Numerical simulations of triggered star formation

by

Scott K. Balfour

A Thesis submitted to Cardiff University
for the degree of Doctor of Philosophy

March 2016

Author: Scott K. Balfour
Title: Numerical simulations of triggered star formation
Date of submission: March 2016

Declaration

This work has not been submitted in substance for any other degree or award at this or any other university or place of learning, nor is being submitted concurrently in candidature for any degree or other award.

Signed: _____ (candidate) **Date:** _____

Statement 1

This thesis is being submitted in the partial fulfillment of the requirements for the degree of PhD.

Signed: _____ (candidate) **Date:** _____

Statement 2

This thesis is the result of my own independant work/investigation, except where otherwise stated. Other sources are acknowledged giving explicit references. The views expressed are my own.

Signed: _____ (candidate) **Date:** _____

Statement 3

I hereby give consent for my thesis, if accepted, to be available for photocopying and for inter-library loan, and for the title and summary to be available to outside organisations.

Signed: _____ (candidate) **Date:** _____

Statement 4: Previously Approved Bar on Access

I hearby give consent for my thesis, if accepted, to be available for photocopying and for inter-library loans **after expiry of a bar on access previously approved by the Academic Standards & Quality Committee**

Signed: _____ (candidate) **Date:** _____

Acknowledgements

I want to begin by thanking my supervisor Anthony Whitworth, who made this entire experience posible and guided me through my Ph.D with patience, humouring me no matter how strange my latest idea sounded. Not only have we worked together to produce some very interesting science but he has also worked hard to help me improve my writing, something for which I will be forever grateful.

I would also like make a special thank you to Oliver Lomax, without whom I would have had no idea how to do anything. Thank you not only for answering all of my questions but for all of the interesting discussions on everything and anything in star formation. There are, of course, all of the other people who have resided in our office and have answered my questions: Katy Holman, Dimitris Stamatellos, Seamus Clarke, Sarah Jaffa and David Hubber. Thank you also.

I must not forget all of my friends who I have spent many hours with talking about science: Ciara Quinn, George Ford, Matt Smith, Chris Clark, Ezzie Pearson, Chris Fuller, Ian Harrison, Laura Nuttall, Andrew Williamson, Thomas Adams, Sebastian Khan, Matt Hunt, Matt Allan, Craig Allford, Tom Bakx, Peri Jones, Olivia Keenan, Camilo Penzloza, Peter Rees, Will Roberts, Subhajit Sarker, Simon Schofield, Rachael Spowage, Rhyan Stock, Gwenllian Williams and anyone else who I may have forgotten. Thank you to all my family who have made this journey possible: Mam, Dad, Sophie and all my grandparents.

Finally, I must thank Jessica Radford for being there through it all, keeping me sane and for trying so hard to understand what I do, so I could bore you with all of my latest breakthroughs and failures. Without you I think I might have fallen at the first hurdle and I would never have made it to this point.

Abstract

Feedback from massive stars is thought to be very important in regulating star formation on a range of scales. However, it is not clear if this feedback acts in a positive way by triggering star formation, or negatively by terminating it. In this thesis we investigate what role feedback plays in determining both the structure of molecular clouds and the rate of star formation, using Smoothed Particle Hydrodynamics. We begin by looking at how the evolution of an HII region is dependent on the amount of ionising radiation the exciting star produces. We then go on to explore the stellar populations created by cloud-cloud collisions and assess their ability to form high mass stars capable of producing large amounts of feedback. We then model the HII regions of these stars and determine what impact these have on star and structure formation.

We find that there is a minimum stellar mass required to produce enough feedback to maintain an HII region. Below this value an HII region will either not form, or form and then implode. Above this value the HII region will act as a traditional HII region, and expand. When two clouds collide we find that they produce a shock compressed layer which forms filamentary structures. The arrangement of these filaments is highly dependent on the collision velocity. Low velocity collisions produce a hub and spoke system in which competitive accretion dominates and produces a few very massive stars and a plethora of low mass stars. High velocity collisions produce filamentary networks that resemble a spider's web. In these spider's webs the stars form at nodes where multiple filaments meet. These nodes act as small local sites for star formation and form either a single, or small collection of stars. As a result stars formed in these systems tend to have a characteristic mass and there is less low mass or high mass star formation. However, we do find that eventually stars capable of producing significant feedback form in all simulations. We model the HII

regions of these stars and find that they very quickly terminate star formation. They also produce very interesting bi-polar HII regions that are difficult to interpret when viewed from some directions.

Contents

Acknowledgements **v**

Abstract **vii**

List of Tables **xiii**

List of Figures **xiv**

1 Introduction **1**

1.0.1 Overview of this thesis 2

2 Background **3**

2.1 Star Formation 3

2.1.1 Molecular Clouds 3

2.1.2 Prestellar cores 4

2.1.3 Solar-type protostars 5

2.1.4 Main Sequence 7

2.2 Colliding clouds/flows 8

2.2.1 Colliding clouds 9

2.3 Feedback 11

2.3.1 Photoionising radiation 12

2.3.2 Photoionisation as a trigger of star formation 14

2.3.3 Stellar Winds 15

3 Numerical Methods **17**

3.1 Smoothed Particle Hydrodynamics 17

3.1.1 Introduction 17

3.1.2 Implementation of SPH 18

3.1.3 Sink Particles . . . 26
3.2 SEREN and GANDALF . . . 28
3.3 Ionizing radiation . . . 29
3.4 Initial Conditions . . . 30
3.4.1 Particle distribution . . . 30
3.4.2 Equation of state . . . 31
3.4.3 Cloud rotations . . . 33

4 What effect does an ionising star have on a cloud already undergoing freefall collapse? 35
4.1 Motivations . . . 35
4.2 Initial cloud conditions . . . 36
4.3 Semi analytic prediction . . . 36
4.3.1 Semi-analytic formulation . . . 36
4.3.2 Semi-analytic solution . . . 43
4.4 Simulations . . . 44
4.4.1 Numerical Setup . . . 45
4.4.2 Evolution of the HII region . . . 45
4.4.3 Evolution of the shell above the ionisation front . . . 46
4.5 Summary . . . 50

5 Cloud-cloud collisions : Effect of the collision velocity 53
5.1 Simulation set-up . . . 54
5.1.1 Initial Conditions . . . 54
5.1.2 Numerical method . . . 55
5.2 Results . . . 56
5.2.1 Fragmentation of the layer . . . 56
5.2.2 Formation of the first protostar . . . 59
5.2.3 Reconfiguration of the filaments . . . 60
5.2.4 The rate of star formation . . . 62
5.2.5 The mass function of protostars . . . 63
5.2.6 Accretion rates . . . 66
5.3 Summary . . . 68

6 Cloud-cloud collisions : Effects of finite closest approach and fractal density **71**

6.1 closest approach . . . 71

6.1.1 Simulation set up . . . 72

6.1.2 Results . . . 72

6.2 Fractal density profile . . . 78

6.2.1 Simulation set up . . . 78

6.2.2 Results . . . 82

6.3 Summary . . . 87

7 A new ionisation method **89**

7.1 Single source treatment . . . 89

7.1.1 Numerical method . . . 90

7.1.2 Temperature smoothing . . . 93

7.1.3 Testing the Spitzer solution . . . 94

7.2 Expanding the method to multiple sources . . . 95

7.3 Computational cost . . . 97

8 Cloud-cloud collisions : Photoionising feedback **99**

8.1 Simulation set up . . . 99

8.2 Results . . . 100

8.2.1 Bipolar HII regions . . . 100

8.2.2 Termination of star formation . . . 105

8.2.3 Final stellar populations . . . 107

8.2.4 Summary . . . 108

9 conclusions **109**

9.1 The effect of an ionising star on a cloud already undergoing freefall collapse . . . 109

9.2 Colliding clouds . . . 110

9.2.1 The collision velocity . . . 110

9.2.2 Variations from the simple model . . . 111

9.3 Colliding clouds and ionising radiation . . . 112

9.3.1 Ionising radiation routine . . . 112

9.3.2 Results . . . 112

9.4 Future Work 113

Bibliography **114**

List of Tables

2.1 This table summarizes the properties of each spectral type. 7

4.1 This table details the three different types of evolutions we identify in our semi-analytic model. 43

5.1 Parameters of the mass functions of protostars formed with different collision velocities. Column 1 gives the collision velocity, v_o, column 2 gives the mean number of protostars, $\bar{\mathcal{N}}_\star$, formed from one collision (and totalling $100\,\mathrm{M}_\odot$), and columns 3 through 6 give, respectively, the mean, $\mu_{\log_{10}}$, standard deviation, $\sigma_{\log_{10}}$, skew, $\gamma_{\log_{10}}$, and kurtosis, $\kappa_{\log_{10}}$, of the protostellar log-masses, $\log_{10}\left(M_\star/\mathrm{M}_\odot\right)$. 66

7.1 This table shows how the routine scales with the number of sources and the number of particles. The simulations were performed with a routine embedded into the GANDALF SPH code. The times given are CPU times, which are the times taken across all 16 processors. To work out the wall time (actual run time) one must divide the numbers in the table by 16, i.e. with $N_{\mathrm{source}} = 1$ and $N_{\mathrm{SPH}} = 10^6$ the routine takes 2.4 s to run. 97

List of Figures

3.1 The evolution of the temperature as a function of density for a gas initally at $T_0 = 10\,K$ using a barotropic equation of state with critical density $\rho_{\rm CRIT} = 10^{-13}\,{\rm g\,cm^{-3}}$. 32

4.1 The predicted radius of the ionisation front as a function of time over a 1.6 Myr period. The Lyman outputs of the stars are $\dot{\mathcal{N}}_{\rm LyC} = 1.4 \times 10^{47}\,{\rm s^{-1}}$, $\dot{\mathcal{N}}_{\rm LyC} = 2.4 \times 10^{47}\,{\rm s^{-1}}$ and $\dot{\mathcal{N}}_{\rm LyC} = 3.4 \times 10^{47}\,{\rm s^{-1}}$ for the blue, red and green lines respectively. In these three lines we see the transition from a contracting evolution to one of expansion, as the ionising output is increased. 44

4.2 The evolution of the shell for the cases where we include infall velocity. The ionising outputs are $\dot{\mathcal{N}}_{\rm LyC} = 1.4 \times 10^{47}\,{\rm s^{-1}}$, $\dot{\mathcal{N}}_{\rm LyC} = 2.4 \times 10^{47}\,{\rm s^{-1}}$ and $\dot{\mathcal{N}}_{\rm LyC} = 3.4 \times 10^{47}\,{\rm s^{-1}}$ for the top , middle and bottom plots respectively. The green line is the radius of the peak density of the shell, the blue lines represent the inner and outer boundaries of the shell, and the red line is the radius of the ionisation front as predicted by the semi-analytic method discussed in Sec. 4.3. The red circles indentify the radii and times at which new stars form. 48

4.3 The evolution of the shell for the cases where we include infall velocity. Each panel shows a the volume density ($log_{10}(\frac{\Sigma}{\delta\xi}{\rm g\,cm^{-2}})$) of a slice ($-0.1\,{\rm pc} < \delta\xi < 0.1\,{\rm pc}$). The ionising out puts are $\dot{\mathcal{N}}_{\rm LyC} = 1.4 \times 10^{47}\,{\rm s^{-1}}$, $\dot{\mathcal{N}}_{\rm LyC} = 2.4 \times 10^{47}\,{\rm s^{-1}}$ and $\dot{\mathcal{N}}_{\rm LyC} = 3.4 \times 10^{47}\,{\rm s^{-1}}$ for the top, middle right and bottom rows respectively. 49

4.4 A slice ($-0.1\,\mathrm{pc} < \delta\xi < 0.1\,\mathrm{pc}$) from a simulation with ionising output $\dot{\mathcal{N}}_{\mathrm{LyC}} = 3.4 \times 10^{47}\,\mathrm{s}^{-1}$. In this plot colour represents volume density ($log_{10}(\frac{\Sigma}{\delta\xi}\mathrm{g\,cm}^{-2})$) .Box A indicates an example of a bright rimed cloud, with box B indicating an example of a pillar. 52

5.1 False-colour image of one of the simulations with $v_{\mathrm{o}} = 2.0\,\mathrm{km\,s}^{-1}$, at time (a) $t_{\star 1} = 1.14\,\mathrm{Myr}$, (b) $t_{10\%} = 1.28\,\mathrm{Myr}$. Colour represents $\log_{10}\{\Sigma/\mathrm{g\,cm}^{-2}\}$, where Σ is column-density projected on the (x, y)-plane. 57

5.2 False-colour column density maps of fragmenting layers at the moment the first protostar forms, $t_{\star 1}$, from simulations using the same initial clouds (one of the ones that start with weak density and velocity perturbations) but different bulk velocities, v_{o}. (a) $v_{\mathrm{o}} = 1.2\,\mathrm{km\,s}^{-1}$, $t_{\star 1} = 1.33\,\mathrm{Myr}$. (b) $v_{\mathrm{o}} = 1.4\,\mathrm{km\,s}^{-1}$, $t_{\star 1} = 1.28\,\mathrm{Myr}$. (c) $v_{\mathrm{o}} = 1.6\,\mathrm{km\,s}^{-1}$, $t_{\star 1} = 1.23\,\mathrm{Myr}$. (d) $v_{\mathrm{o}} = 1.8\,\mathrm{km\,s}^{-1}$, $t_{\star 1} = 1.19\,\mathrm{Myr}$. (e) $v_{\mathrm{o}} = 2.0\,\mathrm{km\,s}^{-1}$, $t_{\star 1} = 1.14\,\mathrm{Myr}$. Colour represents $\log_{10}\{\Sigma/\mathrm{g\,cm}^{-2}\}$, where Σ is column-density projected on the (y, z)-plane, i.e. looking along the direction of the collision. The first protostar is represented by a black dot. . . . 58

5.3 The time of formation of the first protostar, $t_{\star 1}$ (red solid circles, red best-fit line), and the time at which 10% of the total mass has been converted into protostars, $t_{10\%}$ (blue stars, blue best-fit line), plotted against the cloud velocity, v_{o}. The green dashed line is the value of $t_{\star 1}$ predicted by Eqn. (5.5). 60

5.4 False-colour column-density maps of fragmenting layers at the moment, $t_{10\%}$, when 10% of the mass has been converted into protostars, from the same simulations presented in Fig. 5.3. (a) $v_{\mathrm{o}} = 1.2\,\mathrm{km\,s}^{-1}$, $t_{10\%} = 1.47\,\mathrm{Myr}$. (b) $v_{\mathrm{o}} = 1.4\,\mathrm{km\,s}^{-1}$, $t_{10\%} = 1.42\,\mathrm{Myr}$. (c) $v_{\mathrm{o}} = 1.6\,\mathrm{km\,s}^{-1}$, $t_{10\%} = 1.37\,\mathrm{Myr}$. (d) $v_{\mathrm{o}} = 1.8\,\mathrm{km\,s}^{-1}$, $t_{10\%} = 1.33\,\mathrm{Myr}$. (e) $v_{\mathrm{o}} = 2.0\,\mathrm{km\,s}^{-1}$, $t_{10\%} = 1.28\,\mathrm{Myr}$. Colour represents $\log_{10}\{\Sigma/\mathrm{g\,cm}^{-2}\}$, where Σ is column-density projected on the (y, z)-plane, i.e. looking along the direction of the collision. The black dots represent the protostars. 61

5.5 Protostellar mass ranges. For each collision velocity, $v_{\rm o}$, we combine the data from all ten realisations. The green shading gives the full range of protostellar masses, the red shading gives the range between the $10^{\rm th}$ and $90^{\rm th}$ centiles, the blue shading gives the range between the $25^{\rm th}$ and $75^{\rm th}$ centiles (the interquartile range), and the filled circles give the median mass. 64

5.6 The cumulative mass of protostars at $t_{10\%}$, from all 50 simulations (10 at each $v_{\rm o}$),as a function of protostellar mass. Red full curve: $v_{\rm o} = 1.2\,{\rm km\,s^{-1}}$. blue dashed curve: $v_{\rm o} = 1.4\,{\rm km\,s^{-1}}$. green dotted curve: $v_{\rm o} = 1.6\,{\rm km\,s^{-1}}$. black cross-dashed curve: $v_{\rm o} = 1.8\,{\rm km\,s^{-1}}$. purple dot-dashed curve: $v_{\rm o} = 2.0\,{\rm km\,s^{-1}}$. 65

5.7 The final mass of each protostar, $M_\star$, at $t_{10\%}$ (the end of the simulation) plotted against its time of formation, $t_{\rm FORM}$, i.e. the time at which the corresponding sink particle is created. Red dots, $v_{\rm o} = 1.2\,{\rm km\,s^{-1}}$; blue crosses, $v_{\rm o} = 1.4\,{\rm km\,s^{-1}}$; green stars, $v_{\rm o} = 1.6\,{\rm km\,s^{-1}}$; black open circles, $v_{\rm o} = 1.8\,{\rm km\,s^{-1}}$; purple triangles, $v_{\rm o} = 2.0\,{\rm km\,s^{-1}}$. 67

5.8 Log-log plot of the rate of accretion, $\dot{M}_\star$, against the protostellar mass, $M_\star$, both evaluated at the end of the simulation, $t_{10\%}$. Red dots, $v_{\rm o} = 1.2\,{\rm km\,s^{-1}}$; blue crosses, $v_{\rm o} = 1.4\,{\rm km\,s^{-1}}$; green stars, $v_{\rm o} = 1.6\,{\rm km\,s^{-1}}$; black open circles, $v_{\rm o} = 1.8\,{\rm km\,s^{-1}}$; purple triangles, $v_{\rm o} = 2.0\,{\rm km\,s^{-1}}$. Note that the lowest accretion rates are quantised at values $0.1\,{\rm M_\odot\,Myr^{-1}}$, $0.2\,{\rm M_\odot\,Myr^{-1}}$, $0.3\,{\rm M_\odot\,Myr^{-1}}$, etc., corresponding to sinks accreting one, two, three, etc. SPH particles (hence $10^{-3}\,{\rm M_\odot}$, $2 \times 10^{-3}\,{\rm M_\odot}$ $3 \times 10^{-3}\,{\rm M_\odot}$, etc.), during the 0.01 Myr interval between the last two outputs. Similarly some accretion rates fall on the line $\dot{M}_\star = M_\star/0.01\,{\rm Myr}$, corresponding to sinks formed during the 0.01 Myr interval between the last two outputs. 69

6.1 False-colour image of the colliding clouds, as seen looking across the collision axis at $t_{10\%}$ (i.e. when 10 percent of the mass has been converted into protostars). In this case the simulation has $v_{\rm o} = 2.0\,{\rm km\,s^{-1}}$ and b $= {\rm R_0}/4$. Colour represents $log_{10}\{\Sigma/{\rm g\,cm^{-2}}\}$, where Σ is column-density projected on the (x,y)-plane. The black dots are protostars. . 73

6.2 Diagram to illustrate the direction in which the gas will be collapsing in clouds that have b = 0 (A) and b > 0 (B). The diagrams show the view looking across the collision axis and the layer would be located along the collision interface. Red arrows indicate the direction of the vertical collapse in each of the cloud regions. 75

6.3 False-colour images at time $t_{10\%}$, for simulations involving uniform-density clouds colliding at impact parameter $b_{\circ} = 0.25\,\mathrm{pc}$ ($= R_{\circ}/8$) and different collision velocities: (a) $(v_{\circ}, t_{10\%}) = (1.0\,\mathrm{km\,s^{-1}}, 1.53\,\mathrm{Myr})$; (b) $(1.2\,\mathrm{km\,s^{-1}}, 1.49\,\mathrm{Myr})$; (c) $(1.4\,\mathrm{km\,s^{-1}}, 1.42\,\mathrm{Myr})$; (d) $(1.6\,\mathrm{km\,s^{-1}}, 1.36\,\mathrm{Myr})$; (e) $(1.8\,\mathrm{km\,s^{-1}}, 1.30\,\mathrm{Myr})$; (f) $(2.0\,\mathrm{km\,s^{-1}}, 1.25\,\mathrm{Myr})$. Colour represents $\log_{10}\{\Sigma/\mathrm{g\,cm^{-2}}\}$, where Σ is column-density projected on the (y, z)-plane, i.e. looking along the collision axis. The black dots represent stars. 76

6.4 As Fig. 6.3, but with the larger impact parameter, $b_{\circ} = 0.50\,\mathrm{pc}$ ($= R_{\circ}/4$) and (a) $(v_{\circ}, t_{10\%}) = (0.8\,\mathrm{km\,s^{-1}}, 1.62\,\mathrm{Myr})$; (b) $(1.0\,\mathrm{km\,s^{-1}}, 1.55\,\mathrm{Myr})$; (c) $(1.2\,\mathrm{km\,s^{-1}}, 1.48\,\mathrm{Myr})$; (d) $(1.4\,\mathrm{km\,s^{-1}}, 1.41\,\mathrm{Myr})$; (e) $(1.6\,\mathrm{km\,s^{-1}}, 1.34\,\mathrm{Myr})$; (f) $(1.8\,\mathrm{km\,s^{-1}}, 1.28\,\mathrm{Myr})$. 77

6.5 Stellar mass ranges at $t_{10\%}$, for non head-on collisions of uniform-density pre-collision clouds. (a) $b_{\circ} = 0.25\,\mathrm{pc}$ ($= R_{\circ}/8$) and $v_{\circ} = 1.0,\ 1.2,\ 1.4,\ 1.6,\ 1.8$ and $2.0\,\mathrm{km\,s^{-1}}$. (b) $b_{\circ} = 0.50\,\mathrm{pc}$ ($= R_{\circ}/4$) and $v_{\circ} = 0.8\ 1.0\ 1.2,\ 1.4,\ 1.6\ , 1.8$ and $2.0\,\mathrm{km\,s^{-1}}$. For each combination of $b_{\circ}$ and $v_{\circ}$, we combine the results from five different realisations. The green lines give the full range of stellar masses, the red lines give the range between the 10^{th} and 90^{th} centiles, the blue lines give the range between the 25^{th} and 75^{th} centiles (the interquartile range), and the filled circles give the *median* mass. 79

6.6 The cumulative mass distribution of the stars at $t_{10\%}$, for non head-on collisions of uniform-density pre-collision clouds. For each velocity simulated, $v_{\circ} = 0.8\,\mathrm{km\,s^{-1}}$ (yellow curves), $v_{\circ} = 1.0\,\mathrm{km\,s^{-1}}$ (cyan curves), $v_{\circ} = 1.2\,\mathrm{km\,s^{-1}}$ (red curves), $v_{\circ} = 1.4\,\mathrm{km\,s^{-1}}$ (blue curves), $v_{\circ} = 1.6\,\mathrm{km\,s^{-1}}$ (green curves), $v_{\circ} = 1.8\,\mathrm{km\,s^{-1}}$ (black curves), and $v_{\circ} = 2.0\,\mathrm{km\,s^{-1}}$ (purple curves), we combine the results from five different realisations. Panel (a) is for impact parameter $b_{\circ} = 0.25\,\mathrm{pc}$ ($= R_{\circ}/8$). Panel (b) is for $b_{\circ} = 0.50\,\mathrm{pc}$ ($= R_{\circ}/4$). 80

6.7 The cumulative mass,at $t = t_{10\%}$ for (a) simulations with $N_{\rm SPH} = 10^5$ 82

6.8 False-colour image of the colliding clouds, as seen looking across the collision axis at $t_{10\%}$ (i.e. when 10 percent of the mass has been converted into protostars). In this case the simulation has $v_{\rm o} = 1.2\,{\rm km\,s^{-1}}$, b = 0, and a more bumpy fractal density profile, i.e. $\chi = 8$. Colour represents $log_{10}\{\Sigma/{\rm g\,cm^{-2}}\}$, where Σ is column-density projected on the (x,y)-plane. The black dots are protostars. 83

6.9 False-colour images of fragmenting layers at the moment, $t_{10\%}$, when 10% of the mass has been converted into protostars, these simulations have closest approach b = 0 and a relatively smooth fractal density, $\chi = 0$. (a) $v_{\rm o} = 1.2\,{\rm km\,s^{-1}}$, $t_{10\%} = 2.80\,{\rm Myr}$. (b) $v_{\rm o} = 2.0\,{\rm km\,s^{-1}}$, $t_{10\%} = 2.24\,{\rm Myr}$. Colour represents $\log_{10}\{\Sigma/{\rm g\,cm^{-2}}\}$, where Σ is column-density projected on the (y, z)-plane, i.e. looking along the direction of the collision. The black dots represent the protostars. 84

6.10 False-colour images of fragmenting layers at the moment, $t_{10\%}$, when 10% of the mass has been converted into protostars, these simulations have closest approach b = 0 and a more bumpy fractal density, $\chi = 8$. (a) $v_{\rm o} = 1.2\,{\rm km\,s^{-1}}$, $t_{10\%} = 2.93\,{\rm Myr}$. (b) $v_{\rm o} = 2.0\,{\rm km\,s^{-1}}$, $t_{10\%} = 2.39\,{\rm Myr}$. Colour represents $\log_{10}\{\Sigma/{\rm g\,cm^{-2}}\}$, where Σ is column-density projected on the (y, z)-plane, i.e. looking along the direction of the collision. The black dots represent the protostars. 85

6.11 The cumulative mass distribution of the stars at $t_{10\%}$, for clouds with pre-collision density sub-structure colliding head-on. Panel (a) is for mildly clumpy sub-structure ($\chi = 0$). Panel (b) is for strongly clumpy sub-structure ($\chi = 8$). In both panels the blue curve corresponds to collision velocity $v_{\rm o} = 1.2\,{\rm km\,s^{-1}}$, and the green curve to $v_{\rm o} = 2.0\,{\rm km\,s^{-1}}$. In all cases the curves are obtained by combining five different realisations. 86

6.12 Protostellar mass ranges. For each collision velocity, $v_{\circ}$, we combine the data from all five realisations. The green lines give the full range of protostellar masses, the red lines give the range between the 10^{th} and 90^{th} centiles, the blue lines give the range between the 25^{th} and 75^{th} centiles (the interquartile range), and the filled circles give the median mass. The panels show the more bumpy and relatively sooth results for velocities, (a) $v = 1.2\,\mathrm{km\,s^{-1}}$ and (b) $v = 2.0\,\mathrm{km\,s^{-1}}$. 87

7.1 The method used to create an approximate ray from a target particle back to the ionisation source. SPH particles are illustrated by red (particles that do not lie within the target's smoothing length) and green circles (particles that lie within the target's smoothing length); the smoothing length of the target particle is shown as a green circle. In this case we join the target particle to the SPH particle that lies closest to the connecting line between the target particle and the ionisation source. We can then follow the stored ID at this particle to move to the next link in the particle chain. 91

7.2 As in Fig: 7.1, the building of a ray. However in this case we are building it through a non-uniform gas. As shown, the target particle's smoothing length adds a bias in which the next link chosen is not suitable, resulting in a ray that travels through the dense material rather than crossing into the less dense region. 92

7.3 The building of the same ray as the one in Fig: 7.2. In this case we apply a fix in which we also consider particles that have the target particle as a neighbour, such as the particle at the center of the red circle. In this case we are able to make a more appropriate link back to the ionising source 93

7.4 The smoothing length of particles as a function of radius at time $t = 0.01\,\mathrm{Myr}$. Panel A on the left is for the simulation where we do not include temperature smoothing, you can clearly see a break where a discontinuity has formed. In comparison, panel B shows a simulation with the temperature smoothing included, and here we see no break. 94

7.5 The results of a simulation designed to reproduce the Spitzer solution. In this case temperature smoothing has not been turned on. The blue line indicates the location of the ionisation front as predicted by the Spitzer solution (Spitzer, 1978) and the red line indicates the location of the densest part of the shell, which should lie just beyond the ionisation front. 95

7.6 The results of a simulation designed to reproduce the Spitzer solution. In this case temperature smoothing has been turned on. The blue line indicates the location of the ionisation front as predicted by the Spitzer solution (Spitzer, 1978), and the red line indicates the location of the densest part of the shell, which should lie just beyond the ionisation front. 96

7.7 The probability distribution function of the CPU time taken to calculate the ionisation state of the gas for one time step over the entire simulation. 98

8.1 Case A. False-colour images of two clouds with strongly clumpy pre-collision internal sub-structure ($\chi = 8$), undergoing a head-on collision at relatively high velocity ($v_{\circ} = 2.0\,\mathrm{km\,s^{-1}}$); the time is $t = 2.88\,\mathrm{Myr}$. The images on the top line (a and b) are views looking across the collision axis, and those on the bottom line (c and d) are views looking along the collision axis. The lefthand panels (a and c) show the logarithm of the column-density of the neutral gas, i.e. $\log_{10}(\Sigma_{\mathrm{I}}/\mathrm{g\,cm^{-2}})$; the black dots are protostars. The righthand panels (b and d) show the logarithm of the emission-measure, i.e. $\log_{10}(EM/\mathrm{cm^{-5}})$, highlighting the ionised gas. 101

8.2 False-colour image of the colliding clouds, as seen looking across the collision axis at $t = 2.88\,\mathrm{Myr}$, focusing on one of the lobes of the bipolar HII region. The simulation has parameters: $v_{\circ} = 2.0\,\mathrm{km\,s^{-1}}$, b = 0 and has a more bumpy fractal density profile initially, i.e. $\chi = 8$. Colour represents $log_{10}\{\Sigma/\mathrm{g\,cm^{-2}}\}$, where Σ is column-density projected on the (x,y)-plane. 103

8.3 As Fig. 8.1, but for Case B, which involves two clouds with strongly clumpy pre-collision internal sub-structure ($\chi = 8$), undergoing a head-on collision at relatively low velocity ($v_{\circ} = 1.2\,\mathrm{km\,s^{-1}}$); the time is $t = 3.20\,\mathrm{Myr}$. 104
8.4 The total stellar mass as a function of time: $(v_{\circ}, \chi) = (1.2\,\mathrm{km\,s^{-1}}, 0)$, blue; $(1.2\,\mathrm{km\,s^{-1}}, 8;$ Case B), red; $(2.0\,\mathrm{km\,s^{-1}}, 0)$, green; $(2.0\,\mathrm{km\,s^{-1}}, 8;$ Case A), black. 106
8.5 The normalised cumulative mass function: $(v_{\circ}, \chi) = (1.2\,\mathrm{km\,s^{-1}}, 0)$, blue; $(1.2\,\mathrm{km\,s^{-1}}, 8;$ Case B), red; $(2.0\,\mathrm{km\,s^{-1}}, 0)$, green; $(2.0\,\mathrm{km\,s^{-1}}, 8;$ Case A), black. 107

Chapter 1
Introduction

Since the dawn of time humans have looked to the sky and observed the light of stars. It was the study of these tiny specks of light that led to modern day astronomy. However, allowing us to view the universe is not the most important role stars play. They also produce the vital heavy elements required for life, and the light and heat required to sustain it. These facts alone make their formation an important area of study. However, a robust star formation theory is also required so that we can understand a range of other processes, e.g. the evolution of galaxies.

For over a hundred years we have been studying the evolution of Main Sequence and post-Main Sequence stars via observation. However, the study of star formation has only become practical in the last few decades with the introduction of infrared and sub-millimeter telescopes, which can observe young stellar objects.

The evolution of star forming gas is highly non-linear and can only be solved analytically for a small selection of simple gas configurations. This difficulty is further complicated by the spacial range over which the dynamical processes can act. Solutions to these problems have only become possible since the advent of the computer, which allows us to run numerical simulations to model star forming regions. The complexity of these simulations has advanced rapidly with the introduction of large supercomputers which provide unprecedented computing power.

The aim of this thesis is to use numerical simulations to explore the star formation in regions where feedback may be very important. We will focus on the feedback produced by massive stars which emit a large amount of high energy UV radiation.

1.0.1 OVERVIEW OF THIS THESIS

In chapter 2 we provide an overview of star formation process, colliding flows, solar type protostars and the main sequence. In chapter 3 we introduce the Smoothed Particle Hydrodynamics (SPH) codes SEREN and GANDALF, and also give an overview of SPH as a whole. We then describe how ionising radiation is introduced into SEREN. The last part of this chapter introduces other parameters used to create the initial conditions for the simulations. In chapter 4 we place an ionising star within a cloud undergoing free fall collapse and explore how luminous the star has to be to reverse the collapse. In chapter 5 two uniform density molecular clouds are collided head on at a range of velocities. We then explore the stellar populations that form as a result. In chapter 6 we repeat the simulations from chapter 5, but add a finite impact parameter and initial density structure. We determine what impact these have on the stellar populations that form. In chapter 7 we give an overview of the routine we have written to include ionisation in the GANDALF SPH code. In chapter 8 we add photoionising feedback into the simulations from chapter 7 and determine if this triggers or suppresses star formation, and the morphology of the resulting HII regions.

Chapter 2
Background

2.1 Star Formation

2.1.1 Molecular Clouds

Molecular clouds are large condensations of gas found throughout the Galaxy. They are particularly abundant around the spiral arms and have masses in the range $100\,\mathrm{M}_\odot \leq \mathrm{M} \leq 10^6\,\mathrm{M}_\odot$. They also appear to have a range of diameters, $1\,\mathrm{pc} \leq \mathrm{D} \leq 10^2\,\mathrm{pc}$, and mean densities, $10^{-22}\,\mathrm{g\,cm^{-3}} \leq \bar{\rho} \leq 10^{-20}\,\mathrm{g\,cm^{-3}}$.

Molecular clouds are optically thick to UV-dissociative radiation, and consequently they have little atomic hydrogen. For this reason molecular clouds consist mostly of molecular hydrogen, which has no dipole moment and therefore is not detectable at the temperatures characteristic of molecular clouds ($T < 100\,\mathrm{K}$). This makes it almost impossible to determine the column density of hydrogen via direct observation, rather it must be observed indirectly using other methods. One such method is to use molecules such as carbon monoxide (e.g. Wilking and Lada, 1983). However, the interpretation of molecular line observations is complicated by chemistry (molecules do not only exist in the gas phase throughout a cloud), excitation considerations and radiation transport effects. Dense regions are better traced using long-wavelength emission from dust (Motte et al., 1998; Simpson et al., 2008), which is usually optically thin. This is beneficial because the flux density is then proportional to the product of the column density and the temperature. Hence, as long as one can determine the relationship between the dust and gas, and make an accurate estimate of the temperature, one can infer a column density. Fortunately one can make an estimate of the temperature by either fitting a spectral energy distribution (e.g. Kirk et al., 2013) or by using radiative transfer models (e.g. Stamatellos et al., 2007).

All observed molecular clouds have chaotic internal substructure; this suggests that there is some underlying motion in the gas. This gas movement is known as turbulence and could be the result of stellar feedback, or some other cause of uneven structure formation. The supersonic nature of observed velocity dispersions, and the tendency of the velocity size relation to follow a Kolmogorov spectrum (Larson, 1981) are strong indicators that turbulence is present. There is still no clear agreement on what form this turbulence takes, with particular debate as to the correct ratio between the compressive and solenoidal components of the field (Lomax et al., 2015). More recently it has been suggested that magnetic fields may play a very important role in star and structure formation within molecular clouds. However, the extent to which they shape molecular cloud evolution is still unclear. There is some evidence (Palmeirim et al., 2012) that structure formation is related to the direction of the magnetic field, but there is considerable uncertainty with this interpretation. There is also little numerical work to support these conclusions because it is very expensive to simulate magnetic fields, while also solving for gravity and hydrodynamics.

Regions within molecular clouds that have density in excess of $10^{-20}\,\mathrm{g\,cm^{-3}}$ are identified as possible sites of star formation and are known as prestellar cores (Andre et al., 2000). These are cores that appear to be gravitationally bound and are therefore likely to collapse. Once stars have formed, molecular clouds quickly disperse over a few crossing times, leaving behind a cluster of stars (Elmegreen, 2000). This cluster is usually super-virial and disperses to become field stars.

2.1.2 PRESTELLAR CORES

Prestellar cores are dense, gravitationally bound clumps of gas with masses of $10^{-1}\,\mathrm{M_\odot}$ to $10\,\mathrm{M_\odot}$, and diameters in the range $10^{-2}\,\mathrm{pc} \leq \mathrm{D} \leq 10^{-1}\,\mathrm{pc}$. They are quite cool with typical temperatures of 10 K; this is because the core is shielded from the external radiation field by the molecular cloud.

The Jeans criterion is used to determine if a core is likely to collapse, i.e. if the core radius is smaller than the local Jeans length. If it is, then the core is considered to be a prestellar core. The Jeans length is calculated by balancing the gravitational potential energy of a core against twice its thermal energy. One then solves for the core radius, making the assumption that the core is a non-rotating spherical body with mean density $\bar{\rho}$, temperature T and mean gas particle mass $\bar{m}$. This gives the

Jeans length,

$$R_{\rm J} \sim \frac{c_{\rm HI}}{(G\rho_{\rm O})^{1/2}}, \tag{2.1}$$

where $c_{\rm HI}$ is the isothermal sound speed,

$$c_{\rm HI} = \left(\frac{k_{\rm B}T}{\bar{m}}\right)^{1/2}. \tag{2.2}$$

It is sometimes more useful to calculate the minimum mass required for gravitational collapse. This can be the best solution when it is difficult to determine the radius of a core, and in this case the Jeans mass,

$$M_{\rm J} \sim \frac{c_{\rm HI}^3}{G^{3/2}\rho_{\rm O}^{1/2}}, \tag{2.3}$$

is used in place of the Jeans length.

The rate at which the core collapses is not constant; this is due to changes in the radiation transport properties of the gas. Initially the gas is isothermal at a temperature of $\sim 10\,\mathrm{K}$ and the potential energy released by contraction is easily radiated away from the core because the gas is optically thin. As a result the core can collapse rapidly for of order a free fall time, $t_{\rm FF}$,

$$t_{\rm FF} = \sqrt{\frac{3\pi}{32G\bar{\rho}}}. \tag{2.4}$$

However, at a density around $\rho \sim 10^{-13}\,\mathrm{g\,cm^{-3}}$ the gas starts to become optically thick, reducing the rate at which energy can be radiated away. This increases the temperature and thermal pressure, slowing the rate of collapse. At a density of $\sim 10^{-12}\,\mathrm{g\,cm^{-3}}$ the gas becomes completely adiabatic and switches to Kelvin-Helmholtz, i.e. quasistatic, contraction. The rate of collapse accelerates again once the density reaches $\rho \sim 10^{-8}\,\mathrm{g\,cm^{-3}}$ and thermal dissociation of hydrogen begins. During this phase the temperature only increases slowly. Once hydrogen has been dissociated, quasistatic Kelvin-Helmholtz contraction resumes.

2.1.3 Solar-type protostars

Upon forming a protostar a prestellar core moves to the next stage of evolution and becomes classified as a young stellar object (YSO). The energy released as these

objects collapse and accrete makes them luminous sources. However, because they are often deeply embedded within molecular clouds, and have thick envelopes, they are initially very difficult to observe at all but sub-millimeter and infra-red wavelengths. They are split into four classes (Class 0, I, II and III), each of which is thought to represent a different stage of the YSO's evolution (Andre et al., 1993; Lada, 1999).

The earliest stage of stellar evolution begins just after the YSO has formed. At this point it is classified as Class 0 and can be identified by its spectral energy distribution (SED), which is an approximate black body that peaks in the sub-millimeter or far-infrared. As a result it is believed that the YSO is surrounded by an envelope of gas and dust at a temperature of 10 - 20 K. About half of the final stellar mass is accreted onto the YSO during this stage, which lasts of order $10^4 - 10^5$ yrs. There also appears to be a strong relationship between this stage of evolution and the presence of energetic bipolar outflows (Lada, 1999; Andre et al., 2000; Evans et al., 2009).

The SEDs of Class I objects peak in the far-infrared and have a large mid infrared excess. For this reason the SED cannot be modelled as a simple blackbody. In this stage of evolution the system is thought to consist of an envelope which contains a dense object located at the center. It is therefore more appropriate to model the SED as a combination of multiple black bodies rather that just one. Bipolar outflows also appear to be present during this stage of evolution which lasts around $10^5 - 10^6$ yrs (Lada, 1999; Evans et al., 2009).

Class II objects have SED's that peak in the near-infrared or visible wavelengths. This suggests that the central source has emerged from its envelope. The SED also has an infrared excess and emission lines, with the former attibuted to the presence of a circumstellar disk and the latter to accretion onto the star. Class II objects are historically known as T-Tauri stars and remain in this evolutionary stage for approximately 10^6 yrs (Lada, 1999).

Class III objects are in the final stage of evolution prior to moving onto the Main Sequence, and as a result have a SED similar to that of a main sequence star. A blackbody spectrum that peaks in the near infrared or visible wavelengths fits this SED well. It also has emission lines characteristic of atomic hydrogen. These objects are known as Weak-line T-Tauri stars and move onto the main sequence after around 10^7 yrs (Lada, 1999).

2.1.4 Main Sequence

For stars to move from the pre-Main Sequence to the Main Sequence they must collapse to a point where they become sufficiently dense and hot to begin nuclear burning. The energy produced by nuclear burning will then provide sufficient support to prevent further collapse, allowing stars to remain on the Main Sequence for the majority of their luminous lifetimes. Stars that have mass less than $0.08\,M_{\odot}$ will not collapse to a point where they will be able to begin nuclear burning. This is because support from electron degeneracy pressure is introduced before the star becomes hot enough. These stars are known as brown dwarfs and radiate mainly by cooling.

Stars can also be classified based on their spectral type. There are 8 spectral classes[1] O, B, A, F, G, K and M, which are then further split into 10 subclasses. Stars of class O are the hottest stars and those of type M are the coolest, with lower subclasses being hotter, i.e. an O4 star is hotter than an O9. The properties of each spectral type are summarized in table 2.1. Spectral class is also an indicator of the type and intensity of the stellar feedback that the star produces. Stars higher in the classification (i.e. O and B type stars) are hotter and therefore produce a large amount of ionising radiation. These high energy photons will have a significant effect on the entire star forming region. In some cases they will be able to completely destroy the molecular cloud in which they are generated. In contrast, stars lower in the classification are cooler and will therefore only heat local gas, although they will live much longer.

Table 2.1. This table summarizes the properties of each spectral type.

Spectral Type	Surface Temperature / K	Elements present
O	> 30000	H, HeI, HeII
B	$10000 - 30000$	H, HeI
A	$7500 - 10000$	H, CaII
F	$6000 - 7500$	H, metals
G	$5200 - 6000$	H, metals, some molecular species
K	$3700 - 5200$	metals, some molecular species
M	$2400 - 3500$	metals, molecular species

The mass distribution of newly formed stars appears to be roughly universal across most star forming regions in the galaxy (Kroupa, 2001). It is known as the Initial

[1]This increases to 11 if one includes the spectral classes of brown dwarfs: L, T and Y

Mass Function (IMF) and there have been a number of attempts to parameterise it (e.g. Salpeter, 1955; Kroupa, 2001; Chabrier, 2005). Despite this there is no clear consensus as to the origin of the IMF. Some believe it is inherited from the observed mass distribution of cores (Motte et al., 1998; Simpson et al., 2008), others believe it is the result of competitive accretion (Bonnell and Bate, 2006).

2.2 Colliding clouds/flows

Large scale shocks were suggested as precursors of star formation in spiral arms as early as 1969 (Roberts, 1969; Woodward, 1976), but it was not until later that it was suggested that shock-induced star formation occurred regularly on smaller scales. Recent observations (Lefloch and Lazareff, 1995; Sugitani et al., 1999; Walborn et al., 2002) show an unusually high number of star formation regions in and around shocked layers of gas, suggesting that shocks actively trigger star formation.

A number of authors (Elmegreen and Elmegreen, 1978; Ostriker and Cowie, 1981; Vishniac, 1983; Whitworth et al., 1994; McLeod and Whitworth, 2013) have explored the evolution of shock compressed gas layers and find that gravitational instabilities in the layers lead to fragmentation. This fragmentation is thought to happen long before the layer becomes massive enough to be held together by self gravity, and the layer is therefore held together by ram pressure (Whitworth et al., 1994). This results in two possible fragmentation processes that may lead to star formation. The first of these is by Jeans fragmentation, a process in which a spherical ball of gas becomes massive enough to collapse and fragment. In this scenario the thickness of the layer must be greater than the Jeans radius so that it can accommodate a core of sufficient size. Once this thickness is reached the core can then collapse very quickly. It is this method of fragmentation that is invoked most often when discussing such layers. The second form of fragmentation is that due to instabilities parallel to the layer. In this instability gas moves parallel to the layer forming a corrugation, and filaments then form periodically across the layer. However this form of fragmentation takes a long time compared to Jeans fragmentation and has therefore been overlooked.

The fragments produced in a layer formed by converging flows are shown to be much more massive than those formed by molecular cloud collapse alone (Takahira et al., 2014). As a result the layer formed by colliding flows may be very important for high mass star formation. Traditionally high mass stars are difficult to form due to the large amount of material they have to accrete and the relatively short timescale in

which they have to do this (due to their short lifetimes). Massive stars also produce a large amount of radiative and mechanical feedback which suppresses accretion, once again making high mass star formation difficult. However, if the surface density of the star formation region is large enough, the ram pressure associated with the accretion exceeds the radiation pressure and accretion can proceed. Such surface densities are present in shock compressed layers making them possible sites of high mass star formation.

There is no requirement that the flows are molecular, rather they are often treated as atomic, for example in the work of Micic et al. (2013). As a result molecule formation must occur within the collision itself.

2.2.1 Colliding clouds

Colliding clouds are a special case of colliding flows in which two gas clouds come into contact and form a shock compressed gas layer. The layer forms at the collision interface, as gas with opposing velocities comes into contact. The radius of this layer grows as more of the clouds become involved in the collision, and reaches a maximum when the cloud centres become approximately coincident. The mass of the layer increases throughout the collision and is growing fastest when the cloud centres are coincident. When the layer becomes sufficiently massive it fragments. The mass, radius and formation times of these fragments are dependent on the sound speed in the layer, $c_{\rm HI}$, the initial density, ρ_0, and the cloud velocity, v_0 (see Whitworth et al. (1994));

$$M_{\rm fragment} \sim 2c_{\rm HI}^{7/2}\left(G^3\rho_{\rm o}v_{\rm c}\right)^{-1/2}, \tag{2.5}$$

$$r_{\rm fragment} \sim c_{\rm HI}^{3/2}\left(G\rho_{\rm o}v_{\rm c}\right)^{-1/2}. \tag{2.6}$$

$$t_{\rm fragment} \sim \left(\frac{c_{\rm HI}}{G\rho_0 v_0}\right)^{1/2}. \tag{2.7}$$

For a typical molecular cloud with density $\rho_0 \sim 10^{-21}\,{\rm g\,cm^{-3}}$ and temperature $T \sim 10\,{\rm K}$, the fragment mass would be $M_{\rm fragment} \sim 13\,{\rm M}_\odot$, which is the approximate mass of a large B or small O star, although it is worth noting that there is no guarantee this will collapse into one star, rather it may form a small sub-cluster. However, numerical work by Takahira et al. (2014) suggests that clouds with higher

density can form more massive stars, with stars of mass $M = 100\,\mathrm{M}_{\odot}$ being possible.

The finite nature of the clouds in a cloud-cloud collision means one must consider the way in which the two clouds come into contact. The case most related to a colliding flow would be when two uniform density clouds collide head on. However, the general case is a collision at finite closest approach (closest approach is the minimum distance between the cloud centres during the collision. In a head on collision this would be 0), involving clouds which have a density that is larger in the centre than on the outer edges. The density gradients that exist across the layer would cause the layer to take on a more integral like shape than in a head on collision where the layer is straight. This not only alters the shape of the layer but adds angular momentum to the cores that form. This can then halt the collapse of the fragments, resulting in rotationally supported disks. However, this will only happen if there is no redistribution of angular momentum, or further fragmentation. If the closest approach, b, is too large i.e. $b > \sqrt{2}R$ then the collision is unable to produce layers at all (Chapman et al., 1992). This is because only a small amount of the cloud material is shocked, and this is then dispersed radially by shear before fragmentation can begin.

Magnetic fields may also play a role in the fragmentation process. This is discussed in Inoue and Fukui (2013) who find that the effective Jeans mass of the most massive fragment is strongly related to the Alfvenic Jeans mass. This can be orders of magnitude larger than the thermal Jeans mass and as a result including magnetic fields in cloud-cloud collisions tends to produce more massive protostars.

Star formation triggered by cloud cloud collisions may make an important contribution to the IMF. However, this requires that collisions that trigger star formation occur at a high enough frequency. It is very difficult to observe such collisions and so it is not possible to predict the collision frequency based on observation. Early numerical work (Scoville and Hersh, 1979; Norman and Silk, 1980; Tomisaka, 1984; Kwan and Valdes, 1987; Roberts and Stewart, 1987) suggested that the timescale between collisions could be of order 100 Myr, which would mean clouds would not be colliding frequently enough to make a substantial difference to the IMF. Recent work by Dobbs et al. (2015) suggests that collisions could be much more frequent. They carry out simulations that evolve an entire galaxy and are able to follow the motions of the molecular clouds. They are then able to determine how often collisions occur, both inside and outside of the spiral arms. They find that collisions of clouds with mass $M > 10^4 M_{\odot}$, occur once per $8 - 10\,\mathrm{Myr}$ if spiral arms are present, reducing

to once per 28 Myr in they are not. This means that one would expect a cloud to undergo approximately one collision in its lifetime, with some of the most massive clouds undergoing multiple collisions. They also suggest that the velocity dispersions between the clouds will be low, hence collisions may not be as violent as previous work (Hausman, 1981; Lattanzio et al., 1985) has suggested. Duarte-Cabral et al. (2011) find that the clouds in Serpens are colliding with a velocity of $\sim 2\,\mathrm{km\,s^{-1}}$ in agreement with Dobbs et al. (2015) suggestion of low velocity dispersion collisions.

One would have to be very fortunate to directly observe the collision of two molecular clouds as the collision itself does not take long. Rather we are more likely to observe the result of such a collision, particularly in the motions of young star clusters that form. However, this in itself is difficult because although star clusters are often seen in association with the molecular gas that they have formed from, it is difficult to determine if their formation was via spontaneous or triggered gravitational collapse. Despite these difficulties there are a number of possible cloud cloud collision candidates such as Westerlund 2 (Furukawa et al., 2009; Ohama et al., 2010), the Trifid Nebula (Torii et al., 2011), and the Serpens Main Cluster (Duarte-Cabral et al., 2011). There are also cases (Hobbs and Nayakshin, 2009) where a cloud cloud collision can be inferred from the distribution stars and gas.Work by Haworth et al. (2015a,b) also suggests a possible method of identifying collisions which could be beneficial in the future.

2.3 Feedback

Stellar feedback is observed on a wide range of scales and appears to play a significant role in regulating star formation. At small scales it may regulate star formation and drive small scale turbulence. At large scales it plays a role in both the formation and evolution of galaxies. The intensity and type of feedback is dependent on both the type and evolutionary stage of the star. Massive stars at the end of their lives are very important for regulating star formation on galactic scales due to the large amount of energy they inject into the interstellar medium when they undergo a supernova explosion (Agertz et al., 2013). The galactic star formation rate may also be affected by feedback produced during the lifetime of these stars. This is delivered in the form of stellar winds and photoionisation. Smaller stars are unable to produce enough feedback to directly affect the galactic star formation rate, but they do help to set stellar masses and drive small scale turbulence via radiation pressure, stellar outflows and jets. It is still not clear if feedback increases or decreases the amount,

or rate of star formation. In this thesis we are most concerned with the feedback of massive stars during their lifetimes and will therefore not discuss in detail the feedback from small stars or supernovae.

2.3.1 PHOTOIONISING RADIATION

Infrared shells and bubbles appear throughout the Galaxy (e.g. Churchwell 2006, Churchwell 2008) and always contain at least one massive star, which usually lies at the center. Young massive stars are very hot and produce a large amount of Lyman continuum radiation ($E_\gamma > 13.6\,\mathrm{eV}$). This radiation ionises and heats the local gas to temperatures of $T \sim 10^4$ K, creating the bubbles we observe. HII regions can be identified by the bright Photon Dominated (or Photo Dissociation) regions (PDR's) that lie at the boundary of the ionised gas. These regions are interesting areas of study because there appears to be a large number of star formation regions in and around the bubbles, suggesting that their expansion may be the direct cause of star formation. However, these star formation regions may have formed regardless and are just being triggered early or are being reveled. Further to this, it may be the case that, although in the short term HII regions trigger star formation they may have an overall negative effect on star formation by dispersing the remaining gas cloud.

HII regions can be a range of shapes, and there are even some examples of bipolar HII regions (Deharveng et al., 2015). We now discuss the typical structure of an HII region that results from a massive star or star cluster. Immediately surrounding the central star there will be a large bubble of ionised gas created by the large amounts of high energy UV radiation emitted from the star. This bubble of gas is very hot and is therefore initially overpressured. As a result it expands rapidly into the gas that surrounds it. The outer boundary of this ionised gas is known as the ionisation front. The transition between the ionised and neutral gas is very sharp at this location and this allows us to treat it as a front. Just above this front lies a shell of dense neutral gas, this is the PDR in which the gas changes from being mostly atomic to mostly molecular. As the HII region expands it ploughs through the neutral gas which it accretes, and ultimately the shell of swept-up gas becomes sufficiently massive to fragment. At this point it breaks up into a number of structures we see in observations, such as bright-rimmed clouds and pillars, and it is in these structures we see most star forming regions. More massive stars produce more ionising photons and therefore have more massive HII regions. Not all stars are able to create and maintain HII regions. Only when a star exceeds a given mass will it produce an HII region.

The ionisation of the initial bubble occurs very quickly because all of the photons produced by the star are used up on a timescale much shorter than the sound crossing time of the bubble. As a result the gas does not move significantly prior to the system reaching ionisation balance and so the initial radius of the HII can be calculated easily. This is done by equating the rate at which the source emits ionising photons to the rate at which protons and electrons recombine thought the total volume of the HII region,

$$\mathcal{N}_{\rm Lyc} = \frac{4}{3}\pi R_{\rm s}^3 \alpha_2 n_{\rm e}^2. \tag{2.8}$$

Here α_2 is the recombination coefficient into excited states only, $R_{\rm s}$ is the radius of the HII region and $n_{\rm e}$ is the electron number density. Only recombinations into excited states are taken into account and it is assumed that the proton number density is the same as the electron number density. This is justifiable because hydrogen is considerably more abundant than any other element. Were we to include helium in this calculation we could see an increase of up to 20% in the number of free electrons. However, there are few photons with an energy high enough to ionise helium twice, and as a result a 10% increase is more realistic. By re-arranging Eqn. 2.8 one can obtain an expression for the initial radius of the HII region,

$$R_{\rm s} = \left(\frac{3\mathcal{N}_{\rm Lyc}}{4\pi\alpha_2 n_{\rm e}^2}\right)^{1/3}. \tag{2.9}$$

This is known as the Stømgren radius and was first proposed by Strømgren (1939). Using α_2 makes the assumption that the star does not have to re-ionise atoms that recombine directly into the ground state. Fortunately hydrogen presents a large cross section to the photons produced by the recombinations and a compensatory ioinisation is likely to occur. One can then assume that the photons produced by recombinations are not able to travel far before they re-ionise another atom. Hence photons from the star only need to balance recombinations into excited states. This is known as 'the on the spot approximation'.

Initially the number of UV photons per unit area, per second is so large that the ionisation front advances straight into the neutral gas, becoming a weak detonation front. This type of expansion is known as R-type expansion (see Kahn, 1954) and produces only an ionised gas bubble, i.e there is no shock front advancing into the neutral gas, and as a result there is no shell. In general this type of expansion is

not modeled in numerical simulation, rather gas is ionised to the Støgmgren radius at which point D-type (see Kahn, 1954) expansion begins. D-type expansion is a dynamical expansion due to the increased pressure of the ionised gas in comparison to the neutral gas that surrounds it. A shock front is able to advance ahead of the ionisation front, directly into the neutral gas which it sweeps up into a dense gas layer. As expansion continues the number of photons per unit area falls and the rate of expansion decreases, possibly leading to a halt in the expansion. However, in most cases the star will explode as a supernova long before this happens. The rate of this expansion was calculated analytically by Spitzer (1978) who showed that in a uniform non-gravitating gas the radius of the HII region is given by,

$$R_{\rm IF}(t) \, = \, R_{\rm St} \left(1 + \frac{7}{4} \frac{c_{\rm HII} t}{R_{\rm St}} \right)^{4/7} , \tag{2.10}$$

where $c_{\rm HII}$ is the sound speed in the ionised gas.

As the shock front is driven into the neutral gas it sweeps up a dense shell. The surface density of this shell grows as more material is accreted onto it, and eventually it may become gravitationally unstable. This can lead to the shell breaking up into a number of fragments, which can collapse to form a new generation of protostars. This process is referred to as triggered star formation and can in some cases lead to the formation of further massive stars. These may then excite their own HII regions in a process known as propagating star formation. Some of the fragments that form may fall into, or be surrounded by, the HII region itself. These structures are known as cometary globules. Bisbas et al. (2011) show that stars may form in these structure as a result of radiation driven implosion. They also show that this process produces structures such as bright-rimmed clouds and elephant trunks (see Figs. 7 and 8 of Bisbas et al., 2011).

2.3.2 PHOTOIONISATION AS A TRIGGER OF STAR FORMATION

There is a large amount of observational and numerical evidence to suggest that feedback has a direct effect on star formation. In some cases (Elmegreen, 2002; Whitworth and Francis, 2002; Elmegreen, 2011) it has been shown that feedback has a positive effect by triggering star formation. However, in other cases (Whitworth, 1979; Tenorio-Tagle, 1979; Bodenheimer et al., 1979; Franco et al., 1990; Matzner, 2002) it has been shown to eject large amount of gas from the cloud, ultimately dispersing it and reducing the star formation rate. Unfortunately it is difficult to

distinguish triggered star formation from spontaneous star formation and this has hindered attempts to determine if feedback is positive or negative. There has been some effort (Preibisch and Zinnecker, 2007) to identify whether star formation has been triggered, using age gradients, but results have yet to yield conclusive evidence.

The negative effects of feedback have been shown to destroy a normal giant molecular cloud in less than a crossing time (Whitworth, 1979; Matzner, 2002). However, this is not the case for more massive clouds, where photoionisation plays less of a role (Krumholz and Matzner, 2009; Murray et al., 2010; Fall et al., 2010). This is because the accretion flows present in massive clouds are able to quench ionising feedback and hence prevent the expulsion of gas from the system (Dale et al., 2012).

Walch et al. (2012) suggest that ionising feedback can be very effective at triggering star formation. However, they find the feedback has the effect of accelerating star formation rather than increasing the total amount of star formation. In fact the cloud is quickly blown apart following the introduction of feedback and is therefore only able to convert a small fraction of its gas into stars.

2.3.3 Stellar Winds

Stellar winds are fast-moving flows of material ejected from stars, and they are able to inject a large amount of kinetic energy into the gas around the star. Much like HII regions they are able to carve out large cavities in the neutral gas surrounding the stars, and could therefore have a large impact on local star formation. However, McKee et al. (1984) argue that wind bubbles are likely to be trapped within the HII regions created by their driving stars, or that the inhomogeneous density fields in the gas are likely to cool the winds on their expansion timescales, decreasing their effectiveness. Further to this Dale et al. (2014) suggest that in all but the most dense gas, photoionisation will dominate. In the absence of ionising radiation, winds have been shown to carve escape routes out of the cold gas, something also seen in simulations of ionising radiation i.e Rogers and Pittard (2013); these escape routes vent hot gas out of the cloud and reduce the destructive effect of both the ionising radiation and stellar winds. The most noticable effects of stellar winds are related to the structure of the ionised gas within the HII region. Winds from large stars tend to gather the ionised gas in a thin layer that lines the inner edge of the shell (Freyer et al., 2003, 2006). Stars with moderate mass are unable to produce a stellar wind capable of sweeping up all of the ionised material and in this case a small hole

develops in the center of the HII region.

Chapter 3
Numerical Methods

3.1 Smoothed Particle Hydrodynamics

In this chapter I give an overview of Smoothed Particle Hydrodynamics (SPH). SPH is a numerical method used to model the hydrodynamics and self-gravity of star forming gas. In this thesis we use two codes to carry out simulations, SEREN (Hubber et al., 2011) and GANDALF (Hubber et. al. in prep), both of which are SPH based. I will also give a brief overview of sink particles. These are used in both SEREN and GANDALF to represent dense regions which are destined to collapse to stellar density and would otherwise be too costly to simulate.

3.1.1 Introduction

The evolution of star forming gas is non-linear in nature which makes it difficult to simulate. There are few known analytical solutions, and in general the problem must therefore be solved numerically. This is done by first solving the equations of hydrodynamics at all points within the simulation domain. The three equations that must be solved are the continuity, momentum and energy equations;

$$\frac{d\rho}{dt} \equiv \frac{\partial \rho}{\partial t} + \mathbf{v} \cdot \nabla \rho = -\rho \nabla \cdot \mathbf{v}, \tag{3.1}$$

$$\rho \frac{d\mathbf{v}}{dt} \equiv \frac{\partial \rho \mathbf{v}}{\partial t} + \rho \mathbf{v} \nabla \mathbf{v} = -\nabla \cdot P, \tag{3.2}$$

$$\frac{du}{dt} \equiv \frac{\partial u}{\partial t} + \mathbf{v} \cdot \nabla u = -\frac{P}{\rho} \nabla \cdot \mathbf{v}. \tag{3.3}$$

In these equations $\mathbf{v}$ is the gas velocity, ρ is the density, u is the specific internal energy and P is the pressure, given by,

$$P = \frac{\rho k_{\rm B} T}{\bar{m}}. \tag{3.4}$$

Here $\bar{m} = 4.8 \times 10^{-23}$ g is the mean molecular mass for cold interstellar gas. One can use either grid based or particle based codes to solve these equations. Grid based approaches use an Eulerian grid to model the fluid. In this type of simulation the grid, and hence the reference frame, is considered static and the fluid moves through it. This is done by dividing the computational domain into a fixed position grid. Each grid cell is then checked, and the Eulerian derivatives are calculated. In standard grid codes each grid cells has a fixed size. This makes it difficult to simulate a large range of length scales. Adaptive Mesh Refinement (AMR) is used to overcome this problem. In this scheme the grid cells can have different lengths, this allows grid squares to split into smaller grid squares when higher resolution is required. Particle methods divide the fluid into a finite number of particles, each with their own position and velocity. By doing this one assumes the reference frame moves with the fluid, allowing the Lagrangian derivatives to be calculated at each SPH particle. Grid based methods are less noisy and are more reliable when dealing with shocks, but they are not as good at dealing with rotating or rapidly contracting bodies. In contrast, particle methods are able to deal with rotating bodies and are also better able to deal with a large range of length scales.

3.1.2 IMPLEMENTATION OF SPH

SPH was pioneered by Lucy (1977); Gingold and Monaghan (1977) and uses a particle based approach to model a continuous fluid as an ensemble of discrete points, referred to as particles. Each particle has a unique position $\mathbf{r}$, velocity $\mathbf{v}$ and mass $m_{\rm SPH}$, although particles of different mass are rarely used within one simulation. Eqns. 3.2 and 3.3 are integrated at each particle position in order to evolve the gas. In general Eqn. 3.1 does not need to be integrated because each particle has a constant mass.

A kernel is used to smooth each particle such that it overlaps with $\mathcal{N}$ neighboring particles. This allows the discrete particles to be modeled as a continuous fluid. Any continuous quantity, A, can then be convolved with the smoothing kernel to give,

$$\langle A(\mathbf{r}) \rangle = \int_V A(\mathbf{r}') W(\mathbf{r} - \mathbf{r}', h) d\mathbf{r}'^{\mathbf{3}}, \tag{3.5}$$

at any point $\mathbf{r}$ in space. Here $W(\mathbf{r}-\mathbf{r}^{'},h)$ is the kernel, centred at r with length-scale h. The only requirement of the kernel is that it must tend to a Dirac delta function as h tends to zero, and must be normalised so that,

$$\int_V W(\mathbf{r}-\mathbf{r}^{'},h)d\mathbf{r}^{'3} \;=\; 1. \tag{3.6}$$

The integral in Eqn 3.5 is replaced with a summation over the particles contained within the extent of the kernel, i.e.

$$\langle A(\mathbf{r}_{\mathrm{i}})\rangle \;=\; \sum_{j=1}^{\mathcal{N}} \frac{m_{\mathrm{j}}}{\rho_{\mathrm{j}}} A_{\mathrm{j}} W(\mathbf{r}_{\mathrm{ij}},h), \tag{3.7}$$

allowing one to perform the SPH calculations. Most kernels have a well known analytical solution to $\nabla W(\mathbf{r}_{i,j},h)$, and it is therefore useful to calculate the gradient of A, using

$$\langle \nabla A(\mathbf{r}_{\mathrm{i}})\rangle \;=\; \sum_{j=1}^{\mathcal{N}} \frac{m_{\mathrm{j}}}{\rho_{\mathrm{j}}} A_{\mathrm{j}} \nabla W(\mathbf{r}_{\mathrm{ij}},h). \tag{3.8}$$

In both of these equations $\mathbf{r}_{\mathrm{ij}} \;=\; \mathbf{r}_{\mathrm{i}} \;-\; \mathbf{r}_{\mathrm{j}}$, and the volume element $d\mathbf{r}^{'3}$ has been replaced by $\frac{m_{\mathrm{j}}}{\rho_{\mathrm{j}}}$.

Kernel

Originally a Gaussian was used for the smoothing kernel (Lucy, 1977) and although this was reasonable at the time it was later realised that it can be physically unrealistic and very expensive. This is because physical quantities such as the pressure and density only act locally and should not be smoothed over the entire fluid. To correct for this, a range of new compact kernels was devised, with the most popular being the M4 kernel (Monaghan and Lattanzio, 1985). This kernel has compact support and is spherically symmetric; it is given by,

$$W_{\mathrm{M4}}(s) \;=\; \frac{1}{\pi h^3} \begin{cases} 1 \;-\; \frac{3}{2}s^2 \;+\; \frac{3}{4}s^3 & \text{if } 0 \;\leq\; \mathrm{s} \;\leq\; 1; \\ \frac{1}{4}(2 \;-\; s)^3 & \text{if } 1 \;\leq\; \mathrm{s} \;\leq\; 2; \\ 0 & \text{if s} \;>\; 2. \end{cases} \tag{3.9}$$

in three dimensions, where $s = |\mathbf{r}_{ij}|/h$. Eqn. 3.8 requires that we find the first spacial derivative of the smoothing kernel,

$$\nabla W_{M4} = \hat{\mathbf{r}}_{ij} \frac{dW_{M4}}{dr} \tag{3.10}$$

where,

$$\frac{dW_{M4}}{dr}(s) = \frac{1}{\pi h^4} \begin{cases} 3s - \frac{9}{4}s^2 & \text{if } 0 \leq s \leq 1; \\ \frac{3}{4}(2-s)^2 & \text{if } 1 \leq s \leq 2; \\ 0 & \text{if } s > 2. \end{cases} \tag{3.11}$$

Smoothing length

The length scale of the smoothing kernel is commonly referred to as the smoothing length, and was originally a global value based on the average inter-particle spacing. However, if we are to simulate gas at a range of length scales we must allow the smoothing length to vary based on the local gas density. Therefore Monaghan (2002) suggested that the smoothing length should be,

$$h_i = \eta \left(\frac{m_i}{\rho_i} \right)^{\frac{1}{3}}, \tag{3.12}$$

where η is a free parameter which determines the number of nearest neighbours. We use $\eta = 1.2$ which gives, on average, 56 neighbours (Price and Monaghan, 2004). Here ρ_i is a continuous SPH quantity given by,

$$\rho_i = \sum_{j=1}^{\mathcal{N}} m_j W(\mathbf{r}_{ij}, h_{ij}). \tag{3.13}$$

Hence ρ_i and h_i are interdependent and must be iterated to achieve a solution; we iterate until $|h_i - h|/h < 10^{-2}$. This results in each particle having approximately $\bar{\mathcal{N}} \sim \frac{4}{3}\pi(2\eta)^3 \sim 56$ neighbours.

SPH equations

When calculating SPH quantities we must ensure that all the forces between particle pairs are equal and opposite, hence,

$$\frac{\nabla A}{\rho} = \nabla \left(\frac{A}{\rho} \right) + \frac{A}{\rho^2} \nabla \rho, \tag{3.14}$$

is substituted into Eqn. 3.2 to give,

$$\frac{dv_{\rm i}}{dt}|_{\rm HYDRO} = -\sum_{j=1}^{\mathcal{N}} m_{\rm j} \left(\frac{P_{\rm i}}{\rho_{\rm i}^2} + \frac{P_{\rm j}}{\rho_{\rm j}^2} \right) \nabla_{\rm i} W(\mathbf{r}_{\rm ij}, h_{\rm i}). \tag{3.15}$$

By substituting Eqn. 3.1 into Eqn. 3.3 we calculate the time derivative of the specific internal energy,

$$\frac{du_{\rm i}}{dt} = \frac{P_{\rm i}}{\rho_{\rm i}^2} \frac{d\rho_{\rm i}}{dt}, \tag{3.16}$$

or as a SPH quantity,

$$\frac{du_{\rm i}}{dt}|_{\rm HYDRO} = \frac{P_{\rm i}}{\rho_{\rm i}^2} \sum_{j=1}^{\mathcal{N}} m_{\rm j} \mathbf{v}_{\rm ij} \cdot \nabla_{\rm i} W(\mathbf{r_{ij}}, h_{\rm i}). \tag{3.17}$$

In this equation $\mathbf{v}_{\rm ij} = \mathbf{v}_{\rm i} - \mathbf{v}_{\rm j}$.

Correction terms

Nelson and Papaloizou (1994) found that using variable smoothing lengths could lead to energy not being conserved. To correct for this Monaghan (2002) made modifications to Eqns. 3.15 and 3.17,

$$\frac{d\mathbf{v_i}}{dt}|_{\rm HYDRO} = -\sum_{j=1}^{\mathcal{N}} m_{\rm j} \left(\frac{P_{\rm i}}{\rho_{\rm i}^2 \Omega_{\rm i}} \nabla_{\rm i} W(\mathbf{r}_{\rm ij}, h_{\rm i}) + \frac{P_{\rm j}}{\rho_{\rm j}^2 \Omega_{\rm j}} \nabla_{\rm i} W(\mathbf{r}_{\rm ij}, h_{\rm j}) \right), \tag{3.18}$$

$$\frac{du_{\rm i}}{dt}|_{\rm HYDRO} = \frac{P_{\rm i}}{\rho_{\rm i}^2 \Omega_{\rm i}} \sum_{j=1}^{\mathcal{N}} m_{\rm j} \mathbf{v}_{\rm ij} \cdot \nabla_{\rm i} W(\mathbf{r}_{\rm ij}, h_{\rm i}). \tag{3.19}$$

Here,

$$\Omega_{\rm i} = 1 - \frac{\partial h_{\rm i}}{\partial \rho_{\rm i}} \sum_{j=1}^{\mathcal{N}} m_{\rm j} \frac{\partial W}{\partial h}(\mathbf{r}_{\rm ij}, h_{\rm i}) \tag{3.20}$$

and

$$\frac{\partial W_{\rm M4}}{\partial h} = \frac{1}{\pi h^4} \begin{cases} -3 + \frac{15}{2}s^2 - \frac{9}{2}s^3 & \text{if } 0 \leq \text{s} \leq 1; \\ -6 + 12s - \frac{15}{2}s^2 + \frac{3}{2}s^3 & \text{if } 1 \leq \text{s} \leq 2; \\ 0 & \text{if s} > 2. \end{cases} \tag{3.21}$$

Artificial viscosity

Shocks are problematic in SPH and can cause unphysical effects. Particles are prone to oscillate behind shock fronts, or pass through shocks rather than decelerating. Artificial viscosity is used to reduce the impact of these problems. Monaghan (1997) introduce a viscosity term into the equation of motion,

$$\frac{d\mathbf{v}_{\mathrm{i}}}{dt}|_{\mathrm{VISC}} = -\sum_{j=1}^{\mathcal{N}} m_{\mathrm{j}} \Pi_{\mathrm{ij}} \nabla_{\mathrm{i}} \bar{W}(\mathbf{r}_{\mathrm{ij}}, h_{\mathrm{i}}, h_{\mathrm{j}}), \tag{3.22}$$

where

$$\bar{W}(\mathbf{r}_{\mathrm{ij}}, h_{\mathrm{i}}, h_{\mathrm{j}}) = \frac{\nabla_{\mathrm{i}} W(\mathbf{r}_{\mathrm{ij}}, \mathbf{h}_{\mathrm{i}}) + \nabla_{\mathrm{i}} W(\mathbf{r}_{\mathrm{ij}}, \mathbf{h}_{\mathrm{j}})}{2}, \tag{3.23}$$

and

$$\Pi_{\mathrm{ij}} = \begin{cases} \frac{-\alpha v_{\mathrm{SIG}} \mathbf{v}_{\mathrm{ij}} \cdot \mathbf{r}_{\mathrm{ij}}}{\bar{\rho}_{\mathrm{ij}} |\mathbf{r}_{\mathrm{ij}}|} & \text{if } \mathbf{v}_{\mathrm{ij}} \cdot \mathbf{r}_{\mathrm{ij}} \leq 0; \\ 0 & \text{if } \mathbf{v}_{\mathrm{ij}} \cdot \mathbf{r}_{\mathrm{ij}} > 0. \end{cases} \tag{3.24}$$

Here $\bar{\rho}_{\mathrm{ij}} = (\rho_{\mathrm{i}} + \rho_{\mathrm{j}})/2$, and v_{SIG} is the signal velocity as given by,

$$v_{\mathrm{SIG}} = c_{\mathrm{i}} + c_{\mathrm{j}} - \beta \frac{\mathbf{v}_{\mathrm{ij}} \cdot \mathbf{r}_{\mathrm{ij}}}{|\mathbf{r}_{\mathrm{ij}}|}. \tag{3.25}$$

The gas is then heated due to the dissipation of kinetic energy,

$$\frac{du_{\mathrm{i}}}{dt}|_{VISC} = \sum_{j=1}^{\mathcal{N}} m_{\mathrm{j}} \Lambda_{\mathrm{ij}} \mathbf{r}_{\mathrm{ij}} \cdot \bar{W}(\mathbf{r}_{\mathrm{ij}}, h_{\mathrm{i}}, h_{\mathrm{j}}), \tag{3.26}$$

where,

$$\Lambda_{\mathrm{ij}} = \begin{cases} \frac{\alpha v_{\mathrm{SIG}} (\mathbf{v}_{\mathrm{ij}} \cdot \mathbf{r}_{\mathrm{ij}})^2}{2\bar{\rho}_{\mathrm{ij}} |\mathbf{r}_{\mathrm{ij}}|^2} & \text{if } \mathbf{v}_{\mathrm{ij}} \cdot \mathbf{r}_{\mathrm{ij}} \leq 0; \\ 0 & \text{if } \mathbf{v}_{\mathrm{ij}} \cdot \mathbf{r}_{\mathrm{ij}} \geq 0. \end{cases} \tag{3.27}$$

The terms $\alpha = 1$ and $\beta = 2$ determine the level of viscosity in regions of low and high Mach number shocks respectively. The values I use are those recommended by Morris and Monaghan (1997).

Time-dependent viscosity

Through the addition of artificial viscosity terms Morris and Monaghan (1997) were able to correct most of the problems that SPH has in dealing with shocks. However, artificial viscosity can also unintentionally be added to shearing flows, which can lead to unphysical transport of angular momentum. This can be prevented by assigning a value of $\alpha_{\rm i}$ to each particle, which decays in regions where artificial viscosity is not needed, thereby alleviating the problem. Artificial viscosity evolves as,

$$\frac{d\alpha_{\rm i}}{dt} = \frac{\alpha_{\rm MIN} - \alpha_{\rm i}}{\tau_{\rm i}} + S_{\rm i}, \tag{3.28}$$

where $\alpha_{\rm MIN}$ is the minimum value α can take. $\tau_{\rm i}$ is the time scale on which it decays and is given by,

$$\tau_{\rm i} = \frac{h_{\rm i}}{c_{HI} C}. \tag{3.29}$$

Here $c_{\rm HI}$ is the local sound speed and $C = 0.1$. Rosswog et al. (2000) gives us the source term $S_{\rm i}$,

$$S_{\rm i} = \begin{cases} -(\alpha_{\rm MAX} - \alpha_{\rm MIN})\,\nabla \cdot \mathbf{v}_{\rm i} & \text{if } \nabla \cdot \mathbf{v}_{\rm i} \leq 0; \\ 0 & \text{if } \nabla \cdot \mathbf{v}_{\rm i} > 0. \end{cases} \tag{3.30}$$

For any particle in a shocked region $\alpha_{\rm i}$ increases to a maximum value $\alpha_{\rm MAX}$, which will then decay to $\alpha_{\rm MIN} = 0.1$ once it leaves this region. Hence we replace α in Eqns. 3.24 and 3.27 with $\alpha_{\rm ij} = (\alpha_{\rm i} + \alpha_{\rm j})/2$.

Gravity

Like all other continuous SPH quantities gravity must be kernel smoothed. Price and Monaghan (2007) derive the smoothed gravitational potential to be,

$$\phi(\mathbf{r}, h) = 4\pi \left(-\frac{1}{r} \int_0^r W(\mathbf{r}', h) r'^2 dr' + \int_0^r W(\mathbf{r}', h) r' dr' - \int_0^{2h} W(\mathbf{r}', h) r' dr' \right), \tag{3.31}$$

hence the smoothed force is,

$$\phi'(\mathbf{r}, h) = \frac{4\pi}{r^2} \int_0^r W(\mathbf{r}', h) r'^2 dr'. \tag{3.32}$$

Using this we can then determine the gravitational acceleration of each particle,

$$\frac{d\mathbf{v}_{\rm i}}{dt}|_{\rm GRAV} = -G\sum_{j=1}^{\mathcal{N}} m_{\rm j}\bar{\phi}'(\mathbf{r}_{\rm ij}, h_{\rm i}, h_{\rm j})\hat{\mathbf{r}_{\rm ij}} - \frac{G}{2}\sum_{j=1}^{\mathcal{N}}\left(\frac{\xi_{\rm i}}{\Omega_{\rm i}}\nabla_{\rm i}W(\mathbf{r}_{\rm ij}, h_{\rm i}) + \frac{\xi_{\rm j}}{\Omega_{\rm j}}\nabla_{\rm i}W(\mathbf{r}_{\rm ij}, h_{\rm j})\right), \tag{3.33}$$

where,

$$\bar{\phi}'(\mathbf{r}_{\rm ij}, h_{\rm i}, h_{\rm j}) = \frac{\phi'(\mathbf{r}_{\rm ij}, h_{\rm i}) + \phi'(\mathbf{r}_{\rm ij}, h_{\rm j})}{2}, \tag{3.34}$$

and,

$$\xi_{\rm i} = \frac{\partial h_{\rm i}}{\partial \rho_{\rm i}}\sum_{j=1}^{\mathcal{N}} m_{\rm j}\frac{\partial \phi}{\partial h}(\mathbf{r}_{\rm ij}, h_{\rm i}). \tag{3.35}$$

The first term on the right of Eqn. 3.33 is the standard prescription for kernel softened gravity, and the second term is a correction to the force at small distances to help conserve energy. The value of ϕ' is dependent on the kernel, and in this case we use the relevant value for the M4 kernel,

$$\phi'_{\rm M4}(s) = \frac{1}{h^2}\begin{cases} \frac{4}{3}s^3 - \frac{6}{5}s^5 + \frac{1}{2}s^6 & \text{if } 0 \le \text{s} \le 1; \\ \frac{8}{3}s - 3s^2 + \frac{6}{5}s^3 - \frac{1}{6}s^4 - \frac{1}{15}s^{-2} & \text{if } 1 \le \text{s} \le 2; \\ 1 & \text{if s} > 2, \end{cases} \tag{3.36}$$

and,

$$\frac{\partial \phi_{\rm M4}}{\partial h}(s) = \frac{1}{h^2}\begin{cases} \frac{7}{5} - 2s^2 + \frac{3}{2}s^4 - \frac{3}{5}s^5 & \text{if } 0 \le \text{s} \le 1; \\ \frac{8}{5} - 4s^2 + 4s^3 - \frac{3}{2}s^4 + \frac{1}{5}s^5 & \text{if } 1 \le \text{s} \le 2; \\ 0 & \text{if s} > 2. \end{cases} \tag{3.37}$$

We are also able to calculate the gravitational potential at the position of any particle i,

$$\Phi_{\rm i} = G\sum_{j=1}^{\mathcal{N}} m_{\rm j}\bar{\phi}(\mathbf{r}_{\rm ij}, h_{\rm i}, h_{\rm j}), \tag{3.38}$$

where,

$$\bar{\phi}(\mathbf{r}_{\rm ij}, h_{\rm i}, h_{\rm j}) = \frac{\phi(\mathbf{r}_{\rm ij}, h_{\rm i}) + \phi(\mathbf{r}_{\rm ij}, h_{\rm j})}{2}, \tag{3.39}$$

and,

$$\phi_{\rm M4}(s) = \frac{1}{h}\begin{cases} \frac{7}{2} - \frac{2}{3}s^2 + \frac{3}{10}s^4 - \frac{1}{10}s^5 & \text{if } 0 \leq \text{s} \leq 1; \\ \frac{8}{5} - \frac{4}{3}s^2 + s^3 - \frac{3}{10}s^4 + \frac{1}{30}s^5 - \frac{1}{5}s^{-1} & \text{if } 1 \leq \text{s} \leq 2; \\ s^{-1} & \text{if s} > 2. \end{cases} \quad (3.40)$$

The gravitational contribution from each particle is not always calculated. Rather a tree structure is used to identify clusters whose contributions can be treated collectively using a multipole expansion. This significantly reduces the computational cost of the code by reducing the number of calculations required. A GADGET-style multipole acceptance criterion is used and has an error parameter of $\alpha_{_{MAC}} = 10^{-4}$ (Springel et al., 2001). For a comprehensive description of this algorithm see Hubber et al. (2011)

Integration methods

There are a number of integration schemes available in both SEREN and GANDALF. These include 2nd-order Runge-Kutta, 2nd-order Leapfrog (both kick-drift-kick and drift-kick-drift) and 2nd-order Predictor-Corrector. One advantage of 2nd-order Leapfrog integrators is that they only have to calculate the acceleration once, compared to Runge-Kutta which requires two calculations. 2nd-order Leapfrog integrators are also symplectic and are therefore more stable for orbital integration. In principle they are also time-reversable, if one uses a constant global timestep (Hubber et al., 2011).

The optimal timestep for each particle is calculated by determining the minimum value of three separate timesteps. The first of these is a modified Courant condition,

$$\delta t_{\rm COUR} = \gamma_{\rm COUR}\frac{h}{(1+1.2\alpha)c_{\rm HI} + (1+1.2\beta)h_{\rm i}|\nabla\cdot v|_{\rm i}}. \quad (3.41)$$

This version of the Courant condition uses the term $h_{\rm i}|\nabla\cdot v|_{\rm i}$ instead of $|v|_{\rm i}$, replacing the absolute velocity with a frame-independent version. The terms including α and β account for particles that are in the vicinity of shocks. The second condition is an acceleration condition,

$$\delta t_{\rm ACCEL} = \gamma_{\rm ACCEL}\sqrt{\frac{h_{\rm i}}{|a|_{\rm i} + \eta_{\rm a}}}, \quad (3.42)$$

where $\eta_{\rm a}$ is a small positive acceleration to ensure that the denominator does not fall to zero. The final timestep condition is the heating condition,

$$\delta t_{\rm ENERGY} = \gamma_{\rm ENERGY} \frac{u_{\rm i}}{|du/dt|_{\rm i} + \eta_{\rm i}}, \tag{3.43}$$

where $\eta_{\rm i}$ is a small positive heating rate to ensure the denominator does not fall to zero. This timestep limits the fractional change in the internal energy per timestep.

In most simulations there would only be a small number of SPH particles that require very small timesteps. If a global timestep is used, accelerations are recalculated for all particles, irrespective of whether it is required or not. This leads to an unnecessary computational cost with no real benefit. To overcome this one uses hierarchical block-time-stepping (e.g. Aarseth, 2003), which allows each particle to have its own timestep. This timestep is chosen from a binary hierarchy of $\delta t_{\rm n} = 2^{\rm n}\delta t_{\rm MIN}$, where $n = 0, 1, 2, ..., n_{\rm MAX}$. Each particle is then allocated the largest value of $\delta t_{\rm n}$ from the hierarchy which is smaller than its optimal timestep. By restricting the ratio of timesteps to integer powers of two, we ensure that particles are always synchronised at the end of the largest timestep. The acceleration of the particle is then only calculated at the frequency determined by its allocated timestep. A new timestep is automatically recalculated at the end of the current timestep. When the allocated timestep reduces as a result, there will be no problem, because this new timestep will be synchronised with the higher one from which the particle is descending. This is not always the case when a particle timestep increases and we have to ensure that the new timestep is synchronised with the one it is ascending from. We also only allow a particle to ascend by one allocated timestep level at a time. Despite the advantages of this time-stepping method it can cause SPH to perform poorly when neighboring particles have very different timesteps. This effect can be mitigated by broadcasting each particle's allocated timestep to all of its neighbours. If one of the neighbours (j) has an allocated timestep which is more that two levels higher in the hierarchy, then that particle's timestep is automatically reduced to $t_{\rm j} = 4t_{\rm i}$.

3.1.3 Sink Particles

At high density a small region of fluid may be represented by a large number of particles. This can dramatically reduce the minimum timestep in the simulation to a point where the simulation becomes impractical to run. One can avoid this problem by replacing these dense regions with sink particles (Bate et al., 1995). A sink particle is not considered a gas particle and therefore only interacts via gravitational forces.

One can think of a sink particle as a proxy for a star, or star cluster, because it interacts gravitationally with the surrounding gas, whilst also accreting gas particles that become bound to it and fall within its radius. This means that all information relating to the physics within the sink radius is lost. When a sink accretes an SPH particle it assimilates its mass, linear momentum and angular momentum. This is not physical because a star that assimilates all of the angular momentum of the gas it accretes might have unrealistic rotation speeds. Rather the angular momentum should be redistributed to gas surrounding the sink. Hubber et al. (2013) addresses this issue and has created a sink that does just this. However, it is too computationally expensive to be used within the simulations presented in this thesis. Instead we use the standard sink prescription as described by Hubber et al. (2013).

Sink creation

A sink particle must only be introduced into the simulation if the gas it will replace is truly bound. This ensures that random fluctuations in the density do not result in the insertion of an unphysical sink particle. Therefore a SPH particle must pass five conditions before a sink is inserted in its place, these conditions are:

- The candidate particle (particle which is to be replaced by a sink) has a density greater than the sink creation density $\rho_{\rm SINK}$.
- The candidate particle must be at a local gravitational potential minimum, i.e. the gravitational potential at the candidate particle position is lower than that of all of its neighbours.
- The candidate particle and all of its neighbours are gravitationally bound, i.e. the sum of the kinetic and gravitational potential energy is negative.
- The velocity divergence at the position of the candidate particle is negative.
- The candidate particle is not within the accretion radius of another sink particle. This prevents the formation of overlapping sinks.

Sink accretion

Each sink is given an accretion radius ($R_{\rm s}$) which is the radius within which SPH particles will be accreted. This radius is twice the smoothing length, $h_{\rm SINK}$, of a particle with density, $\rho_{\rm SINK}$. This ensures that the radius of each sink particle will be roughly the same as the radius of the kernal of the highest density SPH particle in the simulation, i.e. twice the smoothing length, $h_{\rm h}$.

An SPH particle j is assimilated by the point-mass of a sink, s, if it satisfies two criteria. First, it must have entered the accretion radius of s, i.e.

$$|r_{\rm j} - r_{\rm s}| < R_{\rm s}. \tag{3.44}$$

Second, the mutual non-thermal energy of j and s (i.e. their mutual bulk-kinetic plus gravitational energy), must be negative. If more than one sink is minded to accrete j, j is accreted by the one whose point-mass is closest.

The formation of a sink particle begins by replacing the candidate SPH particle with a sink particle of identical mass. Following this, neighbour particles will be accreted if they satisfy the two conditions discussed above. In cases where the jeans mass is fully resolved, most, if not all of the original SPH particles neighbours will be accreted. However, in cases where the Jeans Mass is not fully resolved (which is the case for some of the simulations in this thesis) not all neighbour particles will pass the conditions, resulting in sink particles with far fewer than 50 SPH particles. In our simulation we find no sink particle forms with less than 10 SPH particles, and while this is not ideal, it confirms that particles are able to fall within the sink radius and become bound. Hence accretion is able to take place and will continue throughout the simulation.

3.2 SEREN AND GANDALF

We use two SPH codes within this thesis, SEREN and GANDALF. SEREN is an established 3D code that is able to carry out simulations requiring SPH, self gravity and N-body dynamics. The user can choose from a number of equation of state and integration schemes, all of which are fully parallelised using OpenMP. It also gives the user the option to use sinks, periodic boundary conditions, radiative cooling (Stamatellos et al., 2007) and simple background gravitational potentials. Further to these native features it also includes a number of modules that add new functionality to the code such as ionising radiation (Bisbas et al., 2009), which is discussed later in the thesis.

GANDALF is the successor to SEREN and is therefore relativity new. It is partly based on some of the algorithms from SEREN but contains many new features and optimisations that significantly improve the speed, functionality and usability of the

code. It has most of the features already present in SEREN, with the additional ability to run with a variety of SPH algorithms. Further to this it is also able to generate initial conditions and includes a tool which can be used to analyse results. As with SEREN, GANDALF is written to be easily modified, allowing a user to add new physics such as ionising radiation. One of the main advantages of GANDALF is that it will be able to take advantage of MPI, something not fully implemented into SEREN. However, MPI was not fully functional at the time the simulations in this thesis were performed.

3.3 Ionizing radiation

SEREN does not natively include a way to simulate the expansion of an HII region. However, it does allow for the addition of new modules which can expand the functionality of the code. Bisbas et al. (2009) took advantage of this and added a module which allows the user to accurately simulate the expansion of the HII region around a single, stationary, ionising source. Ray tracing is used to determine the location of the ionisation front, from which a temperature structure can be inferred. The hierarchical ray structure of HEALPix Górski et al. (2005a) is used to determine the locations and directions of the rays. The routine then walks along each ray until all of the ionising photons are used up, indicating that the ionisation front has been reached.

Rays are emitted using the HEALPix algorithm (Górski et al., 2005a). It generates a set of rays, emanating from $N_{\rm l} = 12 \times 4^{l}$ directions. Here, l represents the level of refinement, with $l = 0$ being the lowest level of refinement. At this level the rays are distributed evenly over the celestial sphere. Each of these rays intersects the celestial sphere at the centre of an approximately square element of solid angle,

$$\delta\Omega_{\rm t} = \frac{4\pi}{N_{\rm l}} \text{steradians.} \tag{3.45}$$

Hence, the angle between neighboring rays is of order $\delta\theta_{\rm l} \sim (\delta\Omega_{\rm l})^{1/2} \sim 2^{-l}$ radians. When an increase in angular resolution is required, HEALPix increases in level, and the ray is split into four child rays. The maximum level allowed is $l = 7$ and this ensures that the routine does not become too computationally expensive.

Rays are split once the linear separation, $r_{\rm j}\delta\theta_{\rm l}$, between them and their neighbours exceeds $f_2 h_{\rm j}$. Here, f_2 is a dimensionless parameter controlling the angular resolution,

h_j is the smoothing length at the current evaluation point, j, and r_j is the distance between the ionising source and the evaluation point. Hence to maintain an acceptable angular resolution, the level, l, must always be,

$$l \geq \log_2 \left(\frac{r_j}{f_2 h_j} \right). \tag{3.46}$$

Smaller values of f_2 give a greater accuracy but require more HEALPix rays and are therefore more computationally expensive. Values of f_2 in the range 1.0 to 1.3 give acceptable results.

If an evaluation point is determined to be inside of the ionisation front then it follows that some of its neighbours will be ionised. Each neighbour is checked and marked as ionised if it satisfies the following two conditions: (a) its coordinates are inside the solid angle of the ray; and (b) its distance from the star is smaller than the distance of the evaluation point. If a SPH particle is marked as ionised it is given a temperature of $T_{ION} = 10000\,\mathrm{K}$. The temperature gradient across the ionisation front is then artificially smoothed to ensure that the particles do not become separated by the large pressure gradient between the hot and cold gas. If this happens the hot and cold particles will no longer be in contact and the HII region will not expand correctly. For more details see Bisbas et al. (2009).

3.4 Initial Conditions

3.4.1 Particle distribution

SPH simulations model a fluid as a finite number of SPH particles, which interact via hydrodynamical forces. In general all particles are given the same mass. This means that the number density of SPH particles is directly proportional to the density of the fluid. Hence, any fluctuation in the particle distribution can lead to a fluctuation in the fluid density. Creating a uniform density gas is therefore difficult and one must reduce the particle noise as much as possible. If the fluctuations in the particle number density are large enough, the simulation can produce structure formation that is purely numerical and does not fully capture the physics.

One way to create a uniform density gas is to place particles on a hexagonally close packed grid. By doing this we reduce the particle noise to zero because all the particles are placed with equal spacing. However, in this situation the particles must be

rotated such that the axis of the grid is not aligned with the simulation axis, otherwise one risks artifacts in their results. The other option is to create a glass, which is a semi uniform distribution of particles that are roughly equidistant from each other.

A glass begins as an ensemble of N randomly distributed particles contained within a single unit cube. These particles are then evolved hydrodynamically within a periodic computational domain, i.e. any particle that leaves the domain on the right boundary will be reintroduced on the left boundary. As a result, any part of the computational domain that has a high density, is overpressured, and slowly expands. Artificial viscosity is used to help dissipate the kinetic energy gained by particles as they move from high to low density regions. Although this process is very effective, it is not perfect and results in an oscillating density structure, i.e. particles move from high density to low density and then back again. However, the amplitude of this oscillation decreases with time and the density variation becomes smaller. We measure this variation using the coefficient of variation of the density,

$$C_{\rm v} = \sigma/\mu. \tag{3.47}$$

Here σ is the standard deviation of the density and μ is the mean density. The simulation is stopped, and the gas considered relaxed once this falls to a value of $C_{\rm v} \sim 1/\sqrt{N}$. The output of this simulation provides the particle positions for the glass, which will be a cube of unit length, containing N particles. Should more particles be required the cube can be replicated and the replicas joined to create a larger domain. This process can be repeated any number of times to create a glass with any number of particles. One can then cut a cloud from this cube and scale the mass and length to the required values.

3.4.2 Equation of state

In this thesis I make the assumption that the gas is ideal, and as a result the pressure and specific internal energy are related by,

$$P = \frac{\rho k_{\rm b} T}{\bar{m}} = (\gamma - 1)\rho u. \tag{3.48}$$

Here $k_{\rm b}$ is Boltzmann's constant, $\bar{m}$ is the mean gas-particle mass, and $\gamma = 5/3$ is the ratio of specific heats. The temperature of the neutral gas is calculated using a

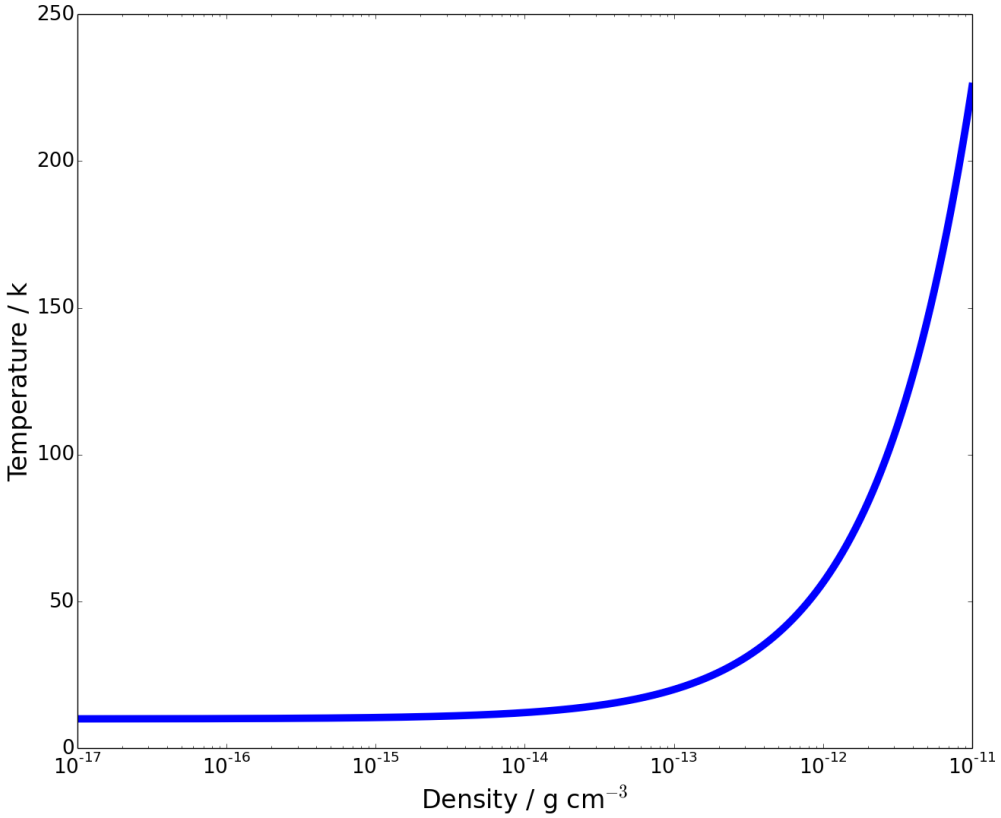

Figure 3.1. The evolution of the temperature as a function of density for a gas initally at $T_0 = 10\,K$ using a barotropic equation of state with critical density $\rho_{\rm CRIT} = 10^{-13}\,{\rm g\,cm^{-3}}$.

barotropic equation of state,

$$T = T_0 \left\{ 1 + \left(\frac{\rho}{\rho_{\rm CRIT}} \right)^{\gamma - 1} \right\}. \tag{3.49}$$

Here $\rho_{\rm CRIT}$ is the critical density and T_0 is the initial temperature of the gas i.e. the temperature of the gas at low densities, $\rho < \rho_{\rm CRIT}$. When the gas is below the critical density it is considered optically thin and is therefore approximately isothermal. When the density rises above the critical density it becomes optically thick and behaves adiabatically. This is illustrated in Fig. 3.1.

3.4.3 Cloud rotations

Numerical artifacts and symmetries can occur when the axis of the simulation is in the same orientation as the one used to create the initial conditions. To avoid this it is best to rotate clouds by random Euler angles. This is done by moving a particle at position $\mathbf{r}$ to,

$$\mathbf{r}_{\text{NEW}} = \begin{bmatrix} \cos\theta\cos\varphi & \cos\phi\sin\varphi + \sin\phi\sin\theta\cos\varphi & \sin\phi\sin\varphi - \cos\phi\sin\theta\cos\varphi \\ -\cos\theta\sin\varphi & \cos\phi\cos\varphi - \sin\phi\sin\theta\sin\varphi & \sin\phi\cos\varphi + \cos\phi\sin\theta\sin\varphi \\ \sin\theta & -\sin\phi\cos\theta & \cos\phi\cos\theta \end{bmatrix} \mathbf{r}. \tag{3.50}$$

Here, we first rotate ϕ radians around the x-axis, followed by a θ radian rotation around the y-axis and then a φ radian rotation around the z-axis.

Chapter 4

What effect does an ionising star have on a cloud already undergoing freefall collapse?

4.1 Motivations

Feedback from massive stars is expected to play an important role in shaping the stellar populations that form in molecular clouds, either by triggering or quenching star formation. However, which one of these effects is most prevalent is still an open question. Recently, numerical work such as that by Walch et al. (2012) and Dale et al. (2012) has suggested that, although ionising feedback does trigger star formation, it also quickly removes gas from the system, reducing the net star formation efficiency. Overall, feedback seems to have a negative effect on star formation by reducing the amount of mass that ends up in stellar objects.

As discussed in Sec. 2.3.1, massive stars produce HII regions which expand and disrupt molecular clouds. The way in which an HII region expands, and its impact on the environment is dependent on both the underlying density structure and also the output of the ionising star. A more uniform cloud is more likely to produce a spherical HII region with a dense shell of material just outside the ionisation front, whereas a fractal cloud produces a more chaotic structure in which gaps open up in the shell. This allows gas to escape which reduces the pressure in the HII region and slows the expansion. In this work we explore what impact the output of the ionising star has on the evolution of a cloud when it is initialised such that it is already undergoing freefall collapse. In this system there will be an additional inward ram pressure, delivered by the infalling gas that may alter the evolution of the HII

region. we first explore, semi-analytically, the relationship between the thermal pressure, ram pressure and gravitational acceleration to determine if there is a critical point at which the HII region is unable to expand. we then use SPH simulations to follow the fragmentation of the shell and the subsequent star formation.

4.2 Initial cloud conditions

The cloud initially has mass $M_{\rm O} = 10^3\,M_\odot$, radius $R_{\rm O} = 2\,{\rm pc}$, uniform density $\rho_0 = 2.02 \times 10^{-21}\,{\rm g\,cm^3}$, and hence freefall time $t_{\rm ff} = 0.63\,{\rm Myr}$. The cloud is constructed from $N_{\rm SPH} = 10^6$ particles cut from a uniform density glass as described in Sec. 3.4.1. This results in a mass resolution of $0.057\,{\rm M}_\odot$, i.e just below the hydrogen-burning limit.

Each particle in the cloud is given an inward radial velocity as if it has fallen from infinity to its current position. Hence the cloud is in homologous free fall collapse with an outer boundary moving at $v_{\rm O} = (2GM_{\rm O}/R_{\rm O})^{1/2}$. The cloud is given the thermal properties we would associate with such a cloud and hence the isothermal sound speed is set to $c_{\rm O} = 0.188\,{\rm km\,s^{-1}}$, corresponding to molecular gas with hydrogen fraction $X_{\rm H} = 0.7$ and a temperature of $T_{\rm iso} = 10\,{\rm K}$.

Ionising radiation is emitted from x=y=z=0 in order to simulate the presence of an ionising star with an ionising output characteristic of an early B / late O type star, hence we assign values in the range $10^{46}\,s^{-1} \leq \dot{\mathcal{N}}_{\rm LyC} \leq 10^{48}\,s^{-1}$. The gravitational field of the star is not included.

4.3 Semi analytic prediction

In advance of carrying out simulations of the system discussed in section 4.2 we develop a semi-analytic model to predict the evolution and position of the ionisation front.

4.3.1 Semi-analytic formulation

We split the evolution of the ionisation front into two phases, the early phase and the late phase. During the early phase the cloud consists of three regions: the HII region, the shocked shell of neutral gas and the unshocked, infalling neutral gas. The late phase begins once all of the outer neutral gas has accreted onto the shell.

At this point the system consists of an HII region and a shell. We therefore define the time of transition $t_{\rm tran}$ as the time the early phase ends and the late phase begins. At this time $R_{\rm IN}(t_{\rm tran}) = R_{\rm SH}(t_{\rm tran})$, where $R_{\rm IN}$ is the outer radius of the infalling gas and $R_{\rm SH}$ is the position of the shock front at the outer boundary of the shell.[1]

The collapsing cloud

For this part of the dynamics we are concerned with the parts of the cloud in freefall collapse i.e. the parts that have yet to come in contact with the HII region or shell. We consider a small element at radius $r_{\rm o}$, which, if in freefall is initially ($t = 0$) moving inwards with velocity,

$$\begin{aligned} v_{\rm IN}(r_{\rm 0}) &= \frac{v_{\rm O} r_{\rm O}}{R_{\rm O}} \\ &= \left(\frac{2GM_{\rm O}(r_{\rm O}/R_{\rm O})^3}{r_{\rm O}} \right)^{1/2} . \end{aligned} \tag{4.1}$$

As the cloud is in homologous freefall collapse we do not expect the mass interior to this element to change as the radius r decreases. However we do expect the inward velocity to increase according to,

$$v_{\rm IN}(r) = \left(\frac{2GM_{\rm O}(r_{\rm O}/R_{\rm O})^3}{r} \right)^{1/2} . \tag{4.2}$$

From Eqn. 4.2 we can then determine the time it would take for an element at radius $r_{\rm 0}$ to collapse to radius r,

$$\begin{aligned} t_{\rm IN}(r) &= \int_{r'=r_{\rm O}}^{r'=r} \frac{dr'}{-v(r')} \\ &= \frac{2}{3} \left(\frac{R_{\rm O}^3}{2GM_{\rm O}} \right)^{1/2} \left\{ 1 - \left(\frac{r}{r_{\rm O}} \right)^{3/2} \right\} . \end{aligned} \tag{4.3}$$

Using Eqn. 4.3 we can then determine the freefall time, which is the time taken for the entire cloud to collapse to the center, in the absence of an ionising star,

$$t_{\rm O} = \frac{2}{3} \left(\frac{R_{\rm O}^3}{2GM_{\rm O}} \right)^{1/2} . \tag{4.4}$$

[1] subscript IN refers to an infalling gas property and subscript SH refers to a shell property

Alternatively we can say the radius of of an element that was initially at $r_{_0}$ is given by,

$$r_{_{\rm IN}}(t) \;=\; r_{_{\rm O}} \left\{ 1 \,-\, \left(\frac{t}{t_{_{\rm O}}} \right) \right\}^{2/3} . \tag{4.5}$$

Using Eqn. 4.5 we can re-write the evolution of $R_{_{\rm IN}}$, $\rho_{_{\rm IN}}$, $v_{_{\rm IN}}$ and $M_{_{\rm IN}}$ as a function of time,

$$R_{_{\rm IN}}(t) \;=\; R_{_{\rm O}} \left\{ 1 \,-\, \left(\frac{t}{t_{_{\rm O}}} \right) \right\}^{2/3} , \tag{4.6}$$

$$\rho_{_{\rm IN}}(t) \;=\; \rho_{_{\rm O}} \left\{ 1 \,-\, \left(\frac{t}{t_{_{\rm O}}} \right) \right\}^{-2} . \tag{4.7}$$

$$v_{_{\rm IN}}(r,t) \;=\; v_{_{\rm O}} \left(\frac{r}{R_{_{\rm O}}} \right) \left\{ 1 \,-\, \left(\frac{t}{t_{_{\rm O}}} \right) \right\}^{-1} , \tag{4.8}$$

$$M_{_{\rm IN}}(r,t) \;=\; M_{_{\rm O}} \left(\frac{r}{R_{_{\rm O}}} \right)^3 \left\{ 1 \,-\, \left(\frac{t}{t_{_{\rm O}}} \right) \right\}^{-2} . \tag{4.9}$$

The HII region

We now consider the HII region, making the assumption that it is in ionisation balance and that the shell outside the HII region is thin, i.e. $R_{_{\rm HII}} = R_{_{\rm SH}}$. In this case, the radius of the HII region, $R_{_{\rm SH}}$, is related to its density, $\rho_{_{\rm HII}}$, by,

$$\frac{4\pi R_{_{\rm SH}}^3(t)}{3}\, \alpha_{_{\rm B}} \left(\frac{\rho_{_{\rm HII}}(t)}{m} \right)^2 \;=\; \dot{\mathcal{N}}_{_{\rm LyC}} . \tag{4.10}$$

Here $\alpha_{_B} = 2.6 \times 10^{-13}\,{\rm cm^3\,s^{-1}}$ is the Case B recombination coefficeient (i.e. only the recombinations into excited states are counted). The mass $m = 2.4 \times 10^{-24}\,g$ is the mass associated with a single hydrogen atom, after taking into account other elements; and $\dot{\mathcal{N}}_{_{\rm LyC}}$ is the rate of emission of ionising photons by the ionising star. Here we make the assumption that all ionising photons are used balancing recombination in the bulk of the HII region, rather than ionising new material.

We use Eqn. 4.10 to work out the initial radius of the HII region (the Strømgren radius),

$$R_{\rm SH}(0) = \left(\frac{3\dot{\mathcal{N}}_{\rm LyC}}{4\pi\alpha_{\rm B}}\right)^{1/3} \left(\frac{\rho_{\rm O}}{m}\right)^{-2/3}. \tag{4.11}$$

$$\tag{4.12}$$

We also write the density $\rho_{\rm HII}$ and mass $M_{\rm HII}$ of the HII region as a function of $R_{\rm SH}$,

$$\rho_{\rm HII}(t) = \left(\frac{3\dot{\mathcal{N}}_{\rm LyC}}{4\pi\alpha_{\rm B}}\right)^{1/2} m\, R_{\rm SH}^{-3/2}(t)\,, \tag{4.13}$$

$$\begin{aligned} M_{\rm HII}(t) &= \frac{4\pi R_{\rm SH}^3(t)\rho_{\rm HII}(t)}{3} \\ &= \left(\frac{4\pi\dot{\mathcal{N}}_{\rm LyC}}{3\alpha_{\rm B}}\right)^{1/2} m\, R_{\rm SH}^{3/2}(t)\,. \end{aligned} \tag{4.14}$$

Evolution of the shell

In the early phase of shell evolution, the shell is sandwiched between the ionised gas and infalling gas. Its mass is given by,

$$M_{\rm SH}(t) = M_{\rm SUM}(t) - M_{\rm HII}(t)\,, \tag{4.15}$$

where $M_{\rm SUM}$ is mass of the HII region and shell combined i.e. $M_{\rm SUM} = M_{\rm IN}(R_{\rm SH}(t), t)$. In determining the motion of the shell we must take into account the gravitational force, the pressure of the HII region and the ram pressure exerted on the shell due to the in-falling gas. The gravitational accelerations at the inner and outer edges of the shell are given by,

$$a_{\rm INNER}(t) = -\frac{GM_{\rm HII}(t)}{R_{\rm SH}^2(t)}, \tag{4.16}$$

and,

$$a_{\rm OUTER}(t) = -\frac{G\{M_{\rm HII}(t) + M_{\rm SH}(t)\}}{R_{\rm SH}^2(t)}. \tag{4.17}$$

Because the shell is assumed to be thin, the total gravitational acceleration can be worked out by calculating the arithmetic mean of these two terms,

$$a_{\rm GRAV}(t) \;=\; -\frac{G\{2M_{\rm HII}(t)+M_{\rm SH}(t)\}}{2R^2_{\rm SH}(t)}, \tag{4.18}$$

and can be simplified using Eqn. 4.15 to give the outward acceleration due to gravity,

$$a_{\rm GRAV}(t) \;=\; -\frac{G\{M_{\rm SUM}(t)+M_{\rm HII}(t)\}}{2R^2_{\rm SH}(t)}\,. \tag{4.19}$$

The ram pressure is given by,

$$P_{\rm RAM}(t) \;=\; \rho_{\rm IN}(t)\{v_{\rm RAM}(t)+\dot{R}_{\rm SH}(t)\}^2\,, \tag{4.20}$$

where $v_{\rm RAM}$ is the inward velocity of the gas accreting onto the shell, i.e. $v_{\rm RAM} = v_{\rm IN}(R_{\rm SH}(t),t)$. One can combine this with the pressure exerted by the HII region,

$$P_{\rm HII}(t) \;=\; \rho_{\rm HII}(t)c^2_{\rm HII}\,, \tag{4.21}$$

to obtain the net outward hydrodynamic acceleration,

$$a_{\rm HYDRO}(t) \;=\; \frac{4\pi R^2_{\rm SH}(t)\{P_{\rm HII}(t)-P_{\rm RAM}(t)\}}{M_{\rm SH}(t)}\,,\ \text{for } t<t_{\rm TRAN}\,, \tag{4.22}$$

where $c_{\rm HII}$ is the sound speed in the ionised gas. We note that the only difference between the early stage and late stage is that in the late stage there will be no ram pressure, hence Eqn. 4.22 will become,

$$a_{\rm HYDRO}(t) \;=\; \frac{4\pi R^2_{\rm SH}(t)P_{\rm HII}(t)}{M_{\rm SH}(t)}\,,\ \text{for } t\geq t_{\rm TRAN}\,. \tag{4.23}$$

Introducing Dimensionless Variables

In order to simplify the equations for the numerical calculations we introduce the following dimensionless variables,

$$\xi \;=\; \frac{R}{R_{\rm O}}\,, \tag{4.24}$$

$$\tau \;=\; \frac{t}{t_{\rm O}}\,, \tag{4.25}$$

$$\mu = \frac{M}{M_{\rm O}}, \tag{4.26}$$

$$\delta = \frac{\rho}{\rho_{\rm O}}, \tag{4.27}$$

$$\nu = \frac{t_{\rm O} v}{R_{\rm O}}, \tag{4.28}$$

and the dimensionless parameters,

$$\eta_{\rm LyC} = \left(\frac{4\pi \dot{N}_{\rm LyC} R_{\rm O}^3}{2\alpha_{\rm B}}\right)^{1/2} \frac{m}{M_{\rm O}}, \tag{4.29}$$

$$\eta_{\rm II} = \left(\frac{c_{\rm HII}}{v_{\rm O}}\right)^2, \tag{4.30}$$

$$\eta_{\rm I} = \left(\frac{c_{\rm HI}}{v_{\rm O}}\right)^2. \tag{4.31}$$

Here $c_{\rm HI}$ and $c_{\rm HII}$ are the sound speeds of the neutral and ionised gas respectively.

We now proceed to convert our equations to the dimensionless system for both the early and late phase. The dimensionless radius (Eqn. 4.6) of the edge of the infalling cloud becomes,

$$\xi_{\rm IN}(\tau) = \begin{cases} (1-\tau)^{2/3}, & \tau < \tau_{\rm TRAN}, \\ \text{undefined}, & \tau \geq \tau_{\rm TRAN}. \end{cases} \tag{4.32}$$

The density and inward velocity of any point within the infalling cloud (Eqns. 4.7 and 4.8) become,

$$\delta_{\rm IN}(\tau) = \begin{cases} (1-\tau)^{-2}, & \tau < \tau_{\rm TRAN}\,, \\ \text{undefined}, & \tau \geq \tau_{\rm TRAN}\,, \end{cases} \tag{4.33}$$

$$\nu_{\rm IN}(\xi,\tau) = \begin{cases} \frac{2}{3}\xi(1-\tau)^{-1}, & \tau < \tau_{\rm TRAN}\,; \\ \text{undefined}, & \tau \geq \tau_{\rm TRAN}\,. \end{cases} \tag{4.34}$$

Using Eqn. 4.39 we can specify the dimensionless velocity of the gas about to impact the accretion shock,

$$\nu_{\rm RAM}(\tau) \;=\; \begin{cases} \frac{2}{3}\xi_{SH}(\tau)(1-\tau)^{-1}, & \tau < \tau_{\rm TRAN}\,, \\ \text{undefined}, & \tau \geq \tau_{\rm TRAN}\,. \end{cases} \tag{4.35}$$

The mass and density of the HII region (Eqns. 4.14 and 4.13) become,

$$\delta_{HII}(\tau) \;=\; \eta_{\rm LyC}\xi_{\rm SH}^{-3/2}(\tau)\,, \tag{4.36}$$

$$\mu_{HII}(\tau) \;=\; \eta_{\rm LyC}\xi_{\rm SH}^{3/2}(\tau)\,. \tag{4.37}$$

From Eqn. 4.15, the shell mass becomes,

$$\mu_{SH}(\tau) \;=\; \mu_{\rm SUM}(\tau) - \mu_{\rm HII}(\tau)\,, \tag{4.38}$$

where $\mu_{\rm SUM}$ is the total mass of the shell and HII region, and is given by,

$$\mu_{\rm SUM}(\tau) \;=\; \begin{cases} \xi_{\rm SH}^{3}(1-\tau)^{-2}, & \tau < \tau_{\rm TRAN}\,; \\ 1, & \tau \geq \tau_{\rm TRAN}\,. \end{cases} \tag{4.39}$$

Using the above we can then derive dimensionless forms for the gravitational and hydrodynamic acceleration (Eqns. 4.19,4.22 and 4.23),[2]

$$\xi''_{\rm GRAV}(\tau) \;=\; -\frac{\mu_{\rm SUM}(\tau)+\mu_{\rm HII}(\tau)}{9\xi_{\rm SH}^{2}(\tau)}\,, \tag{4.40}$$

$$\xi''_{\rm HYDRO}(\tau) \;=\; \frac{4\xi_{\rm SH}^{2}(\tau)}{3\mu_{\rm SH}(\tau)} \begin{cases} \eta_{\rm II}\delta_{\rm HII}(\tau) - \delta_{\rm IN}(\tau)\left(\frac{3\xi'_{SH}(\tau)}{2} + \frac{\xi_{\rm SH}(\tau)}{1-\tau}\right)^{2}, & \tau < \tau_{\rm TRAN}\,; \\ \eta_{\rm II}\delta_{\rm HII}(\tau), & \tau \geq \tau_{\rm TRAN}\,. \end{cases} \tag{4.41}$$

The net acceleration of the shell is given by the sum of these contributions,

$$\xi''_{\rm SH}(\tau) \;=\; \xi''_{\rm GRAV}(\tau) + \xi''_{\rm HYDRO}(\tau). \tag{4.42}$$

[2] Here ξ'' and ξ' are the dimensionless derivatives $\xi'' = \frac{d^2\xi}{d\tau^2}$ and $\xi' = \frac{d\xi}{d\tau}$.

4.3.2 Semi-analytic solution

We solve the Eqns. 4.32 to 4.42 using a fourth order Runge-Kutta based, C^{++} routine. We predict the location of the ionisation front over a 1.6 Myr period ($2.5t_o$) for the cloud discussed in Sec.4.2, under the influence of ionising stars with outputs in the range $10^{46}\,\mathrm{s}^{-1} < \dot{\mathcal{N}}_{\mathrm{LyC}} < 10^{48}\,\mathrm{s}^{-1}$. We identify three possible evolutions of the HII region; it may expand and then contract, expand and then become approximately stationary before expanding once more, or expand continuously; these will be referred to as Cases 1, 2 and 3 respectively and are summarised in Tab. 4.1.

Table 4.1. This table details the three different types of evolutions we identify in our semi-analytic model.

Case	Ionising Output ($\dot{\mathcal{N}}_{\mathrm{LyC}}$)	Description
1	$1.4 \times 10^{47}\,\mathrm{s}^{-1}$	expand - contract
2	$2.4 \times 10^{47}\,\mathrm{s}^{-1}$	expand - contract - approximately stationary - expand
3	$3.4 \times 10^{47}\,\mathrm{s}^{-1}$	expand

We begin by examining Case 3, which is shown as a green line in Fig. 4.1. Initially the HII region undergoes a rapid expansion phase. During this phase we would expect the mass of the shell to increase as neutral gas from the cloud accretes onto the surface of the shell. This increases the weight, and in combination with the ram pressure (due to the inward velocity) leads to a deceleration in the rate of expansion. This deceleration is quite notable, with the HII region becoming almost stationary for $0.4\,\mathrm{Myr} < \mathrm{t} < 0.6\,\mathrm{Myr}$. After the last of the neutral material has fallen onto the shell the only factor resisting expansion is gravity, and in this example this is not large enough to dominate over the thermal pressure, and the shell once again begins to expand.

The blue line of Fig. 4.1 shows the evolution of Case 1 in which there is an initial rapid expansion phase. In this case we notice that the combination of the ram pressure and the weight of the shell are able to slow and reverse the expansion of the HII region before the last of the neutral gas has accreted onto the shell. At this ionising output the thermal pressure is unable to support the weight of the shell, hence the shell continues to contract.

The most interesting case is Case 2, shown by the red line of Fig. 4.1. In this case we once again see the initial rapid expansion of the HII region. Similarly to Case

1 we find that the combination of the ram pressure and the weight of the shell is able to turn around the expansion of the HII region and we see it begin to contract. The ram pressure plays a critical role in this turn around. Once the last of the neutral material has accreted onto the shell, the ram pressure vanishes and the contraction slows and transitions back into expansion. It is important to note that this effect is only present for a small number of ionising outputs and is unlikely to occur in simulations that have any pre-existing density structure in the neutral gas.

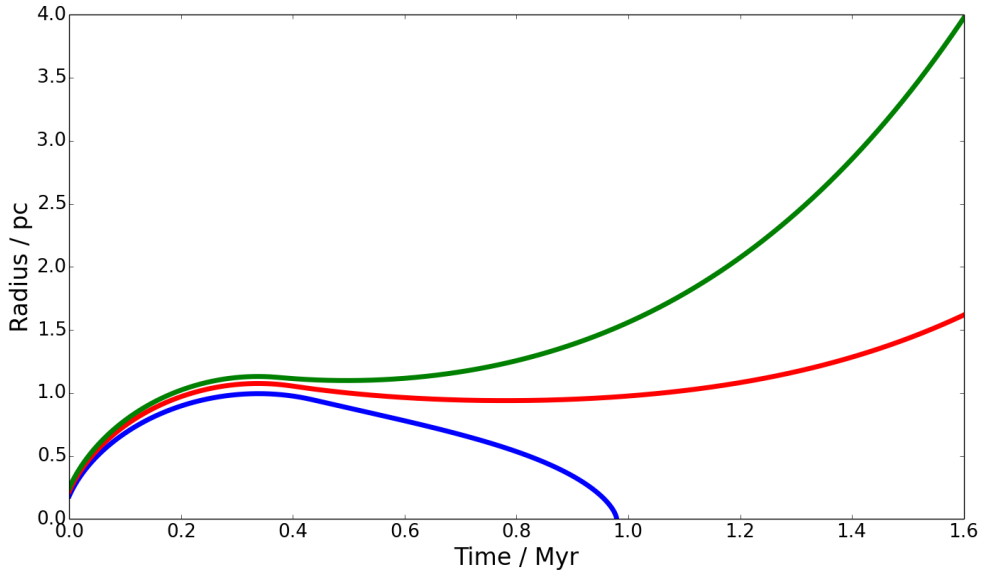

Figure 4.1. The predicted radius of the ionisation front as a function of time over a 1.6 Myr period. The Lyman outputs of the stars are $\dot{\mathcal{N}}_{\rm LyC} = 1.4 \times 10^{47}\,{\rm s}^{-1}$, $\dot{\mathcal{N}}_{\rm LyC} = 2.4 \times 10^{47}\,{\rm s}^{-1}$ and $\dot{\mathcal{N}}_{\rm LyC} = 3.4 \times 10^{47}\,{\rm s}^{-1}$ for the blue, red and green lines respectively. In these three lines we see the transition from a contracting evolution to one of expansion, as the ionising output is increased.

4.4 SIMULATIONS

In order to test our semi-analytic predictions, and also explore any structure formation, we carry out hydrodynamical simulations of the cloud used in the predictions (Sec. 4.3.2 and discussed in Sec. 4.2). In total we carry out three detailed simulations, each containing of order $N_{\rm SPH} = 10^6$ particles and a centrally located ionising star. The ionising outputs are chosen to represent the most interesting cases as predicted by the semi analytic solution (Sec: 4.3), hence we give the sources outputs of $\dot{\mathcal{N}}_{\rm LyC} = 1.4 \times 10^{47}\,{\rm s}^{-1}$, $\dot{\mathcal{N}}_{\rm LyC} = 2.4 \times 10^{47}\,{\rm s}^{-1}$ and $\dot{\mathcal{N}}_{\rm LyC} = 3.4 \times 10^{47}\,{\rm s}^{-1}$.

4.4.1 Numerical Setup

The simulations are carried out using the SPH code SEREN, along with the ionisation module added by Bisbas et al. (2009) to simulate an ionising source; these are discussed in more detail in chapter Sec. 3.2 and Sec. 3.3 respectively. A binary tree is used to compute gravitational forces and collate particle neighbour lists. The grad-h formulation of the evolution equations is invoked (Price and Monaghan, 2004), and they are solved with a second-order leapfrog integrator. Artificial viscosity is treated using the method of Monaghan (1997), with parameters with $\alpha = 1$ and $\beta = 2$. Sinks are introduced and evolved using the standard procedure described in Hubber et al. (2013), with $\rho_{\rm SINK} = 10^{-12}\,{\rm g\,cm^{-3}}$; hence condensations which are converted into sinks are already well into their Kelvin-Helmholtz contraction phase, and their properties are essentially independent of the choice of $\rho_{\rm SINK}$. The resolution-parameter is set to $\eta = 1.2$, so that an SPH particle typically has ~ 56 neighbours. The simulations are run for $2.5t_{_0}$, or until the shell has converged onto the centre. The state of the simulation is logged every 0.1 Myr in order to fully capture the evolution of both the HII region and the neutral gas. A barotropic equation of state of the form discussed in Sec. 3.4.2 is used with $T_{_0} = 10\,{\rm K}$ and $\rho_{\rm CRIT} = 10^{-14}\,{\rm g\,cm^{-3}}$.

4.4.2 Evolution of the HII region

Due to the spherical nature of the simulations the radius, $R_{\rm SH}$, of the shell can be estimated by locating the peak density; this assumption will hold as long as the shell remains intact. As the shell is thin, and lies just outside the HII region, $R_{\rm SH}$ is also a good proxy for the edge of the HII region, i.e the ionsiation front. We also calculate an approximate thickness for the shell. The outer edge of the shell is first located by slowly moving out from the peak density until the density is no longer changing. At this point the uniform neutral material of the cloud has been reached and the outer edge of the shell has been found. The inner edge is located by finding the location of the last ionised particle.

In Fig. 4.2 we plot the evolution of the shell for the three simulations, the green line shows the radius of the peak density, the blue lines represent the outer edges of the shell and the red line is the predicted evolution of the ionisation front. These figures show that the simulation results and the predictions agree quite well. The erratic behavior of the peak density and shell edges in Case 3 at $t > 1.5\,{\rm Myr}$ is due to the shell breaking up, resulting in poorly defined shell boundaries. We note that our prediction is in best agreement for low output sources in which the evolution

is slower and there is less disruption to the shell. For the larger outputs we see an over prediction of the ionisation front radius, which is not surprising as our models assume that the shell remains spherically symmetric and does not break apart. Any hole in the shell would result in a loss of pressure and hence a reduction in expansion rate, this is visible in simulations with higher ionising outputs. We note that in all three simulations the shell thickness also appears to evolve, this is most clear in the panel A. Initially the shell is thick, but, as the simulation progresses the shell becomes thinner for a short period. Despite this change in the shell thickness we do not see much divergence from the semi-analytical prediction, which assumes the shell is thin. Hence, it is unlikely that the thinning of the shell is playing a large role in the evolution of the HII region.

4.4.3 EVOLUTION OF THE SHELL ABOVE THE IONISATION FRONT

Star formation

The star formation rate in these simulations is highly dependent on the evolution of the HII region; in fact significant star formation is only present in a small number of cases, specifically the cases in which the evolution of the shell contains both a contraction phase and a long approximately stationary period. In order to explain this we will examine each of the three cases individually, beginning with Case 3 ($\dot{\mathcal{N}}_{\rm LyC} = 3.4 \times 10^{47}\,{\rm s}^{-1}$), in which the HII region undergoes continuous expansion. In the bottom row of Fig. 4.3 we plot 4 snapshots from the simulation, each snapshot shows the column density of a slice of $-0.1\,{\rm pc} < {\rm z} < 0.1\,{\rm pc}$ through the simulation. The simulation progresses from left to right with snapshots at times $t = 0.10\,{\rm Myr}$, $t = 0.40\,{\rm Myr}$, $t = 0.95\,{\rm Myr}$ and $t = 1.35\,{\rm Myr}$. As discussed, the HII region initially expands, and by $t = 0.40\,{\rm Myr}$ the last of the neutral gas has accreted onto the shell, at this point the shell begins to become unstable. These instabilities seed the formation of the structures we see in the third and fourth panel. At this time the shell is still expanding and the structures do not form with a high enough density to resist the evaporation caused by the ionising radiation, hence few stars form.

We next examine Case 1 ($\dot{\mathcal{N}}_{\rm LyC} = 1.4 \times 10^{47}\,{\rm s}^{-1}$). Here the HII region initially expands before being overcome by the weight of the shell and contracting. We show the four snapshots from this simulation, in the top four panels of Fig. 4.3. In this simulation we see the HII region begins to contract just after the last of the neutral material has accreted. We also notice that though the density of the shell increases as the HII region contracts it does not develop high density cores. Hence there is very little star

formation in the shell as it contracts, in fact we only get star formation when the shell has converged onto the centre.

Finally we examine Case 2 ($\dot{\mathcal{N}}_{\rm LyC} = 2.4 \times 10^{47}\,{\rm s}^{-1}$), here the evolution has both a contraction phase and a long approximately stationary period. The middle four images of Fig. 4.3 show the snapshots from the simulation. In this case we see that the shell of neutral gas just outside the ionisation front contracts as a result of the ram pressure of the accreting gas. This increases the density in the shell, which we can see when we compare the $t = 0.42\,{\rm Myr}$ and $t = 0.90\,{\rm Myr}$ images. In the $t = 0.90\,{\rm Myr}$ snapshot we can again see the development of substructure within the shell. What is important to note is that these structures have much higher density than the ones in Case 3 and are therefore more likely to form stars.

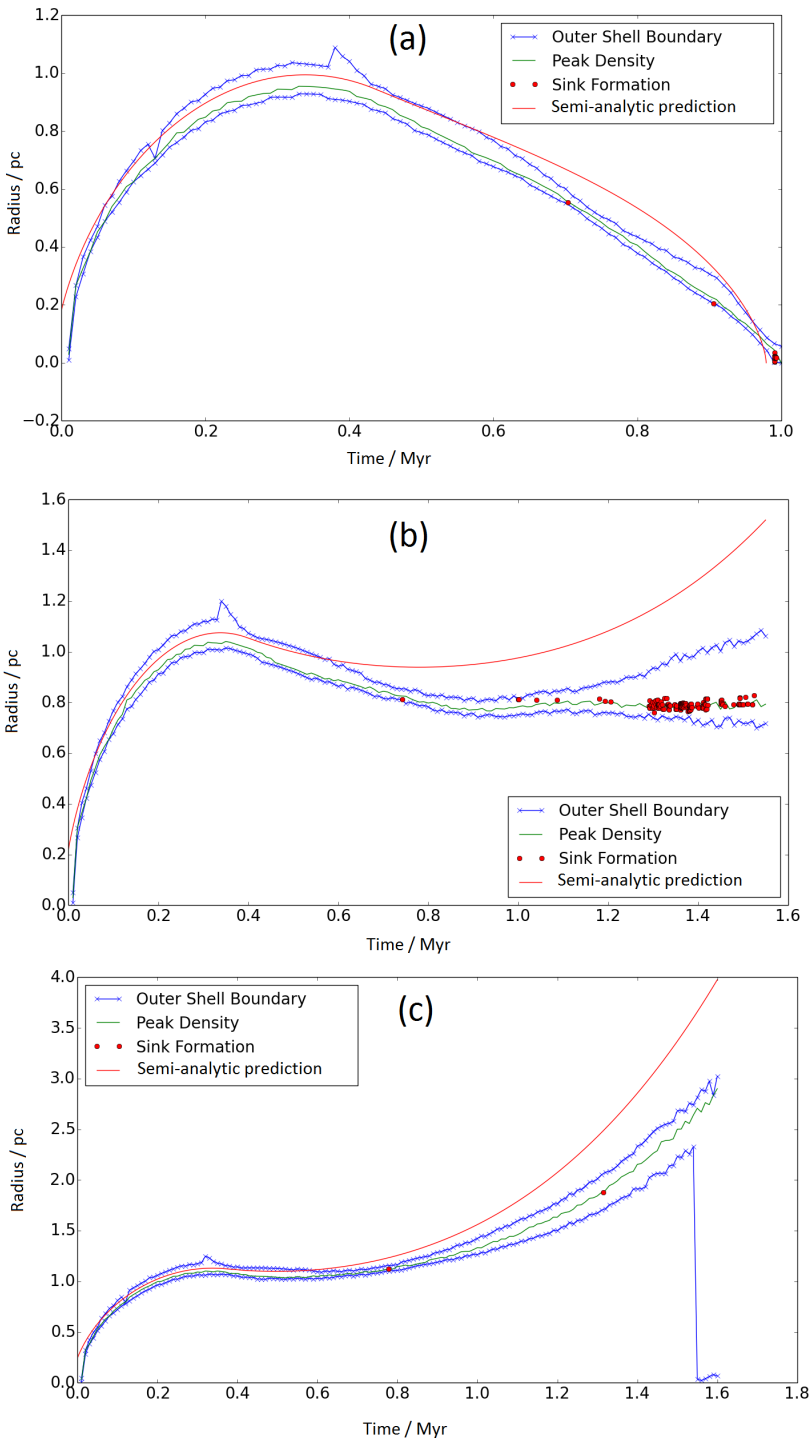

Figure 4.2. The evolution of the shell for the cases where we include infall velocity. The ionising outputs are $\dot{\mathcal{N}}_{\rm LyC} = 1.4 \times 10^{47}\ {\rm s}^{-1}$, $\dot{\mathcal{N}}_{\rm LyC} = 2.4 \times 10^{47}\ {\rm s}^{-1}$ and $\dot{\mathcal{N}}_{\rm LyC} = 3.4 \times 10^{47}\ {\rm s}^{-1}$ for the top , middle and bottom plots respectively. The green line is the radius of the peak density of the shell, the blue lines represent the inner and outer boundaries of the shell, and the red line is the radius of the ionisation front as predicted by the semi-analytic method discussed in Sec. 4.3. The red circles indentify the radii and times at which new stars form.

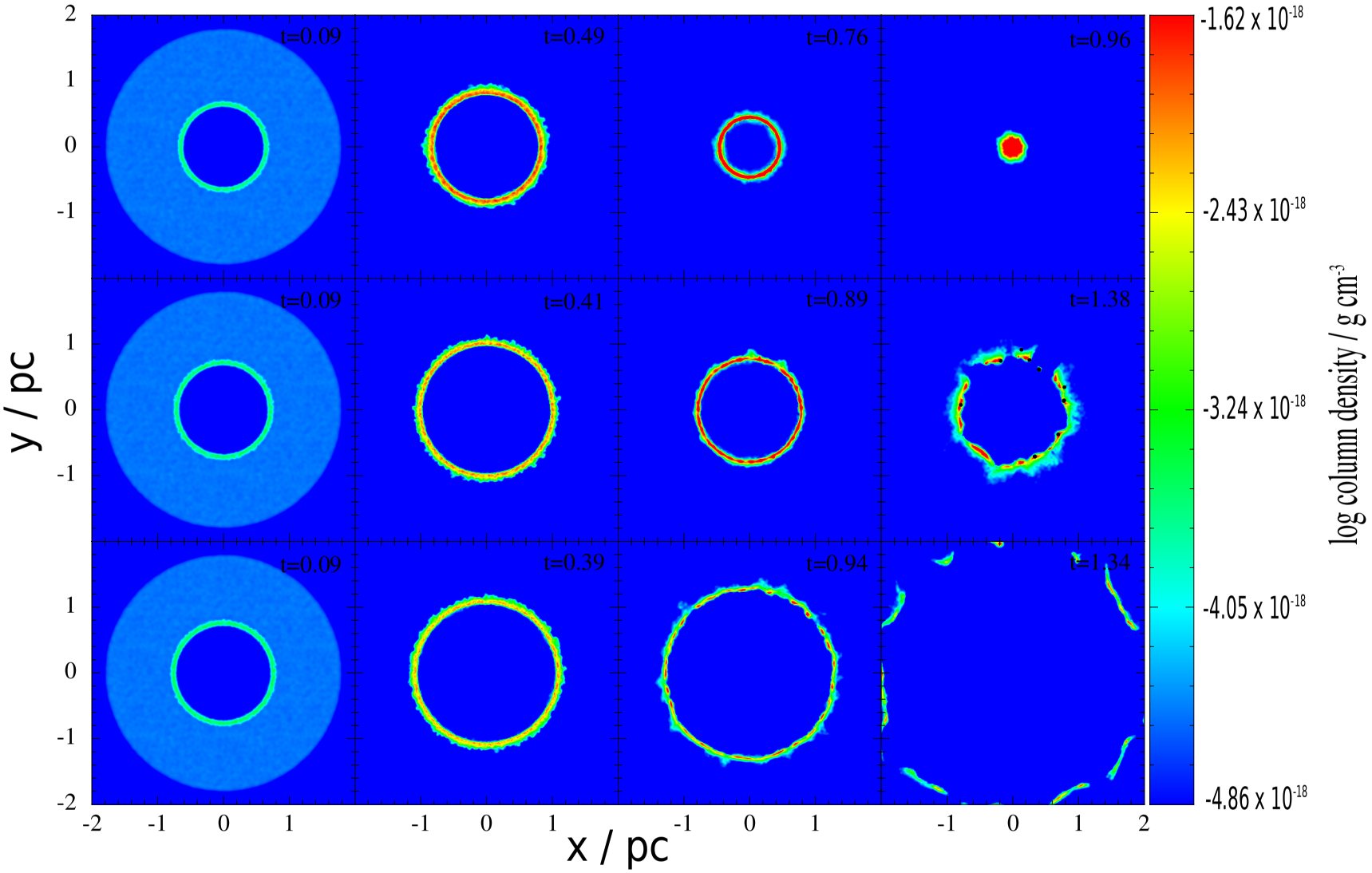

Figure 4.3. The evolution of the shell for the cases where we include infall velocity. Each panel shows a the volume density ($log_{10}(\frac{\Sigma}{\delta\xi}\mathrm{g\,cm^{-2}})$) of a slice ($-0.1\,\mathrm{pc} < \delta\xi < 0.1\,\mathrm{pc}$). The ionising out puts are $\dot{\mathcal{N}}_{\mathrm{LyC}} = 1.4 \times 10^{47}\,\mathrm{s}^{-1}$, $\dot{\mathcal{N}}_{\mathrm{LyC}} = 2.4 \times 10^{47}\,\mathrm{s}^{-1}$ and $\dot{\mathcal{N}}_{\mathrm{LyC}} = 3.4 \times 10^{47}\,\mathrm{s}^{-1}$ for the top, middle right and bottom rows respectively.

Shell break up

In all but the simulations with the lowest ionising output, we find that the swept up shell is unable to remain intact. This is the result of instabilities, seeded by the underlying noise in the particle distributions (as discussed in Sec. 3.4.1). This is not unexpected, as Vishniac (1983) showed that a dense fluid resting on one of lower density is prone to instabilities. In Fig. 4.4 we see an example of a shell that has been broken apart into many smaller structures. Among these structures we see examples of both bright rimmed clouds and pillars. Box A in Fig. 4.4 illustrates an example of a bright rimmed cloud. Such structures have been studied in detail by Bisbas et al. (2011). When we compare the bright rimmed cloud shown in Fig. 4.4 to Fig. 7 from Bisbas et al. (2011) we find many common features such as the mushroom shape with a high density region along the leading edge (edge facing the star). As the structure is exposed to the ionising radiation of the star it is undergoing evaporation and is moving away from the star due to the rocket effect (Oort and Spitzer, 1955; Kahn, 1954).

Box B in Fig. 4.4 shows an example of a pillar from our simulations. Again we can compare this with Bisbas et al. (2011) who in their Fig. 8 show a simulation of pillar formation. In both cases we see a long extended structure with a dense tip at the leading edge. In general pillars extend away from the star, although we note that our pillars are not as straight as those of Bisbas et al. (2011), we suspect this is because the pillars in our simulations form as a result of structures in a shell of material rather than a single cloud of gas with no background density structure or history. Again the pillar is undergoing evaporation due to the ionising photons from the star and is moving away from the star due to the rocket effect.

4.5 SUMMARY

In this work we have developed a semi-analytic model to describe the evolution of an HII region contained within a cloud that has collapsed from infinity. We find that by adding the inward radial velocity we introduce an effect in which the ionisation front contracts slightly before becoming stationary for a long period of time. This can then promote star formation due to the increased density of the shell. However this phenomena only occurs for a very small range of Lyman outputs and outside this range there is very little star formation. This work shows that it is very difficult to trigger star formation in a uniform density cloud with a centrally located ionising star. We do however find that in most cases we can produce the structures we see in

observation, such as bright rimed clouds and pillars. These structures produce stars along the edge facing the ionising star. This work also shows that only the most massive stars are able to form and maintain an HII region capable of disrupting a cloud, whether that be by triggering star formation or blowing the cloud apart. These results are in agreement with the work of Dale et al. (2005) who find that feedback is less effective in dense gas. We find similar effects in the sense that HII regions are unable to form and be effective in some environments.

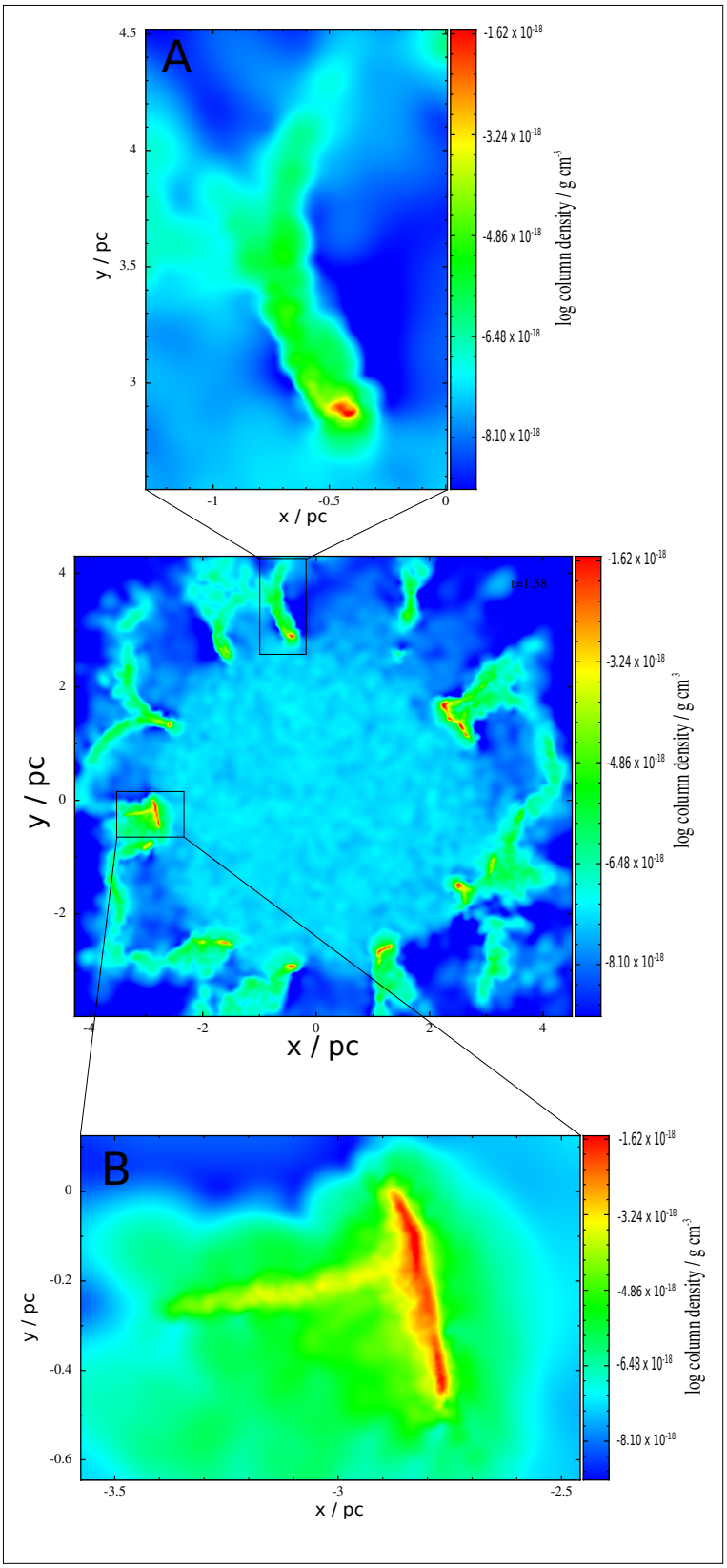

Figure 4.4. A slice ($-0.1\,\mathrm{pc} < \delta\xi < 0.1\,\mathrm{pc}$) from a simulation with ionising output $\dot{\mathcal{N}}_{\mathrm{LyC}} = 3.4 \times 10^{47}\ \mathrm{s}^{-1}$. In this plot colour represents volume density ($log_{10}(\frac{\Sigma}{\delta\xi}\mathrm{g\,cm}^{-2})$) .Box A indicates an example of a bright rimed cloud, with box B indicating an example of a pillar.

Chapter 5
Cloud-cloud collisions : Effect of the collision velocity

In the previous chapter I have shown that stars with a range of masses are able to excite HII regions. However, only the HII regions of the most massive stars are capable of significantly disrupting the collapse of a molecular cloud. Walch et al. (2012) and Dale et al. (2012) both show that the disruption caused by an expanding HII region can terminate star formation very rapidly, and in some cases completely destroy the cloud. They also find that this process is dependent on both the density and the substructure of the cloud, suggesting that the environment is a key factor in determining how destructive the HII region is. It is therefore important to study a range of environments and how their evolutions are changed by the feedback from massive stars.

The layer formed as a result of a cloud-cloud collision is an interesting star formation environment which has the potential to form massive stars which has been studied by a range of authors (Micic et al., 2013; Inoue and Fukui, 2013; McLeod and Whitworth, 2013; Elmegreen and Elmegreen, 1978; Ostriker and Cowie, 1981; Vishniac, 1983; Whitworth et al., 1994). The morphology of the layer means that any HII regions that form may become bi-polar as they break out of the layer in the direction of the collision. In this chapter we explore the type of stellar population that forms as a result of a cloud-cloud collision to determine if massive stars (capable of producing large amounts of ionising radiation) are able to form. Previous work (Takahira et al., 2014) suggests they will, due to the high surface density of the shocked compressed layer and the large mass of the cores caused by fragmentation. The mass of these fragments is dependent on the velocity at which the clouds collide (Whitworth et al.,

1994). We therefore carry out a number of simulations at different collision velocities to determine how this changes the stellar population that forms. We do not include ionisation at this stage, rather we end the simulations at the time ionisation would begin to terminate star formation. By doing this we are able to explore the star formation process prior to the introduction of feedback. In chapter 8 we explore how feedback goes on to alter star formation if the simulations are allowed to continue. Work from this chapter was previously published in Balfour et al. (2015).

5.1 SIMULATION SET-UP

5.1.1 INITIAL CONDITIONS

Each cloud in our simulation is presumed to be part of a larger, approximately virialised cloud complex, with mass between $2000\mathrm{M}_{\odot}$ and $20000\mathrm{M}_{\odot}$. Using Larson's scaling relation (Larson, 1981), one can show that such clouds would have a velocity dispersion in the range $1.2\,\mathrm{km\,s^{-1}}$ to $2.0\,\mathrm{km\,s^{-1}}$. The clouds are therefore given initial bulk velocities of

$$(v_{\mathrm{x}}, v_{\mathrm{y}}, v_{\mathrm{z}}) = (\mp v_{\mathrm{o}}, 0, 0), \tag{5.1}$$

with $v_0 = 1.2, 1.4, 1.6, 1.8$ and $2.0\,\mathrm{km\,s^{-1}}$. The Mach Numbers of the accretion shocks bounding the shock-compressed layer are of order 6 to 10, giving compression factors in the range 36 to 100.

The clouds initially have mass $M_{\mathrm{o}} = 500\,\mathrm{M}_{\odot}$, radius $R_{\mathrm{o}} = 2\,\mathrm{pc}$ and uniform density $\rho_{\mathrm{o}} = 1.01 \times 10^{-21}\,\mathrm{g\,cm^{-3}}$; hence the clouds have a freefall time of $t_{\mathrm{o}} = 2.1\,\mathrm{Myr}$. The cloud centres are initially at

$$(x, y, z) = (\pm 2.02, 0, 0)\,\mathrm{pc}, \tag{5.2}$$

such that they are almost touching; this ensures that the clouds do not have time to collapse before the collision begins. The fraction of hydrogen, by mass, is $X = 0.70$, and the hydrogen is assumed to be molecular, so the initial molecular hydrogen number-density is $n_{\mathrm{H_2}} = 2.1 \times 10^{2}\,\mathrm{H_2\,cm^{-3}}$. This gas is initially isothermal at $T_{\mathrm{o}} = 10\mathrm{K}$, and therefore has an isothermal sound speed $a_{\mathrm{o}} = 0.19\,\mathrm{km\,s^{-1}}$.

For each velocity we perform ten simulations. Of these ten simulations, five are performed with clouds that initially have zero internal velocity dispersion (Set 1),

and five are performed with clouds that initially have a very low-amplitude internal velocity field (Set 2). The first set (Set 1) of simulations have zero internal velocity dispersion and hence fragmentation is seeded by very small residual fluctuations in the particle density. The ratio of thermal to gravitational energy in an individual cloud is $\alpha_{\rm THERM} = 0.083 < 0.5$, so the pre-collision clouds are again not virialised. The second set of simulations (Set 2) have the same particle distribution as those of Set 1. However, in this case we add a velocity field with a power-spectrum $P_{\rm k} \propto k^{-4}$ and a velocity dispersion $\sigma_{\rm TURB} = 0.066\,{\rm km\,s^{-1}}$. This corresponds to a Mach Number $M_{\rm TURB} = 0.35$ and a turbulent to gravitational energy ratio of $\alpha_{\rm TURB} = 0.010$; hence the pre-collision clouds are again not virialised, $\alpha_{\rm THERM} + \alpha_{\rm TURB} = 0.093 < 0.5$.

5.1.2 Numerical method

The simulations are performed with the Smoothed Particle Hydrodynamics code GANDALF (see Sec. 3.2). The ∇h formulation of the evolution equations is invoked, and they are solved with a second order leapfrog integrator. Artificial viscosity is treated using the method of Monaghan (1997), with parameters $\alpha = 1$ and $\beta = 2$. A barotropic equation of state (see Sec. 3.4.2) is used with $T_0 = 10K$ and $\rho_{\rm CRIT} = 10^{-14}\,{\rm g\,cm^{-3}}$. Sinks are introduced and evolved using the standard procedure described in Hubber et al. (2013), with $\rho_{\rm SINK} = 10^{-12}\,{\rm g\,cm^{-3}}$; hence condensations which are converted into sinks are already well into their Kelvin-Helmholtz contraction phase, and their properties are essentially independent of $\rho_{\rm SINK}$.

This part of the study examines the stellar population that forms due to a cloud-cloud collision that has no feedback. We therefore terminate the simulations once 10% of the total mass has been converted into protostars, on the assumption that feedback would be becoming important at this stage and might begin to disrupt the star formation process. At this resolution it is also not practical to follow the simulations beyond this point. Feedback is added to these simulations in chapter 8 where we reduce the resolution (increase $m_{\rm SPH}$) and introduce sinks at a lower density threshold (lower $\rho_{\rm SINK}$).

All simulations are performed with $N_{\rm TOT} \simeq 10^6$ SPH particles, therefore each particle has mass $m_{\rm SPH} \simeq 0.001\,{\rm M_\odot}$. The resolution-parameter is set to $\eta = 1.2$, so that a SPH particle typically has ~ 57 neighbours, hence the mass resolution is $\sim 0.1\,{\rm M_\odot}$ (i.e. just above the hydrogen-burning limit). The particles are laid down in a glass as described in Sec. 3.4.1.

5.2 RESULTS

5.2.1 FRAGMENTATION OF THE LAYER

As the two clouds come into contact, a shock-compressed gas layer forms on either side of the x=0 plane, an example of which is shown in Fig. 5.1. Initially the mass and radius of this layer increases due to the increasing size of the collision area. However, the rate at which the radius of the layer grows decreases as the simulation progresses; this is due to the lateral collapse of the cloud, i.e collapse toward the x-axis. The amount of mass in the layer continues to grow throughout the simulation, and growth is at a maximum when the cloud centres are coincident. Once the layer becomes sufficiently massive, it fragments into a network of filaments. The form these filaments take is critically dependent on the speed at which the clouds collide.

We identify two critical times in the fragmentation process, t_{*1} and $t_{10\%}$. t_{*1} is the time at which the first protostar forms, and $t_{10\%}$ is the time at which the total mass first exceeds $100\,M_{\odot}$, in other words 10% of the mass has been converted into protostars. Fig. 5.2 shows the filamentary structure that has developed by the time the first protostar forms at t_{*1}, for simulations with different collision velocities, $v_{\circ}$.

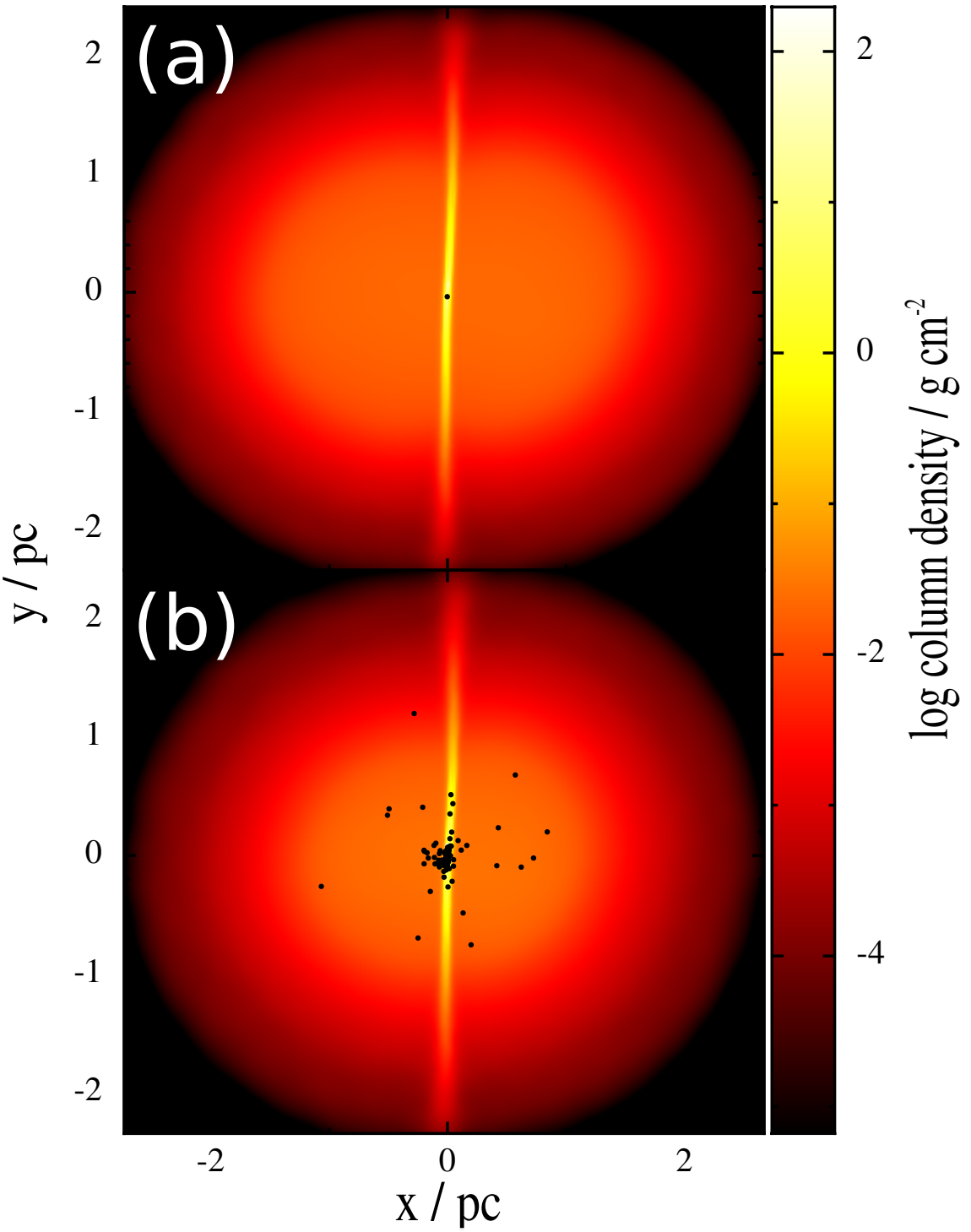

Figure 5.1. False-colour image of one of the simulations with $v_{\circ} = 2.0\,\mathrm{km\,s^{-1}}$, at time (a) $t_{\star 1} = 1.14\,\mathrm{Myr}$, (b) $t_{10\%} = 1.28\,\mathrm{Myr}$. Colour represents $\log_{10}\{\Sigma/\mathrm{g\,cm^{-2}}\}$, where Σ is column-density projected on the (x, y)-plane.

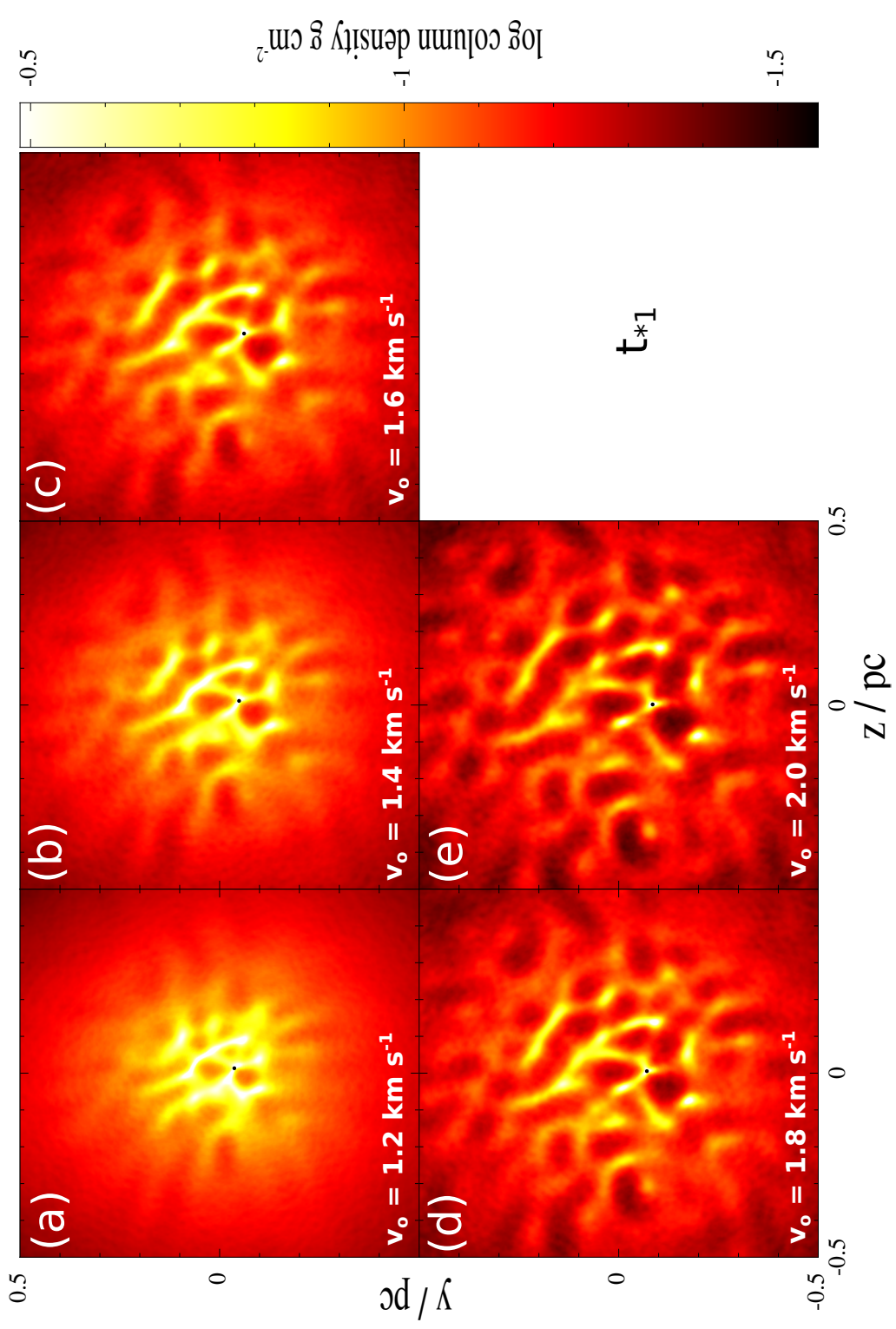

Figure 5.2. False-colour column density maps of fragmenting layers at the moment the first protostar forms, $t_{\star 1}$, from simulations using the same initial clouds (one of the ones that start with weak density and velocity perturbations) but different bulk velocities, $v_\circ$. (a) $v_\circ = 1.2\,\mathrm{km\,s^{-1}}$, $t_{\star 1} = 1.33\,\mathrm{Myr}$. (b) $v_\circ = 1.4\,\mathrm{km\,s^{-1}}$, $t_{\star 1} = 1.28\,\mathrm{Myr}$. (c) $v_\circ = 1.6\,\mathrm{km\,s^{-1}}$, $t_{\star 1} = 1.23\,\mathrm{Myr}$. (d) $v_\circ = 1.8\,\mathrm{km\,s^{-1}}$, $t_{\star 1} = 1.19\,\mathrm{Myr}$. (e) $v_\circ = 2.0\,\mathrm{km\,s^{-1}}$, $t_{\star 1} = 1.14\,\mathrm{Myr}$. Colour represents $\log_{10}\{\Sigma/\mathrm{g\,cm^{-2}}\}$, where Σ is column-density projected on the (y, z)-plane, i.e. looking along the direction of the collision. The first protostar is represented by a black dot.

In all panels the same initial cloud has been used, in this case the cloud has uniform density, and a weak turbulent velocity field. The turbulent velocity field and the cloud orientation are the same in all five simulations, and consequently the configurations of the filaments at t_{*1} are broadly similar. It is important to note that the form the filamentary structure takes is almost independent of the way the initial perturbations are seeded.

The extent of the filamentary structure at t_{*1} is dependent on the velocity, $v_{\rm o}$, at which the clouds collide. Low velocity collisions, $v_{\rm o} < 1.6\,{\rm km\,s^{-1}}$, produce a much more centrally concentrated network of filaments. This is because the surface density of the layer builds up more slowly, and the filamentary structure takes longer to develop. Hence, by the time the first protostar forms the lateral contraction of the layer has progressed further, and the extent of the filamentary network is smaller.

5.2.2 Formation of the first protostar

The time at which the first protostar forms is related to the time at which the layer begins to fragment. This fragmentation process was investigated by Whitworth et al. (1994), who show that a shock-compressed layer created by two semi-infinite anti-parallel flows with a density $\rho_{\rm o}$, and velocity $v_{\rm o}$, fragments at time,

$$t_{\rm CRIT} \simeq \left(\frac{a_{\rm s}}{2^{3/2} G \rho_{\rm o} v_{\rm o}} \right)^{1/2} . \tag{5.3}$$

Here $a_{\rm s}$ is the effective isothermal sound speed in the shocked gas, and 'semi-infinite' means that, if the discontinuity between the flows is the $x = 0$ plane, the gas has infinite extent in the y- and z-directions. However, the layer created as a result of a cloud-cloud collision has a finite extent in the y- and z- directions and therefore contracts towards the x-axis on a timescale,

$$t_{\rm FF} \simeq \left(\frac{3\pi}{32 G \rho_{\rm o}} \right)^{1/2} . \tag{5.4}$$

As a result of this contraction, the condensation of the first protostar is accelerated.

We suggest that the time at which the first protostar forms might be approximated

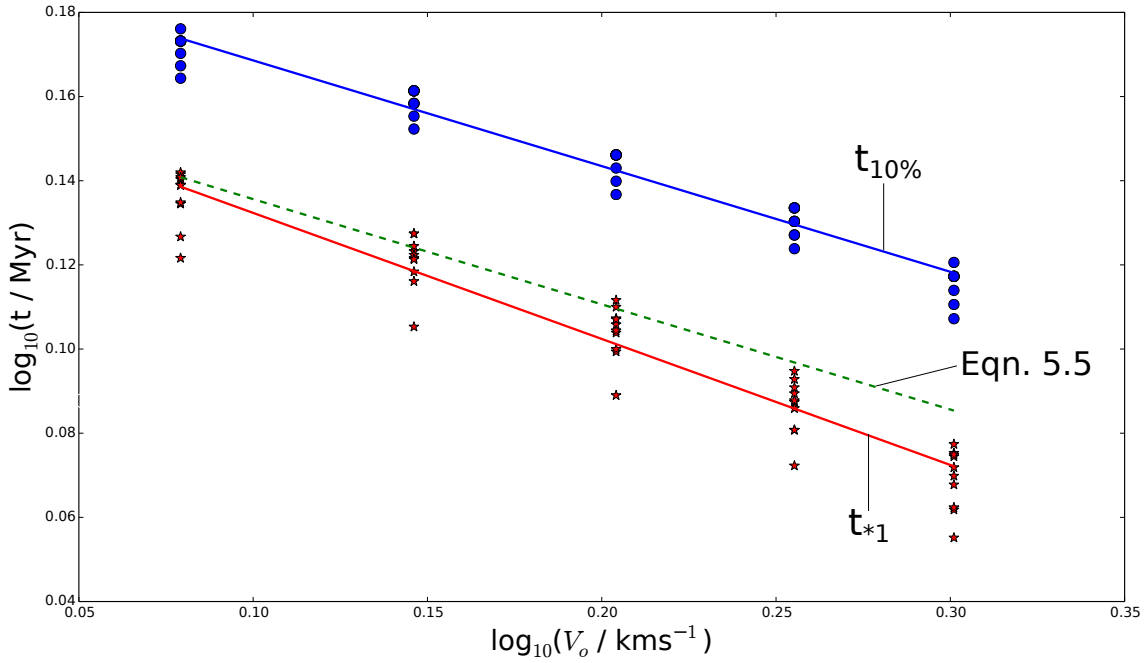

Figure 5.3. The time of formation of the first protostar, t_{*1} (red solid circles, red best-fit line), and the time at which 10% of the total mass has been converted into protostars, $t_{10\%}$ (blue stars, blue best-fit line), plotted against the cloud velocity, $v_{\rm o}$. The green dashed line is the value of t_{*1} predicted by Eqn. (5.5).

by the logarithmic mean of $t_{\rm CRIT}$ and $t_{\rm FF}$, i.e.

$$t_{*1} \simeq \left(t_{\rm CRIT} t_{\rm FF}\right)^{1/2} \simeq \frac{1}{2(G_{\rm o})^{1/2}} \left(\frac{3\pi a_{\rm s}}{2^{5/2} v_{\rm o}}\right)^{1/4} \tag{5.5}$$

Fig. 5.3 shows the values of t_{*1} and $t_{10\%}$ from all of the simulations we performed, as well as the prediction of Eqn. 5.5.

5.2.3 RECONFIGURATION OF THE FILAMENTS

The filamentary structure becomes more defined as the simulation approaches $t_{10\%}$. This can be seen by comparing Fig. 5.2 and Fig. 5.4 which are false colour images of the fragmenting layers at t_{*1} and $t_{10\%}$.

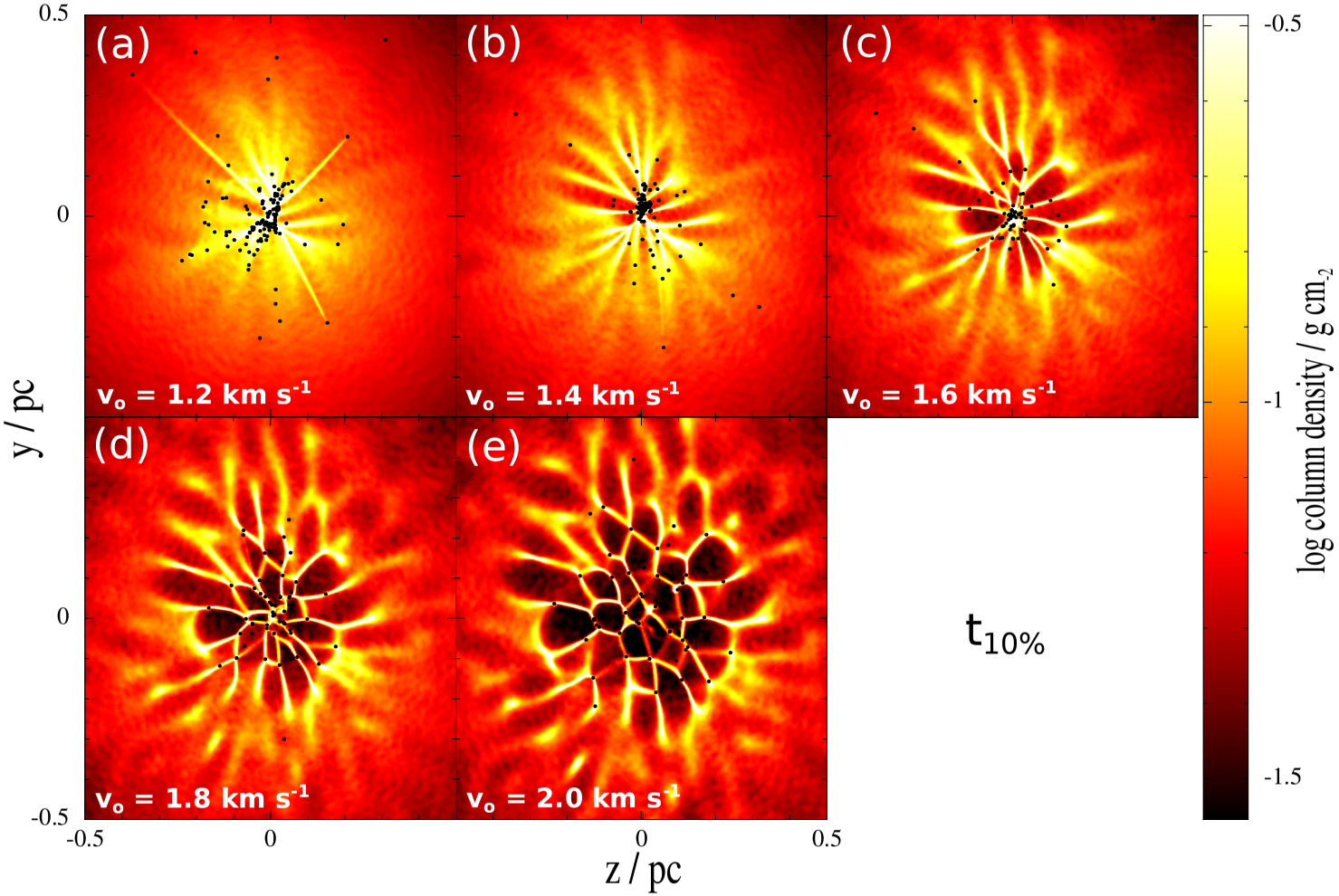

Figure 5.4. False-colour column-density maps of fragmenting layers at the moment, $t_{10\%}$, when 10% of the mass has been converted into protostars, from the same simulations presented in Fig. 5.3. (a) $v_{\rm o} = 1.2\,{\rm km\,s^{-1}}$, $t_{10\%} = 1.47\,{\rm Myr}$. (b) $v_{\rm o} = 1.4\,{\rm km\,s^{-1}}$, $t_{10\%} = 1.42\,{\rm Myr}$. (c) $v_{\rm o} = 1.6\,{\rm km\,s^{-1}}$, $t_{10\%} = 1.37\,{\rm Myr}$. (d) $v_{\rm o} = 1.8\,{\rm km\,s^{-1}}$, $t_{10\%} = 1.33\,{\rm Myr}$. (e) $v_{\rm o} = 2.0\,{\rm km\,s^{-1}}$, $t_{10\%} = 1.28\,{\rm Myr}$. Colour represents $\log_{10}\{\Sigma/{\rm g\,cm^{-2}}\}$, where Σ is column-density projected on the (y, z)-plane, i.e. looking along the direction of the collision. The black dots represent the protostars.

The shock compressed layer has an increased surface density close to the x-axis and this causes the layer to undergo non-homologous lateral contraction. As a result the inner parts of the layer converge on shorter timescales than the outer parts, stretching pre-existing filaments into predominately radial orientations.

The lateral contraction of the layer has a greater effect in low velocity collisions. Filaments in these layers are stretched radially producing a system of spokes that feed material into a central hub where a large reservoir of gas accumulates (see the top row of Fig. 5.4), producing a hub and spoke system similar to the one found by Peretto et al. (2014). Any stars that form in these filaments are diverging from one another due to the tidal stretching of the filament they formed in. Stars that form in this way tend to have low masses and do not interact until they reach the central hub, where they interact violently with one another. Many stars are ejected as a result of these interactions, but a few settle in the centre, where they are able to grow by competitive accretion. The final population of protostars formed from a low velocity collision tends to be made up of a large number of low mass protostars with a few high mass protostars.

Two clouds colliding at high collision velocity, $v_{\circ} \geq 1.6\,\mathrm{kms}^{-1}$, produce a large network of criss-crossing filaments with nodes wherever two or more filaments intersect (see the frames on the bottom row of Fig. 5.4). The filaments that feed each node are small, and are therefore only able to provide a small amount of gas from which prestellar cores can form. As a result each node is only able to form a small sub-cluster of protostars, and each of these sub-clusters will typically contain one moderately massive protostar and a few less massive ones.

5.2.4 THE RATE OF STAR FORMATION

In my simulations the duration of star formation

$$\delta t_{\mathrm{SF}} = t_{10\%} - t_{*1} \simeq 0.14 \pm 0.01\,\mathrm{Myr}, \tag{5.6}$$

is approximately independent of collision velocity, $v_{\circ}$. Thus, the overall star formation rate in the layer is also approximately independent of $v_{\circ}$,

$$\dot{M}_{*} = \frac{100\,\mathrm{M}_{\odot}}{\delta t_{\mathrm{SF}}} \simeq 700\,\mathrm{M}_{\odot}\,\mathrm{Myr}^{-1}. \tag{5.7}$$

At lower collision velocity, star formation starts later, and there is less mass in the shock-compressed layer when it does. This is compensated for by the fact that the layer has had more time to contract laterally and so the star formation rate is similar in all simulations.

5.2.5 The mass function of protostars

For the remainder of the chapter we merge the data from both the Set 1 and Set 2 simulations. We do this because we find the protostellar population develops in the same way regardless of how we seed the initial perturbations.

The stellar population is affected by the velocity at which the clouds collide, $v_{\circ}$. Increasing the velocity raises the median protostellar mass, and decreases both the maximum protostellar mass and the spread of protostellar masses. Low collision velocities promote the formation of a large hub at the centre of the layer. Protostars fall into this hub and partake in competitive accretion, consequently a small number of protostars grow to very large masses, and a large number of protostars are ejected dynamically, producing a diaspora of predominately low-mass protostars. Collisions at high velocity produce a number of different nodes spawning protostars independently of one another. Each node spawns one moderately massive protostar and a few smaller ones, resulting in a large fraction of the protostars having similar mass. There are few dynamical ejections and as a result most protostars are still close to the location where they formed when the simulations are terminated.

We illustrate these trends in Fig. 5.5 by plotting the mass ranges, as a function of collision velocity. The green lines represent the complete ranges of masses at each velocity. The red lines represent the range between the 10th and 90th centiles; in other words, by number, 10% of the stars fall below this range, and 10% fall above it. Similarly the blue lines represent the range between the 25th and 75th centiles, also known as the interquartile range.

The maximum protostellar mass, shown by the upper green line, decreases as $v_{\circ}$ is increased. An increase in $v_{\circ}$ leads to a reduction in the size and mass of the central hub, and eventually, for sufficiently high $\mathrm{v_O}$, it disappears. As a consequence the amount of material available for the competitive accretion process is reduced. This not only lowers the mass of the most massive protostar but also the number of small protostars, which has the effect of increasing the median protostellar mass.

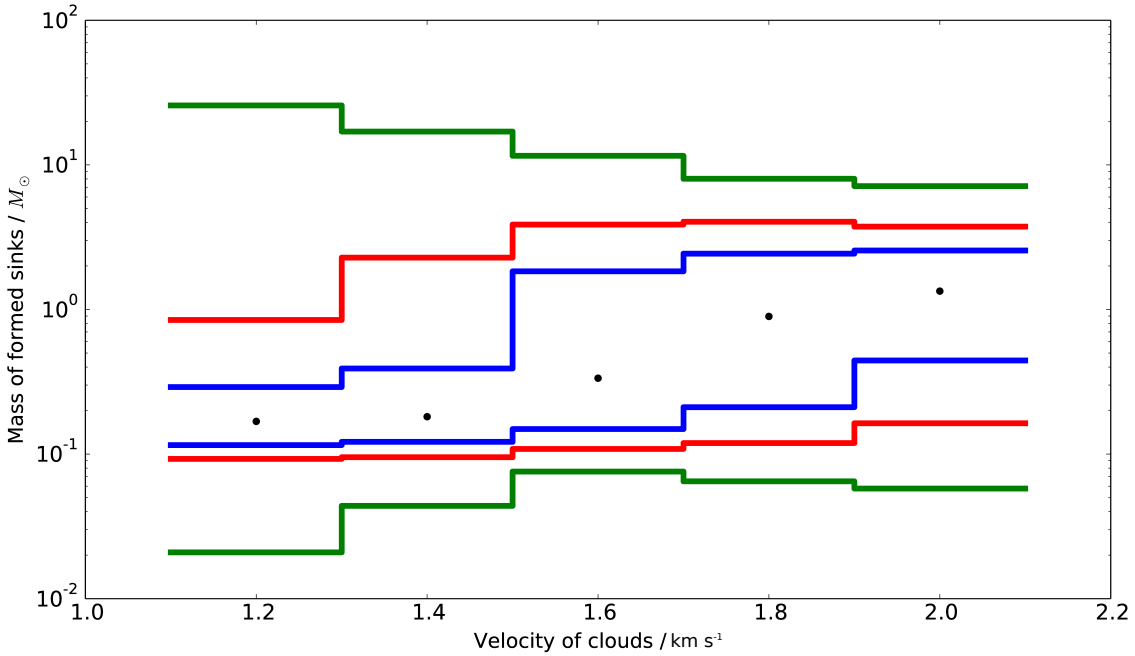

Figure 5.5. Protostellar mass ranges. For each collision velocity, $v_\circ$, we combine the data from all ten realisations. The green shading gives the full range of protostellar masses, the red shading gives the range between the 10^{th} and 90^{th} centiles, the blue shading gives the range between the 25^{th} and 75^{th} centiles (the interquartile range), and the filled circles give the median mass.

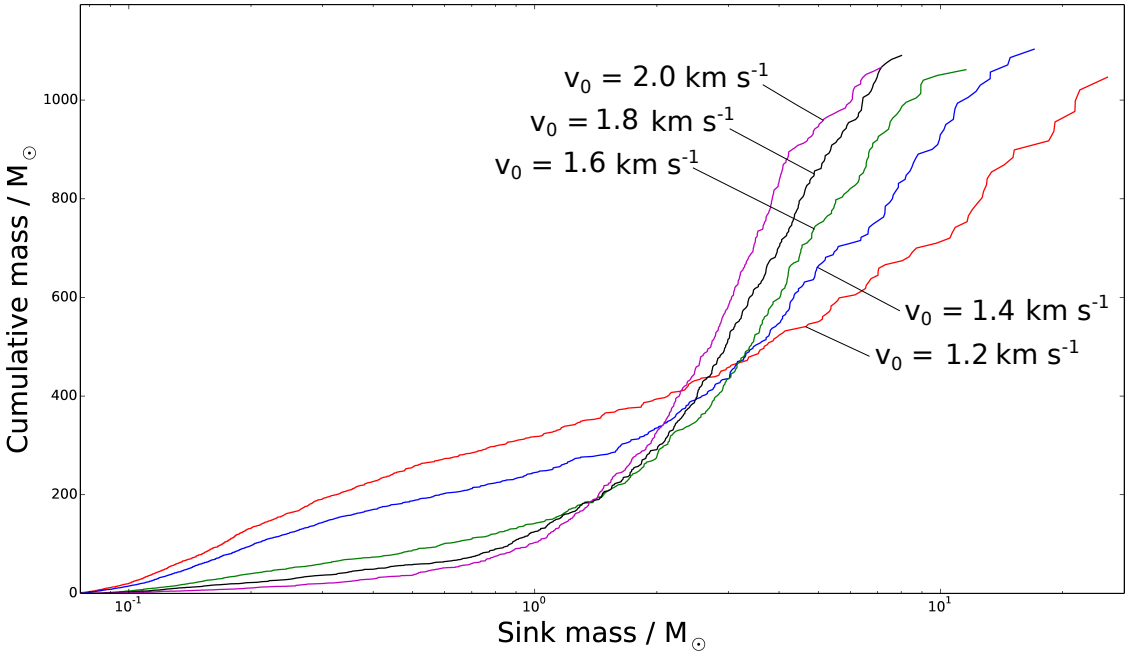

Figure 5.6. The cumulative mass of protostars at $t_{10\%}$, from all 50 simulations (10 at each v_o),as a function of protostellar mass. Red full curve: $v_o = 1.2\,\mathrm{km\,s^{-1}}$. blue dashed curve: $v_o = 1.4\,\mathrm{km\,s^{-1}}$. green dotted curve: $v_o = 1.6\,\mathrm{km\,s^{-1}}$. black cross-dashed curve: $v_o = 1.8\,\mathrm{km\,s^{-1}}$. purple dot-dashed curve: $v_o = 2.0\,\mathrm{km\,s^{-1}}$.

We cannot draw any conclusions from the minimum protostellar mass, illustrated by the lower green line. The smallest possible protostellar mass is set by the procedure for sink creation, i.e. $\sim N_{\mathrm{NEIB}} \sim 0.05\,\mathrm{M}_\odot$. Protostars that form right at the end of the simulation tend to have masses of this order because they have not had time to accrete additional mass. For this reason we cannot draw any meaningful conclusions from this quantity.

The transition from a hub and spoke system to a spider web system occurs between $v_o = 1.4\,\mathrm{km\,s^{-1}}$ and $v_o = 1.6\,\mathrm{km\,s^{-1}}$. We can see the effect of this in the stellar population, as illustrated in 5.5 where we see a sharp transition in this velocity range, this is most noticeable in the blue lines.

Fig. 5.6 plots cumulative mass against protostellar mass for each of the five collision velocities. The graph illustrates that the amount of mass in low-mass protostars increases dramatically with decreasing collision velocity, v_o. Again this is most dramatic between $v_o = 1.4\,\mathrm{km\,s^{-1}}$ and $v_o = 1.6\,\mathrm{km\,s^{-1}}$. It also shows how the two most massive protostars become more massive with decreasing v_o .

Table 5.1. Parameters of the mass functions of protostars formed with different collision velocities. Column 1 gives the collision velocity, v_o, column 2 gives the mean number of protostars, $\bar{\mathcal{N}_\star}$, formed from one collision (and totalling $100\,\mathrm{M}_\odot$), and columns 3 through 6 give, respectively, the mean, $\mu_{\log_{10}}$, standard deviation, $\sigma_{\log_{10}}$, skew, $\gamma_{\log_{10}}$, and kurtosis, $\kappa_{\log_{10}}$, of the protostellar log-masses, $\log_{10}\!\left(M_\star/\mathrm{M}_\odot\right)$.

v_{10}	$\bar{\mathcal{N}_\star}$	$\mu_{\log_{10}}$	$\sigma_{\log_{10}}$	$\gamma_{\log_{10}}$	$\kappa_{\log_{10}}$
$1.2\,\mathrm{km\,s^{-1}}$	198	-0.65	+0.45	+1.92	+4.08
$1.4\,\mathrm{km\,s^{-1}}$	163	-0.56	+0.53	+1.41	+1.12
$1.6\,\mathrm{km\,s^{-1}}$	108	-0.29	+0.60	+0.43	-1.21
$1.8\,\mathrm{km\,s^{-1}}$	88	-0.13	+0.58	-0.11	-1.33
$2.0\,\mathrm{km\,s^{-1}}$	86	-0.01	+0.50	-0.58	-0.72

In no case is the distribution log-normal. Table 5.1 gives the mean, μ_{logM}, standard deviation, σ_{logM}, skew, γ_{logM}, and kurtosis, κ_{logM}, of $\log_{10}(\mathrm{M}_*/\mathrm{M}_\odot)$, for different v_o. As v_o increases, μ_{logM} increases monotonically, i.e. the mean stellar mass increases; σ_{logM} increases and then decreases, but does not vary by much; γ_{logM} decreases monotonically, indicating that the mass function is very asymmetric at low v_o (due to the large number of very low-mass protostars), but becomes increasing symmetric at larger v_o; the variation of the kurtosis indicates that the mass function at low v_o is much more sharply peaked than at high v_o.

On large scales observations suggest that the Initial Mass Function (IMF) does not vary much. However, there may be significant variations on small scales, over and above those that arise purely from sampling statistics. If this is the case then the universal IMF is made up from an average over a representative ensemble of such regions. If we were to observe a single cloud-cloud collision at an early stage of its evolution (i.e before it is dispersed and/or contaminated with other stars) we may may see a stellar population such as the one we see in our simulations.

5.2.6 ACCRETION RATES

We find that as the velocity of the collision is increased, the maximum protostellar mass decreases, and the number of low-mass protostars decreases. This is shown in Fig. 5.7, which plots the final protostellar masses, M_*, at $t_{10\%}$, against the their time of formation t_{FORM}.

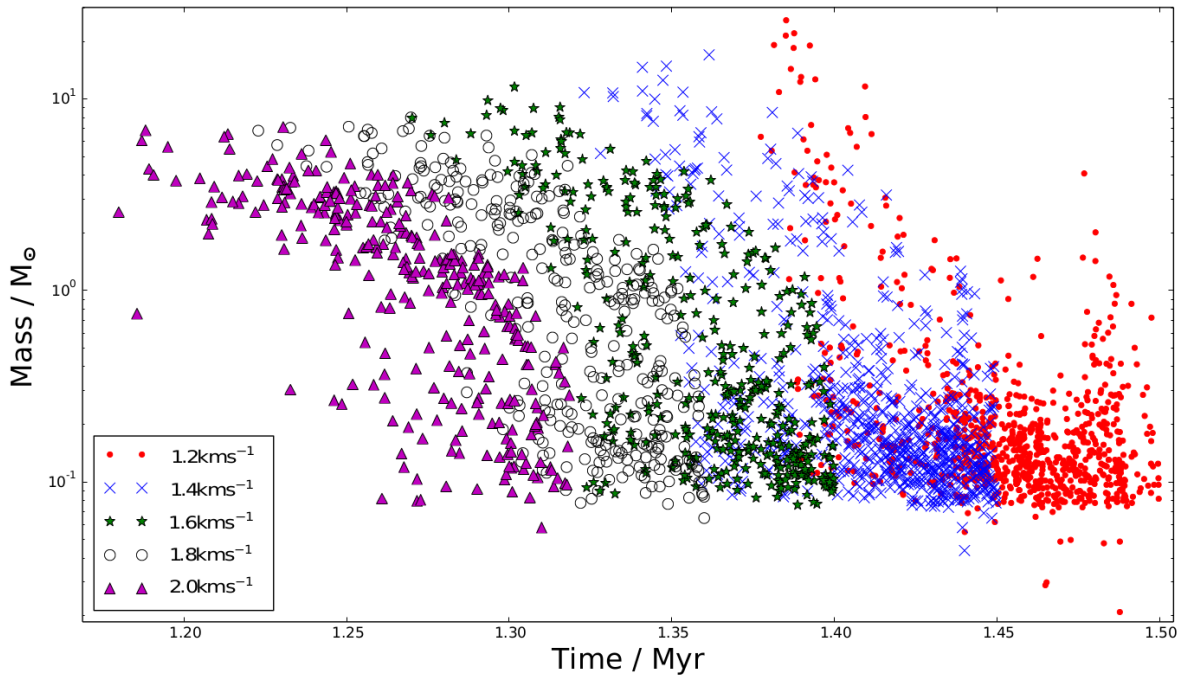

Figure 5.7. The final mass of each protostar, $M_\star$, at $t_{10\%}$ (the end of the simulation) plotted against its time of formation, $t_{\rm FORM}$, i.e. the time at which the corresponding sink particle is created. Red dots, $v_{\rm o} = 1.2\,{\rm km\,s^{-1}}$; blue crosses, $v_{\rm o} = 1.4\,{\rm km\,s^{-1}}$; green stars, $v_{\rm o} = 1.6\,{\rm km\,s^{-1}}$; black open circles, $v_{\rm o} = 1.8\,{\rm km\,s^{-1}}$; purple triangles, $v_{\rm o} = 2.0\,{\rm km\,s^{-1}}$.

Fig. 5.8 shows protostellar accretion rates, $\dot{M}_*$, plotted against protostellar mass, M_*, both evaluated at the end of the simulation, $t_{10\%}$. The final masses of protostars from a low velocity collision , $v_\circ < 1.6\,\mathrm{km\,s^{-1}}$, tend to be more concentrated at low masses, 0.08 to 3 $M_\odot$, and have a wide range of accretion rates. The exception to this is the most massive protostars which are still growing very quickly. The protostars produced by fast collisions , $v_\circ > 1.6\,\mathrm{km\,s^{-1}}$, tend to have final masses and accretion rates that are high, and are clustered around the same region.

5.3 SUMMARY

We have explored the evolution that results from the collision of two quiescent and approximately uniform-density clouds. These clouds have mass $M_\circ = 500\mathrm{M}_\odot$, radius $R_\circ = 2\,\mathrm{pc}$ and collide with relative speeds between $2.4\,\mathrm{km\,s^{-1}}$ and $4.0\,\mathrm{km\,s^{-1}}$. The results are summarised below:

- In all cases the colliding clouds produce a shock-compresed layer, which fragments into filaments.

- At lower relative velocities, it takes longer before fragmentation becomes non-linear and delivers protostars.

- At low relative velocities the filaments are predominately radial due to the effects of lateral collapse, which drags and stretches them toward the collision axis. Protostars condense out of filaments and they then fall along those filaments towards the centre, along with residual gas, so that a single massive cluster forms there. In the central region competitive accretion leads to the formation of a few very massive protostars, and the ejection of a large number of low mass protostars. The distribution of filaments around the single massive cluster can be described as a hub and spoke system.

- At higher relative velocities , there is less time for lateral collapse of the layer, and so the filaments form a network like a spiders web, with many independent star-forming nodes collecting at the intersections of the filaments. The filaments feeding these nodes are relatively short and therefore deliver only a small amount of material from which stars can form. As a result, nodes are only able to spawn a small number of protostars. These typically consist of one of moderate mass and a few of lower mass. Dynamical ejections are rare because there are few protostars in each node.

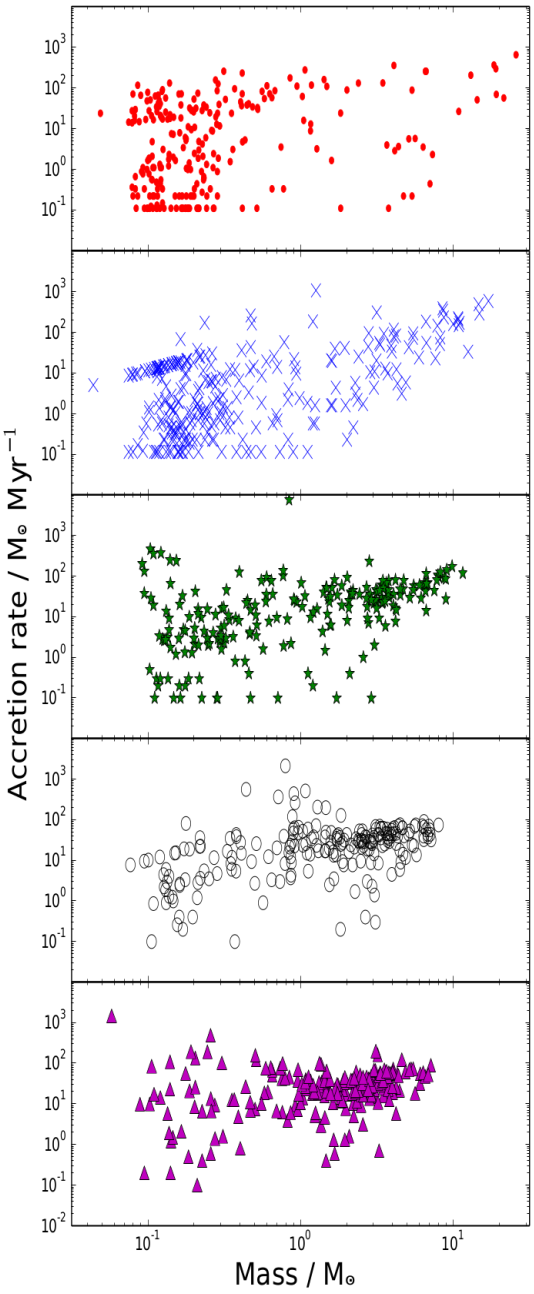

Figure 5.8. Log-log plot of the rate of accretion, $\dot{M}_\star$, against the protostellar mass, $M_\star$, both evaluated at the end of the simulation, $t_{10\%}$. Red dots, $v_\circ = 1.2\,\mathrm{km\,s^{-1}}$; blue crosses, $v_\circ = 1.4\,\mathrm{km\,s^{-1}}$; green stars, $v_\circ = 1.6\,\mathrm{km\,s^{-1}}$; black open circles, $v_\circ = 1.8\,\mathrm{km\,s^{-1}}$; purple triangles, $v_\circ = 2.0\,\mathrm{km\,s^{-1}}$. Note that the lowest accretion rates are quantised at values $0.1\,\mathrm{M_\odot\,Myr^{-1}}$, $0.2\,\mathrm{M_\odot\,Myr^{-1}}$, $0.3\,\mathrm{M_\odot\,Myr^{-1}}$, etc., corresponding to sinks accreting one, two, three, etc. SPH particles (hence $10^{-3}\,\mathrm{M_\odot}$, $2\times10^{-3}\,\mathrm{M_\odot}$ $3\times10^{-3}\,\mathrm{M_\odot}$, etc.), during the 0.01 Myr interval between the last two outputs. Similarly some accretion rates fall on the line $\dot{M}_\star = M_\star/0.01\,\mathrm{Myr}$, corresponding to sinks formed during the 0.01 Myr interval between the last two outputs.

- As the collision velocity is increased, the mean protostellar mass increases, but the range of protostellar masses goes down, so the maximum mass actually decreases and the minimum mass increases; there are many fewer low-mass protostars.

Chapter 6
Cloud-cloud collisions : Effects of finite closest approach and fractal density

In chapter 5 we simulate the collision of two uniform density molecular clouds. We show that for the stellar populations that form, both their mass distribution and their distribution in space are highly dependent on the velocity at which the clouds collide, and that very high mass stars are only able to form following low velocity collisions. However, we would not expect two uniform density clouds to collide head on. It is much more likely that the collision will involve two clouds with pre-existing density structure, and that the collision will be at finite closest approach (Dobbs et al., 2015), although we only have a few observations of such regions (Furukawa et al., 2009; Ohama et al., 2010; Torii et al., 2011; Duarte-Cabral et al., 2011) and it is therefore dificult to deturine the contitions of the clouds prior to collision. In order to address this more realistic scenario, we repeat the simulations of chapter 5 and vary (i) the closest approach and (ii) the initial density structure, and explore what effect this has on the structures and stellar populations that form.

6.1 closest approach

The closest approach, b, is a measure of the collision offset, i.e. the separation of the centres of the clouds, excluding the separation along the axis of collision. If b = 0 the clouds will collide head on, as is the case in Chapter 5. However, approximately head on collisions are expected to be rare (see Sec. 2.2.1) and would only make a small contribution to the Initial Mass Function (IMF). For cloud-cloud

collisions to make a significant contribution to the IMF, there would have to be a large number of collisions with b $>$ 0. To understand what contribution these collisions make we repeat the simulations of Chapter 5, and explore how the stellar populations change as we increase the closest approach.

6.1.1 SIMULATION SET UP

The simulations are set up as they were in Chapter 5, hence the clouds have mass $M_{\circ} = 500\,\mathrm{M}_{\odot}$, radius $R_{\circ} = 2\,\mathrm{pc}$ and uniform density $\rho_{\circ} = 1.01 \times 10^{-21}\,\mathrm{g\,cm^{-3}}$. The closest approach is introduced in the y direction, hence the cloud centres are located at,

$$(x, y, z) = (-2.02, 0, 0)\,\mathrm{pc}, \tag{6.1}$$

and,

$$(x, y, z) = (2.02, b, 0)\,\mathrm{pc}, \tag{6.2}$$

where b is either $R_0/8$ or $R_0/4$. For $R_0/8$, we perform a total of 30 simulations, comprising 5 re- alisations for each of the 6 collision velocities v_0 = 1.0, 1.2, 1.4, 1.6, 1.8 and 2.0 $\mathrm{km\,s^{-1}}$. For $R_0/4$, we perform a total of 35 simulations, comprising 5 re- alisations for each of the 7 collision velocities v_0 = 0.8, 1.0, 1.2, 1.4, 1.6, 1.8 and 2.0 $\mathrm{km\,s^{-1}}$. Unlike Chapter 5 we do not carry out ten realisations for each of the collision velocities, this is because we find only a small change in the results when the number of realisations is increased beyond 5, and it is therefore inefficient to continue beyond this point. Simulations are terminated once 10% of the total mass is in stars, as we do not include feedback. GANDALF is used to carry out the simulations and is configured in the same was as in Sec.5.1.2.

6.1.2 RESULTS

Increasing the closest approach has a notable effect on the shape of the shock compressed layer. It is not only diagonal in orientation but is also deformed at the edge, giving the layer the appearance of an integral sign, see Fig. 6.1. The lateral collapse of the clouds is not uniform and as a result a density gradient forms thoughtout the clouds with the centre being more dense. This difference in density becomes noticeable when the closest approach is increased because two opposite chords no longer have the same density. Therefore the cloud on the right dominates the upper part of

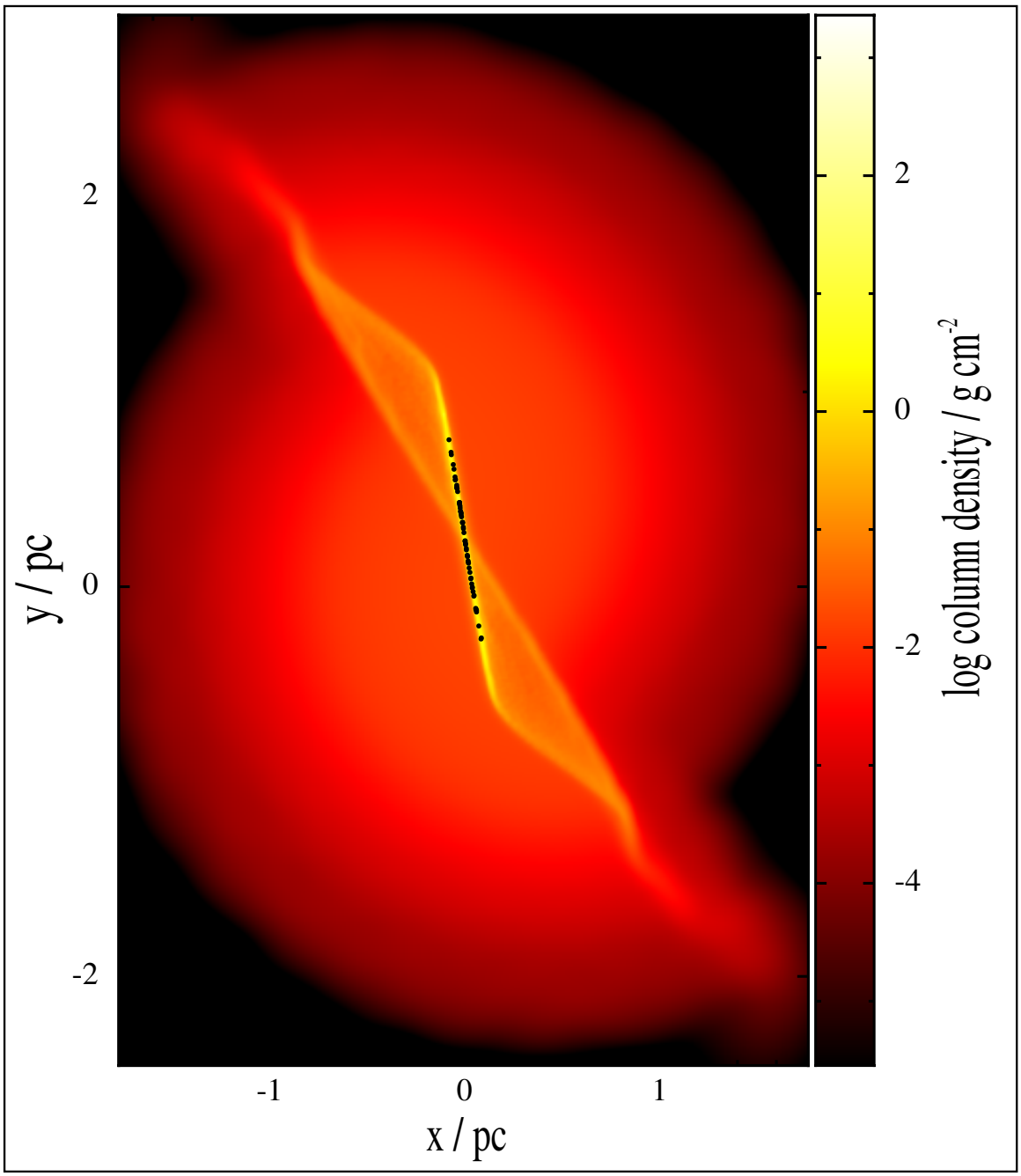

Figure 6.1. False-colour image of the colliding clouds, as seen looking across the collision axis at $t_{10\%}$ (i.e. when 10 percent of the mass has been converted into protostars). In this case the simulation has $v_o = 2.0\,\mathrm{km\,s^{-1}}$ and b = $R_0/4$. Colour represents $log_{10}\{\Sigma/\mathrm{g\,cm^{-2}}\}$, where Σ is column-density projected on the (x,y)-plane. The black dots are protostars.

the layer and the cloud on the left dominates the lower part. The edge of the layer is more susceptible to this effect and is therefore able to travel much further, giving the layer its characteristic shape.

In Chapter 5 we identify two filamentary structures, the hub and spoke, and the spider's web. We also identify a critical velocity, $v_{\rm CRIT} = 1.6\,{\rm km\,s^{-1}}$, at which the system switches from one to the other. This value is a measure of the relationship between the timescale of fragmentation and the timescale of lateral collapse. If the timescale of lateral collapse is comparable to that of fragmentation then the filaments are able to converge onto the centre and form a hub and spoke system, otherwise they form a spider's web system. Increasing the closest approach, decreases the rate of lateral collapse in the central region of the layer. By the central region we mean the region between the cloud centres, where the gas from each cloud is collapsing in opposing directions. This is not the case in collisions with b $= 0$ because the cloud centres are coincident and the gas collapses in the same direction. We illustrate this in Fig. 6.2, where we see that for $b > 0$ (B in the figure) the central region has collapse in opposing directions; whereas for $b = 0$ (A in the figure) the collapse from both clouds is in the same direction. The shear introduced because of this causes the rate of lateral collapse in the star forming region to decrease and as a result the critical velocity is also decreased. Therefore systems that were hub and spoke in chapter 5 may begin to develop spiderweb like features. When we look at the outputs of simulations with $R_0/8$ (Fig. 6.3) and $R_0/4$ (Fig. 6.4) we see that this is the case, and only at very low collision velocities do we see the hub and spoke systems appearing.

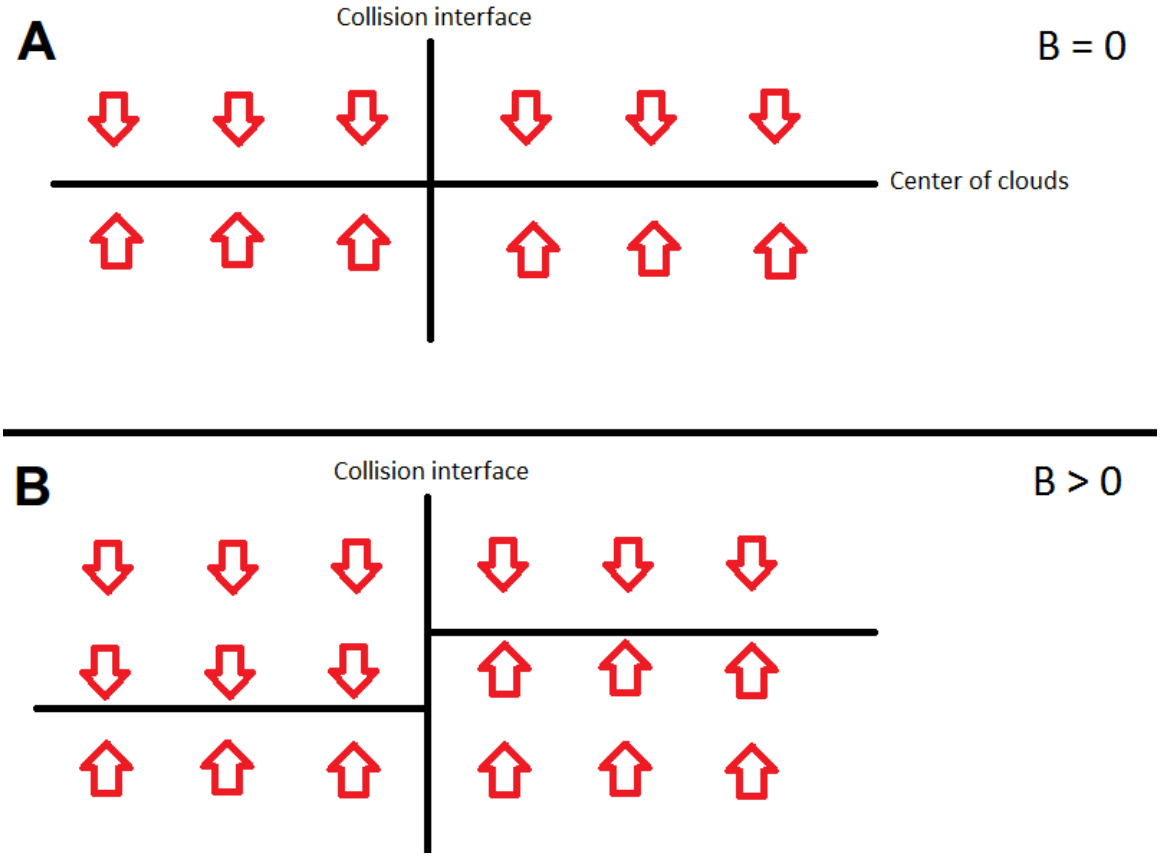

Figure 6.2. Diagram to illustrate the direction in which the gas will be collapsing in clouds that have b = 0 (A) and b > 0 (B). The diagrams show the view looking across the collision axis and the layer would be located along the collision interface. Red arrows indicate the direction of the vertical collapse in each of the cloud regions.

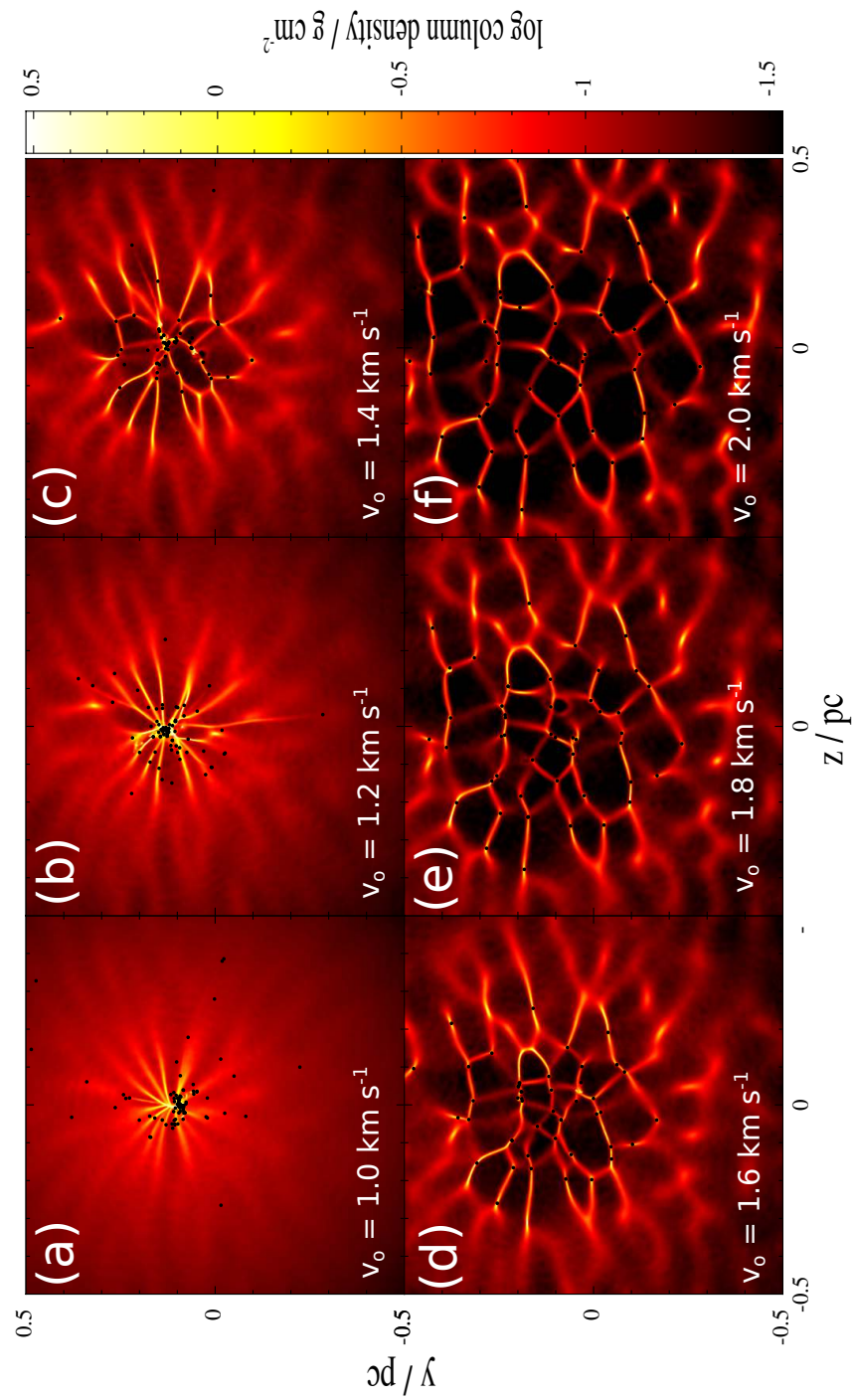

Figure 6.3. False-colour images at time $t_{10\%}$, for simulations involving uniform-density clouds colliding at impact parameter $b_\circ = 0.25\,\mathrm{pc}$ $(= R_\circ/8)$ and different collision velocities: (a) $(v_\circ, t_{10\%}) = (1.0\,\mathrm{km\,s^{-1}}, 1.53\,\mathrm{Myr})$; (b) $(1.2\,\mathrm{km\,s^{-1}}, 1.49\,\mathrm{Myr})$; (c) $(1.4\,\mathrm{km\,s^{-1}}, 1.42\,\mathrm{Myr})$; (d) $(1.6\,\mathrm{km\,s^{-1}}, 1.36\,\mathrm{Myr})$; (e) $(1.8\,\mathrm{km\,s^{-1}}, 1.30\,\mathrm{Myr})$; (f) $(2.0\,\mathrm{km\,s^{-1}}, 1.25\,\mathrm{Myr})$. Colour represents $\log_{10}\{\Sigma/\mathrm{g\,cm^{-2}}\}$, where Σ is column-density projected on the (y, z)-plane, i.e. looking along the collision axis. The black dots represent stars.

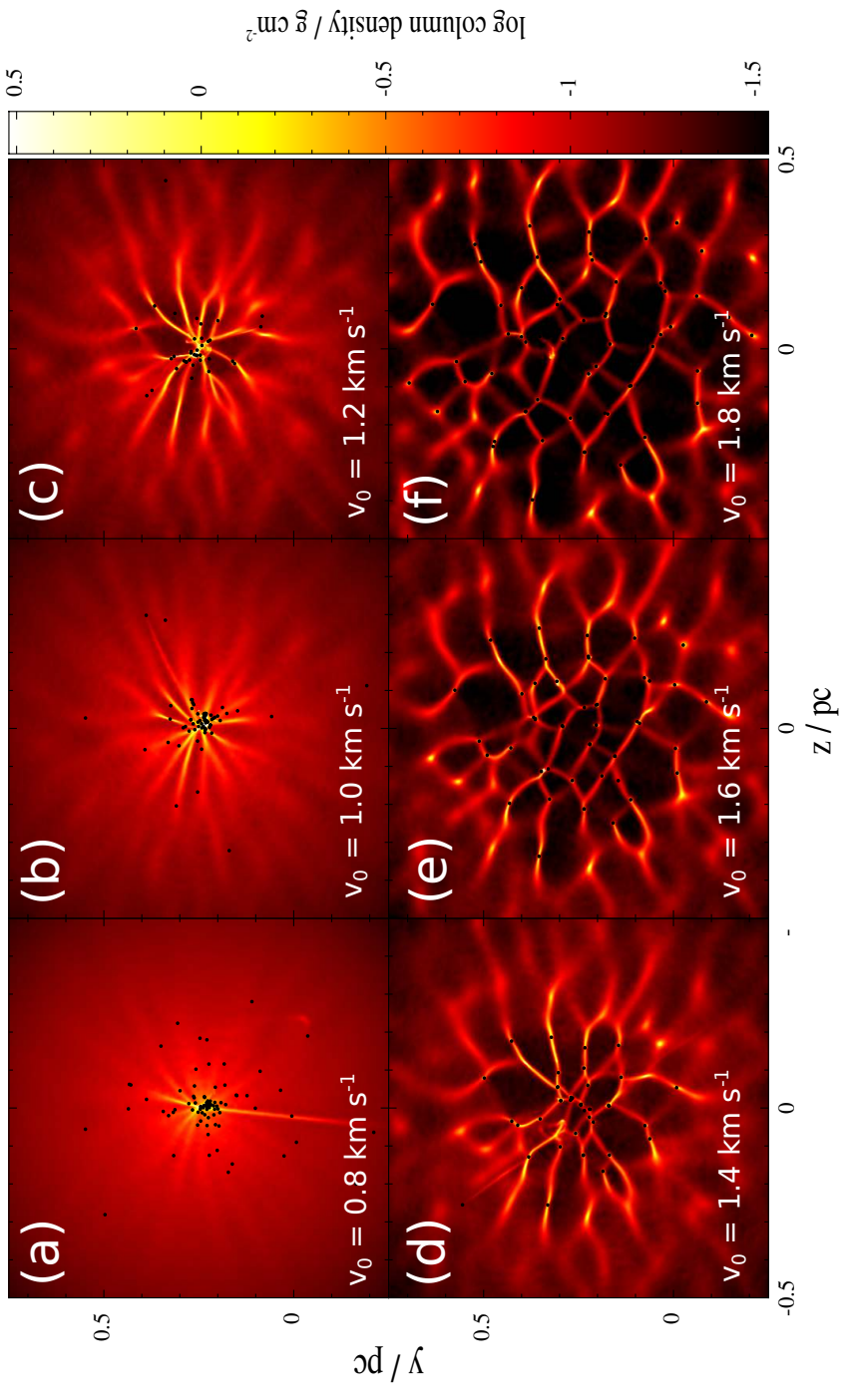

Figure 6.4. As Fig. 6.3, but with the larger impact parameter, $b_\circ = 0.50\,\mathrm{pc}$ ($= R_\circ/4$) and (a) $(v_\circ, t_{10\%}) = (0.8\,\mathrm{km\,s^{-1}}, 1.62\,\mathrm{Myr})$; (b) $(1.0\,\mathrm{km\,s^{-1}}, 1.55\,\mathrm{Myr})$; (c) $(1.2\,\mathrm{km\,s^{-1}}, 1.48\,\mathrm{Myr})$; (d) $(1.4\,\mathrm{km\,s^{-1}}, 1.41\,\mathrm{Myr})$; (e) $(1.6\,\mathrm{km\,s^{-1}}, 1.34\,\mathrm{Myr})$; (f) $(1.8\,\mathrm{km\,s^{-1}}, 1.28\,\mathrm{Myr})$.

We also see the reduction of the critical velocity in the median and interquartile ranges (shown in Fig. 6.5). In the low velocity cases there is a increase in the median, which now becomes consistent with a spider's web system. There is also a narrowing of the range of stellar masses, consistent with stars that form in isolated nodes rather than one big hub. At high velocities we see very little change in the median and only a small reduction in the range of masses. This suggests that as the velocity is increased beyond the critical velocity the system will tend toward a spider's web system, with a characteristic mass. These features once again present themselves in the cumulative mass plots of Fig. 6.6 where we see a reduction in the amount of mass in low mass protostars. The profiles at higher collision velocity also become more similar as the closest approach is increased.

6.2 FRACTAL DENSITY PROFILE

It is widely accepted that molecular clouds are non-uniform and that the underlying density structure plays an important role in star formation. In the simulations we have performed so far we have opted to use a uniform density structure so that we can disentangle the effects that are a result of the collision from those that are a result of the initial conditions. However, because density structure plays such an important role in star formation we explore how adding a fractal density profile to the initial conditions alters the stellar populations we obtain in chapter 5.

6.2.1 SIMULATION SET UP

The clouds in this simulation are given the same mass, $M_0 = 500\,\mathrm{M}_\odot$, as those in the previous simulations, but we increase the radius to $R = 4\,\mathrm{pc}$ in order to reduce the average density to $\rho_0 = 1.26^{-22}\,\mathrm{g\,cm^{-3}}$. This is done so that the densest regions of the cloud do not collapse on a timescale shorter than that of the collision. The fractal density structure is created using the method of Whitworth (in prep). The fractal density structure is characterised by a fractal dimension $D_3 = 2.31$, and a density scaling exponent,

$$\chi = -\frac{dln(\rho)}{dln(L)}. \tag{6.3}$$

Here $\rho(L)$ is the mean density of fractal structure on length-scale L. We invoke structures that are either relatively smooth, $\chi = 0$, or very bumpy, $\chi = 8$. In the relatively smooth case the density is approximately Gaussian with the peak in the

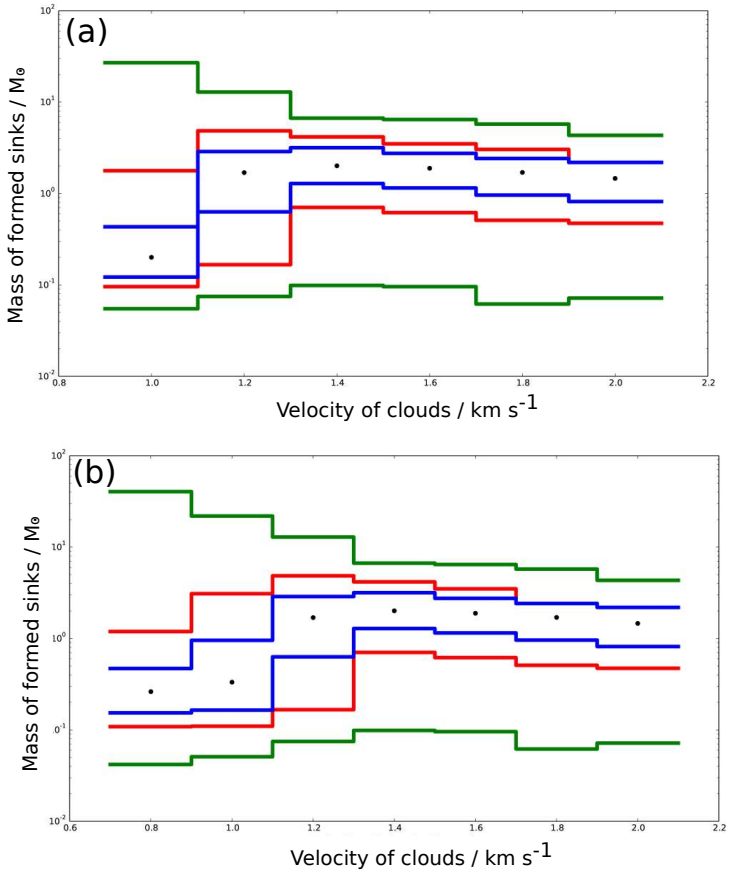

Figure 6.5. Stellar mass ranges at $t_{10\%}$, for non head-on collisions of uniform-density pre-collision clouds. (a) $b_{\circ} = 0.25\,\mathrm{pc}$ $(= R_{\circ}/8)$ and $v_{\circ} =$ 1.0, 1.2, 1.4, 1.6, 1.8 and $2.0\,\mathrm{km\,s^{-1}}$. (b) $b_{\circ} = 0.50\,\mathrm{pc}$ $(= R_{\circ}/4)$ and $v_{\circ} =$ 0.8 1.0 1.2, 1.4, 1.6 ,1.8 and $2.0\,\mathrm{km\,s^{-1}}$. For each combination of $b_{\circ}$ and $v_{\circ}$, we combine the results from five different realisations. The green lines give the full range of stellar masses, the red lines give the range between the 10^{th} and 90^{th} centiles, the blue lines give the range between the 25^{th} and 75^{th} centiles (the interquartile range), and the filled circles give the *median* mass.

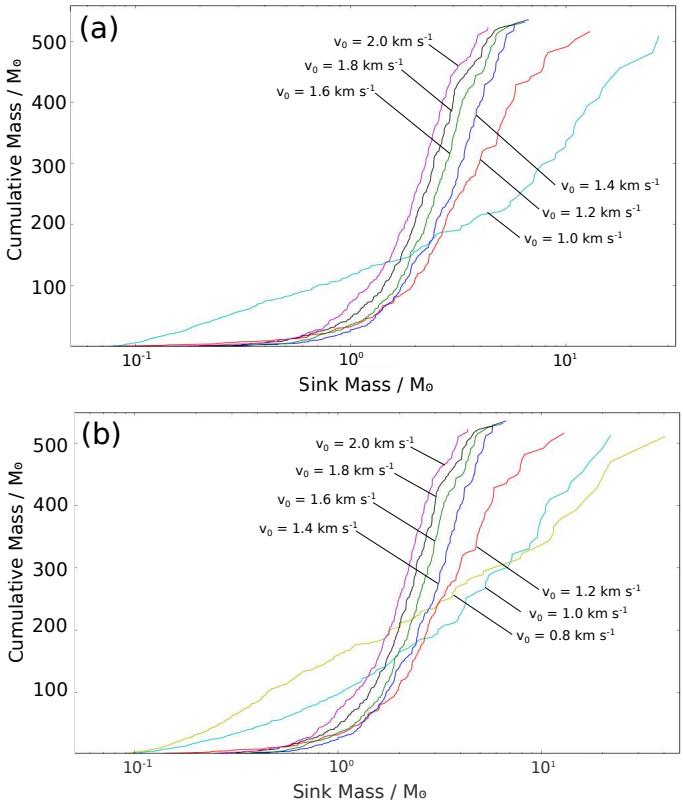

Figure 6.6. The cumulative mass distribution of the stars at $t_{10\%}$, for non head-on collisions of uniform-density pre-collision clouds. For each velocity simulated, $v_{\rm o} = 0.8\,{\rm km\,s^{-1}}$ (yellow curves), $v_{\rm o} = 1.0\,{\rm km\,s^{-1}}$ (cyan curves), $v_{\rm o} = 1.2\,{\rm km\,s^{-1}}$ (red curves), $v_{\rm o} = 1.4\,{\rm km\,s^{-1}}$ (blue curves), $v_{\rm o} = 1.6\,{\rm km\,s^{-1}}$ (green curves), $v_{\rm o} = 1.8\,{\rm km\,s^{-1}}$ (black curves), and $v_{\rm o} = 2.0\,{\rm km\,s^{-1}}$ (purple curves), we combine the results from five different realisations. Panel (a) is for impact parameter $b_{\rm o} = 0.25\,{\rm pc}$ $(= R_{\rm o}/8)$. Panel (b) is for $b_{\rm o} = 0.50\,{\rm pc}$ $(= R_{\rm o}/4)$.

centre of the cloud and is therefore equivalent to the uniform density case I present in chapter 5. However, substructure does exist at a very low amplitude; it is these small fluctuations, rather than the particle noise, that will therefore seed structure formation. The amplitude of the substructure in the bumpy case is much larger and is therefore far more influential in structure formation. As a result the initial density structure may have a direct effect on the stellar populations because the densest regions may begin to collapse independent of the collision.

In total we carry out 20 simulations, ten at each value of the density scaling exponent. Of these ten, 5 are carried out at velocity $v_{\rm CRIT} = 1.2\,{\rm km\,s^{-1}}$ and 5 at $v_{\rm CRIT} = 2.0\,{\rm km\,s^{-1}}$. Simulations with a relatively smooth density profile are used to confirm the results in chapter 5 and the simulation with a more bumpy density profile are used to determine what influence a highly fractal density profile has on the structure and star formation in a cloud-cloud collision.

Simulations are terminated once 10% of the total mass is in stars, as we do not include feedback. GANDALF is used to carry out the simulations and is configured in the same way as it was in Sec.5.1.2. However, these simulations are at a lower resolution, with each SPH particle having a mass $M_{\rm SPH} = 0.01\,{\rm M_\odot}$. As a result we cannot resolve stars much below $\sim 0.5{\rm M_\odot}$ due to computational constraints. Therefore in these simulations a Jeans length does not contain 50 SPH particles and the smallest stars are therefore not resolved fully. In order to check that this does not significantly affect our results we carry out a low resolution counterpart to a simulation from chapter 5. The cumulative mass plots for (a) low resolution and (b) high resolution at $t_{10\%}$ are shown in Fig. 6.7. The red line has collision velocity $v_0 = 1.2\,{\rm km\,s^{-1}}$ and the blue line has collision velocity $v_0 = 2.0\,{\rm km\,s^{-1}}$. We can see that the profiles follow a similar pattern, with a flatter profile at lower velocity. We do notice that the lower mass shifts to the right at low resolution. This is expected as the minimum mass we can resolve has increased. We also compare the results of the low resolution, relatively smooth density simulations to those of chapter 5. In this case we would expect to see slightly more variation because the initial conditions were created in slightly different ways. However, they should be very close because they both have approximately smooth density. We find that once again the results are similar but with a small shift to the right. As a result we conclude that although lowering the resolution will change the positions and times at which stars form, it does not alter the overall stellar populations in a significant way.

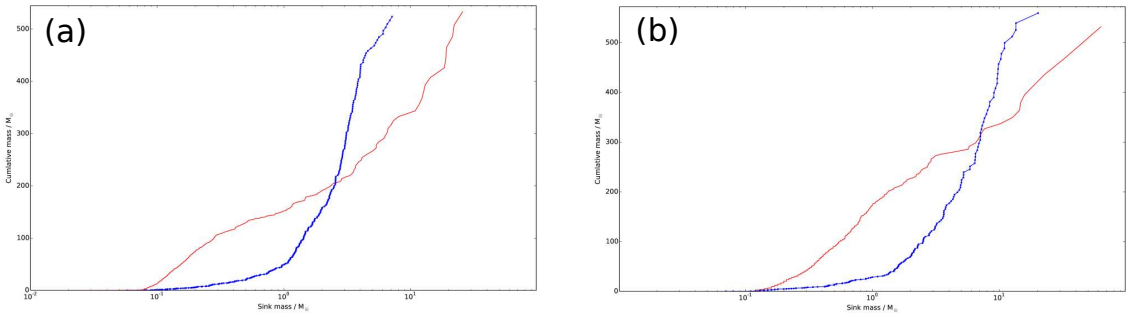

Figure 6.7. The cumulative mass,at $t = t_{10\%}$ for (a) simulations with $N_{\rm SPH} = 10^5$ and (b) $N_{\rm SPH} = 10^6$. The red line has collision velocity $v_{\rm o} = 1.2\,{\rm km\,s^{-1}}$ and the blue lines have a collision velocity $v_{\rm o} = 2.0\,{\rm km\,s^{-1}}$

6.2.2 RESULTS

The first marked difference when using a fractal density profile is the shape of the layer. In the simulations of both chapter 5 and Sec. 6.1 the layer is very flat and well defined (see Figs. 5.1 and 6.1). However, the addition of the fractal density profile, even if quite smooth, significantly alters the structure of the layer. Regions that are higher than the average density are able to penetrate further into the opposite cloud, giving the layer a less uniform structure. This effect is apparent in all simulations, but is far more pronounced in the more bumpy cases where the density variation is largest, see Fig. 6.8. However, despite this the star formation is still, in general, located towards the centre of the layer.

The relatively smooth density profile produces filamentary structures similar to those we see in chapter 5. At low velocity a large central hub is created with a few radial filaments, see image (a) of Fig. 6.9. At high velocity a spider's web is created (see image (b) of 6.9), although in this case it is not as ordered as those produced in chapter 5 because structure formation is now seeded by the underlying density structure rather than particle noise. In contrast, the more bumpy density structure does have a noticeable effect on the filamentary structure. Low velocity collisions now produce a small number of nodes which are locally hub-like (in the sense that they are fed by several radial filaments) rather than just one hub (see image (a) in Fig. 6.10). At high velocities a spider's web is still produced, but the masses and sizes of the nodes appear to be much less uniform, as illustrated in image (b) of Fig. 6.10.

We find that the stellar populations in the smooth cases are very similar to those of chapter 5. In Fig. 6.11 (a) the solid blue and red lines are the cumulative mass

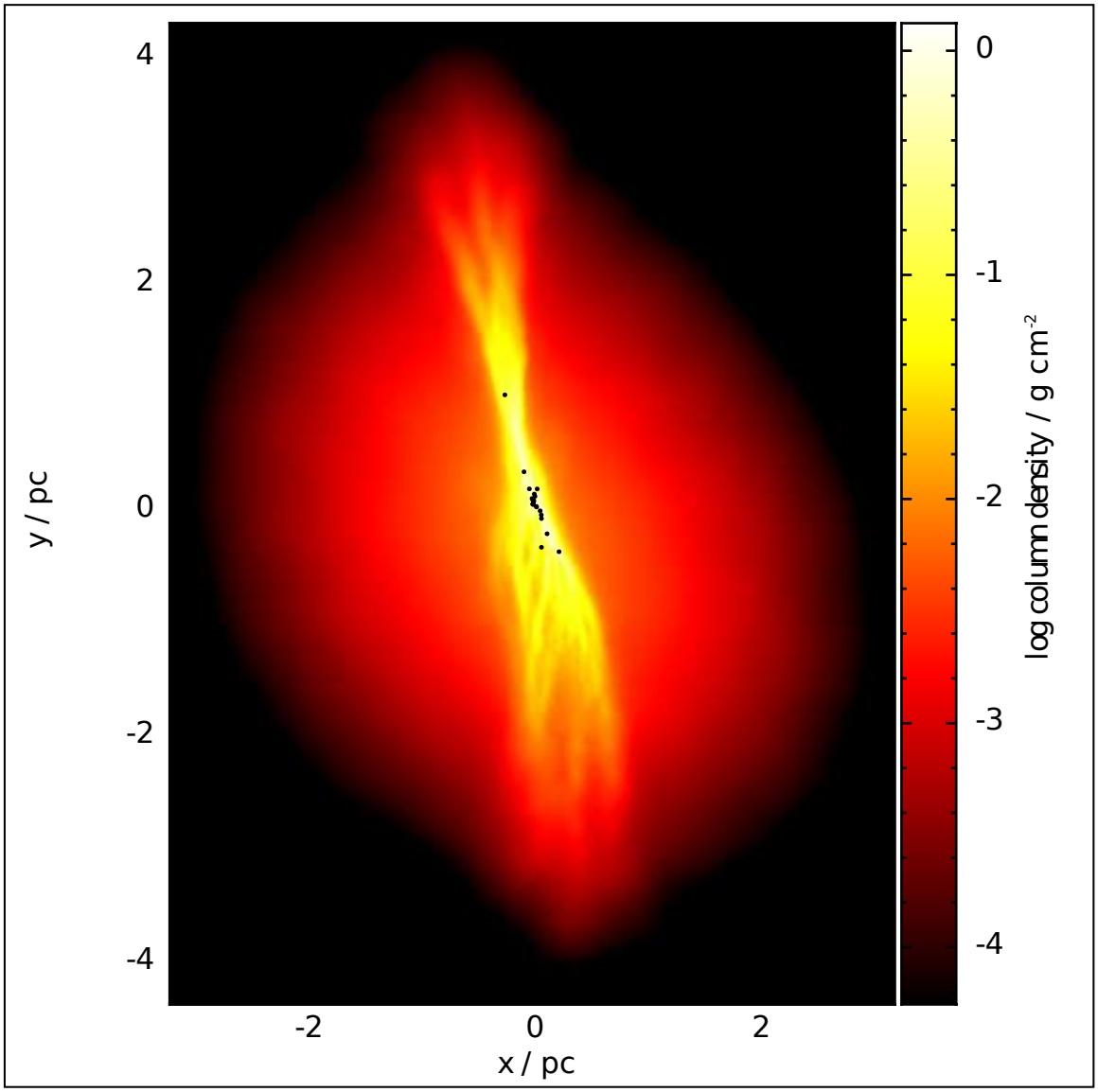

Figure 6.8. False-colour image of the colliding clouds, as seen looking across the collision axis at $t_{10\%}$ (i.e. when 10 percent of the mass has been converted into protostars). In this case the simulation has $v_o = 1.2\,\mathrm{km\,s^{-1}}$, b = 0, and a more bumpy fractal density profile, i.e. $\chi = 8$. Colour represents $log_{10}\{\Sigma/\mathrm{g\,cm^{-2}}\}$, where Σ is column-density projected on the (x,y)-plane. The black dots are protostars.

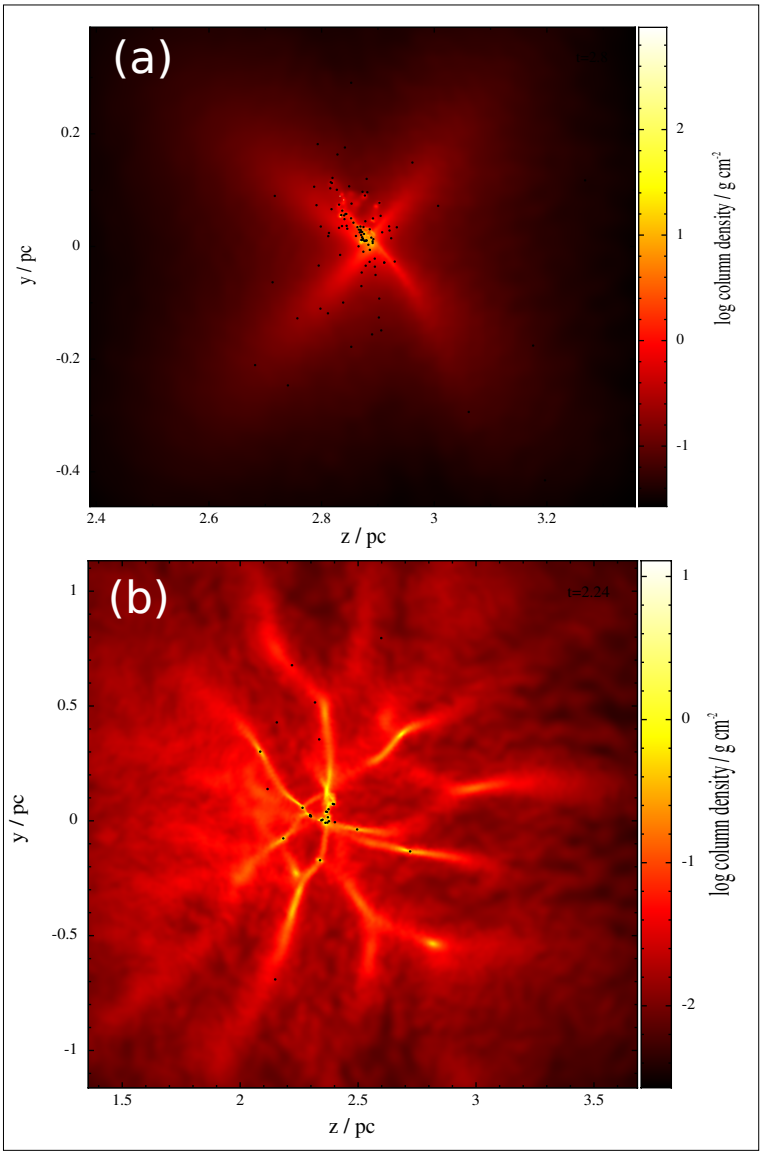

Figure 6.9. False-colour images of fragmenting layers at the moment, $t_{10\%}$, when 10% of the mass has been converted into protostars, these simulations have closest approach b = 0 and a relatively smooth fractal density, $\chi = 0$. (a) $v_{\circ} = 1.2\,\mathrm{km\,s^{-1}}$, $t_{10\%} = 2.80\,\mathrm{Myr}$. (b) $v_{\circ} = 2.0\,\mathrm{km\,s^{-1}}$, $t_{10\%} = 2.24\,\mathrm{Myr}$. Colour represents $\log_{10}\{\Sigma/\mathrm{g\,cm^{-2}}\}$, where Σ is column-density projected on the (y, z)-plane, i.e. looking along the direction of the collision. The black dots represent the protostars.

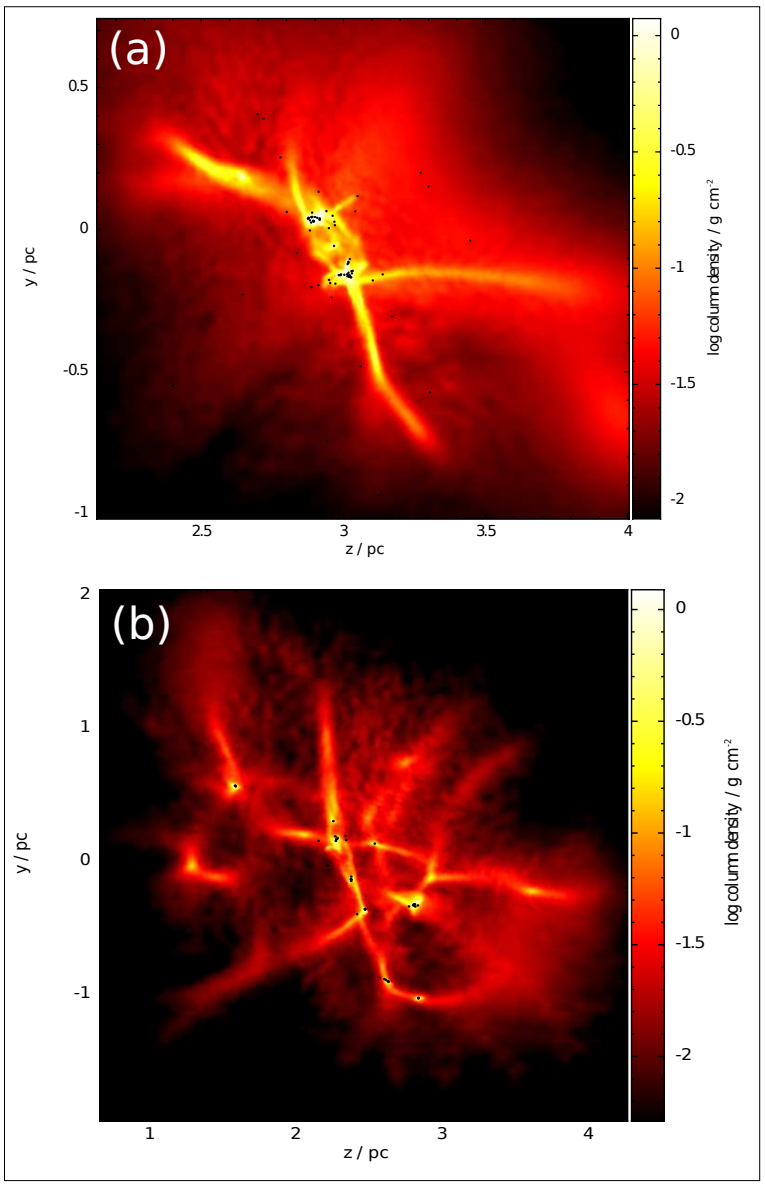

Figure 6.10. False-colour images of fragmenting layers at the moment, $t_{10\%}$, when 10% of the mass has been converted into protostars, these simulations have closest approach b = 0 and a more bumpy fractal density, $\chi = 8$. (a) $v_o = 1.2\,\mathrm{km\,s^{-1}}$, $t_{10\%} = 2.93\,\mathrm{Myr}$. (b) $v_o = 2.0\,\mathrm{km\,s^{-1}}$, $t_{10\%} = 2.39\,\mathrm{Myr}$. Colour represents $\log_{10}\{\Sigma/\mathrm{g\,cm^{-2}}\}$, where Σ is column-density projected on the (y, z)-plane, i.e. looking along the direction of the collision. The black dots represent the protostars.

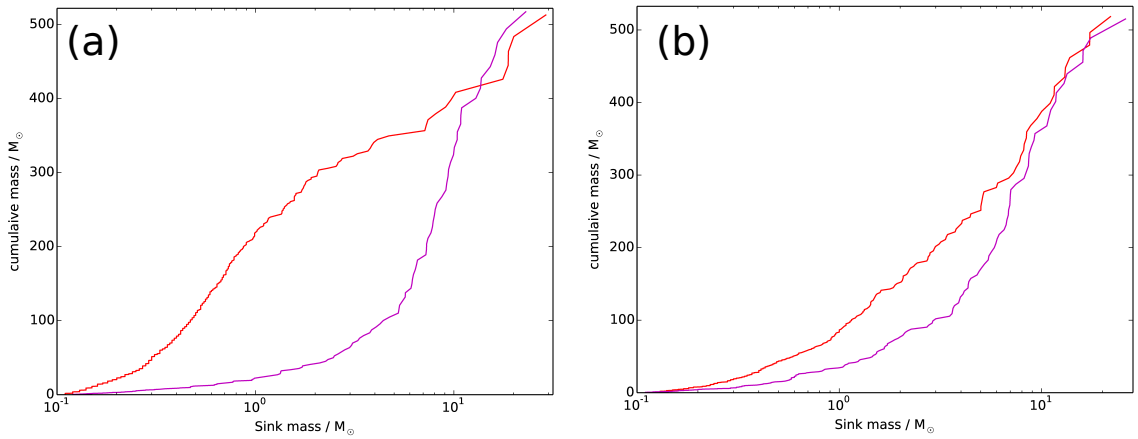

Figure 6.11. The cumulative mass distribution of the stars at $t_{10\%}$, for clouds with pre-collision density sub-structure colliding head-on. Panel (a) is for mildly clumpy sub-structure ($\chi = 0$). Panel (b) is for strongly clumpy sub-structure ($\chi = 8$). In both panels the blue curve corresponds to collision velocity $v_o = 1.2\,\mathrm{km\,s^{-1}}$, and the green curve to $v_o = 2.0\,\mathrm{km\,s^{-1}}$. In all cases the curves are obtained by combining five different realisations.

plots for the smooth low and high velocity simulations respectively. We see approximately the same results as those in chapter 5, with a distinctive difference between the stellar populations of the low velocity hub and spoke systems and the high velocity spiderweb systems. Panel (b) in the plot is the corresponding results for the bumpy simulations. In the low velocity case the amount of mass in low mass protostars becomes more sharply peaked, although the peak is still not as severe as that of the spider's web systems. This confirms that the low velocity cases begin to take on spider's web features, i.e. they consist of a few large nodes rather than one hub. In the high velocity case we see the opposite with an increase in both the number of low mass protostars and the maximum protostellar mass. This could be due to the increased mass of some of the nodes in the spider's web, which are now massive enough for competitive accretion. These trends are also present when we consider the numbers of protostars in each mass range. In Fig. 6.12 we see the median protostellar mass increases at low velocity and decreases at high velocity.

The above results suggest that adding density structure has the effect of standardizing structure formation, by this we mean it adds spider's web features to hub and spoke systems and adds hub type properties to the nodes in spider's webs. These hybrid systems have filamentary networks that are much less regular than those we have observed in previous simulations. Hybrid systems are able to produce massive stars

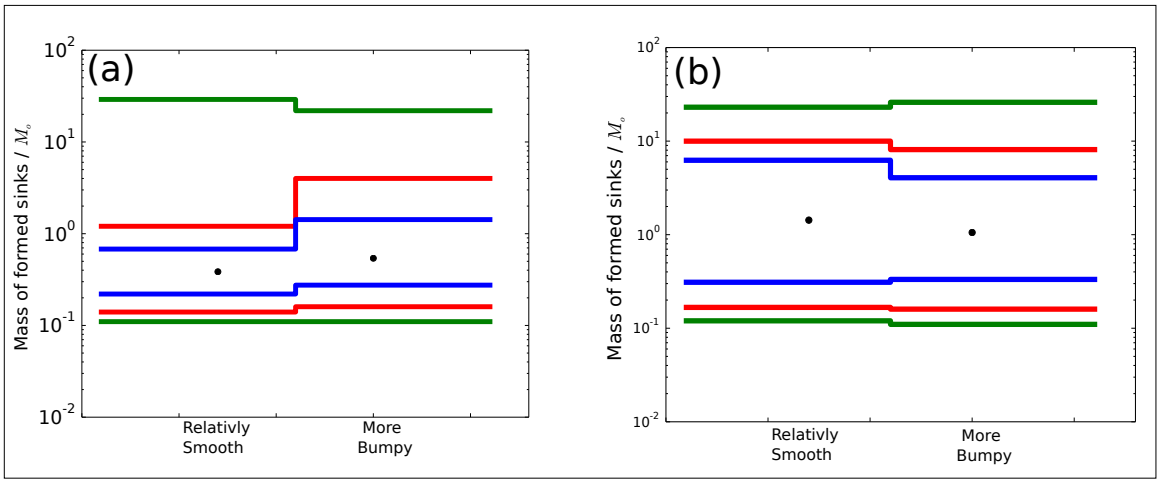

Figure 6.12. Protostellar mass ranges. For each collision velocity, $v_\circ$, we combine the data from all five realisations. The green lines give the full range of protostellar masses, the red lines give the range between the 10^{th} and 90^{th} centiles, the blue lines give the range between the 25^{th} and 75^{th} centiles (the interquartile range), and the filled circles give the median mass. The panels show the more bumpy and relatively sooth results for velocities, (a) $v = 1.2\,\mathrm{km\,s^{-1}}$ and (b) $v = 2.0\,\mathrm{km\,s^{-1}}$.

at all velocity ranges, suggesting that cloud-cloud collisions are strong candidates as locations of high mass star formation.

6.3 SUMMARY

I have explored how the structures and stellar populations discussed in chapter 5 are changed when either an closest approach, or a fractal density profile is added prior to collision. The results are summarised below:

- The critical velocity at which the filamentary network changes from a hub and spoke system, to a spider's web with nodes, is reduced as the closest approach is increased.

- As the velocity is increased beyond the critical velocity the system tends towards a spider's web with a characteristic stellar mass.

- The introduction of a fractal density profile produces a filamentary structure that is a hybrid between the two types of networks. As a result hub and spoke systems now consist of multiple local hubs rather than one central hub. The nodes in spider's web systems are no longer uniform, with some having a great deal of mass allowing competitive accretion to take place.

- The underlying fractal density structure allows massive stars to form at all velocities in contrast to the uniform cases where they could only form below the critical velocity.

Chapter 7
A new ionisation method

In this chapter I introduce a new method for treating ionising radiation within SPH simulations. It is able to locate particles which are ionised by one or more ionising sources, and can be implemented in any SPH code. For this reason we do not assume that neighbours are mutual and hence this method will also work where a neighbor gather is used. The foundations of the method are based on work by Kessel-Deynet and Burkert (2000) and Dale et al. (2007).

7.1 Single source treatment

In order to achieve ionisation balance in a density field $\rho(R\mathbf{r})$ with a central ionising source, and in the absence of a diffuse radiation field, any point $R\mathbf{r}$ on the ionisation front must satisfy,

$$\int_{\mathrm{R=0}}^{\mathrm{R=R_{IF}}} \rho^{2}(R\mathbf{r})R^{2}dR = \frac{\dot{\mathcal{N}}_{\mathrm{LyC}}m^{2}}{4\pi\alpha_{\mathrm{B}}}. \tag{7.1}$$

Here, $\alpha_{B} = 2.6 \times 10^{-13}\,\mathrm{cm^{3}\,s^{-1}}$ is the Case B recombination coefficient (i.e. only the recombinations into excited states are counted), $\rho(R\mathbf{r})$ is the mass density, m_{H} is the mean mass associated with each hydrogen nucleus and $\dot{\mathcal{N}}_{\mathrm{LyC}}$ is the output of ionising photons from the source. This equation calculates the radius at which all of the ionising photons emitted in the direction $\mathbf{r}$ have been used up balancing recombinations into excited states. Using Eqn. 7.1 we can work out which SPH particles lie within the ionisation front and are therefore ionised. Hence any particle at position $R_{\mathrm{sph}}\mathbf{r}$ that satisfies,

$$\int_{\mathrm{R=0}}^{\mathrm{R=R_{sph}}} \rho^{2}(R\mathbf{r})R^{2}dR < \frac{\dot{\mathcal{N}}_{\mathrm{LyC}}m^{2}}{4\pi\alpha_{\mathrm{B}}}, \tag{7.2}$$

is ionised.

7.1.1 NUMERICAL METHOD

In order to work out the ionisation state of a particle, one integrates along the path that connects it to the ionising source (see Eqn. 7.2). In principle this may seem trivial, but the discrete nature of SPH makes it computationally expensive to do this. Bisbas et al. (2011) approached this problem by emitting rays from the ionising source using a method based on HEALpix (Górski et al., 2005b), and then moving along the rays calculating the local densities, based on the nearby SPH particles. The routine then uses these densities to solve Eqn. 7.1 and determine how far the ray penetrates into the cloud, and hence find the edge of the HII region. In principle this method is very accurate at predicting the location of the ionisation front for a single source, but it is computationally expensive, and unable to deal with multiple sources. To overcome these restrictions we approach the problem using a reverse ray tracing scheme similar to the one used in the work of Kessel-Deynet and Burkert (2000) and Dale et al. (2007). In this method the routine begins at the particle whose ionisation state one wishes to know (henceforth known as the target particle). From there it builds an approximation of the path back to the source using the SPH particles themselves. This simplifies the integration, as we no longer need to locate all the neighbour particles of a point to work out the local density, we simply use the density of the SPH particle that defines the integration point. However, this method results in a ray that does not directly link the target particle to the source, but rather travels some indirect path between SPH particles to get there. This introduces a small amount of error into the calculation; this error can be minimised by choosing the SPH particles which most closely represent the direct path back to the source.

Prior to building the first ray, the routine searches each particle's neighbours for the one that lies closest to the line connecting the particle to the ionising source. The chosen neighbor's ID is then stored in the particle's class giving each particle a signpost to the particle that connects it back to the ionising source. Building a ray from this data is then straightforward; each SPH particle is simply connected to the next, following the signposts until we reach the ionising source (as illustrated in Fig: 7.1). In certain situations this method of particle selection can result in a ray that will not move into a less dense region than the one it is already in. This problem is illustrated in Fig: 7.2, here we see that the most appropriate link back to the ionising source lies just outside of the target particle's smoothing kernel. This results in a ray

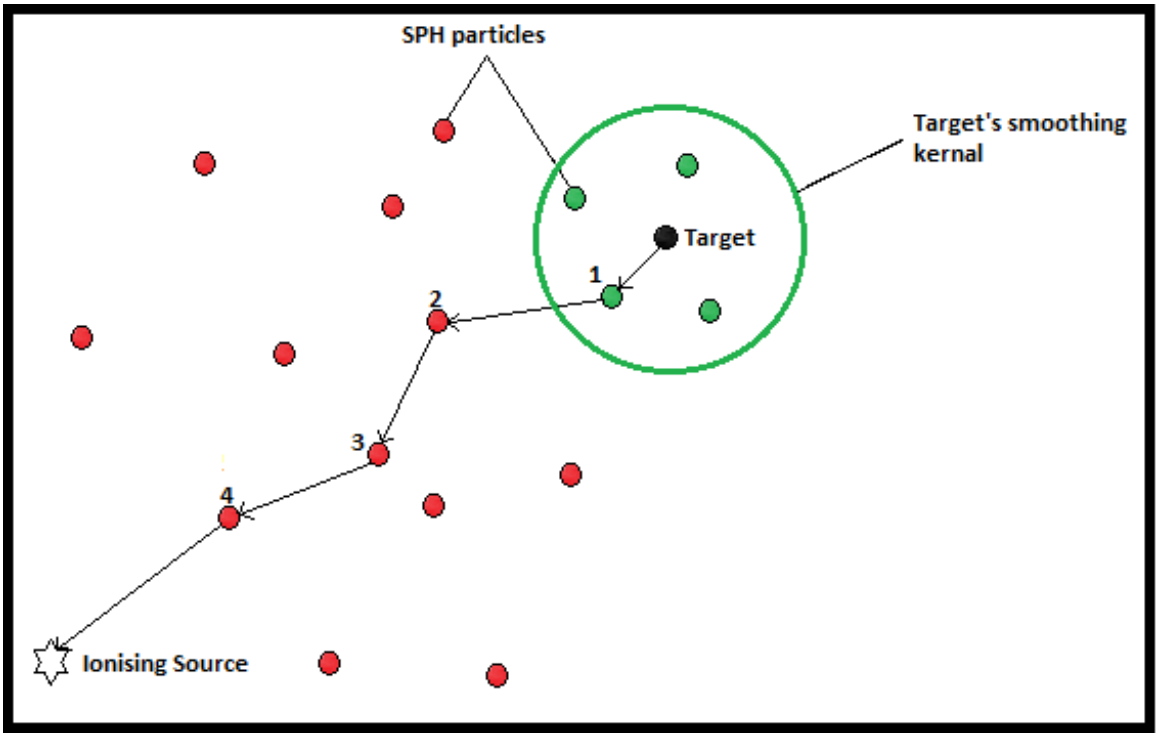

Figure 7.1. The method used to create an approximate ray from a target particle back to the ionisation source. SPH particles are illustrated by red (particles that do not lie within the target's smoothing length) and green circles (particles that lie within the target's smoothing length); the smoothing length of the target particle is shown as a green circle. In this case we join the target particle to the SPH particle that lies closest to the connecting line between the target particle and the ionisation source. We can then follow the stored ID at this particle to move to the next link in the particle chain.

that is attracted to the dense regions in the cloud and does not correctly represent the true path that a ray would take. This can lead to a particle being marked as un-ionised when it should, in-fact, be ionised. Fortunately this can be easily corrected by redefining the conditions required for a particle to be considered as a link back to the ionising source. Any particle that considers the target particle one of its neighbours is also made available as a possible link back to the source, as illustrated in Fig: 7.3. In this figure we see that particle 1 considers the target particle as a neighbour and is therefore eligible for selection as a link particle, along with the target particle's actual neighbours. Hence the ray is able to traverse the boundary between dense and less dense regions correctly.

We now have a framework that allows us to use the SPH particles as integration points, allowing us to split Eqn. 7.2 into n smaller integrals, where n is the number

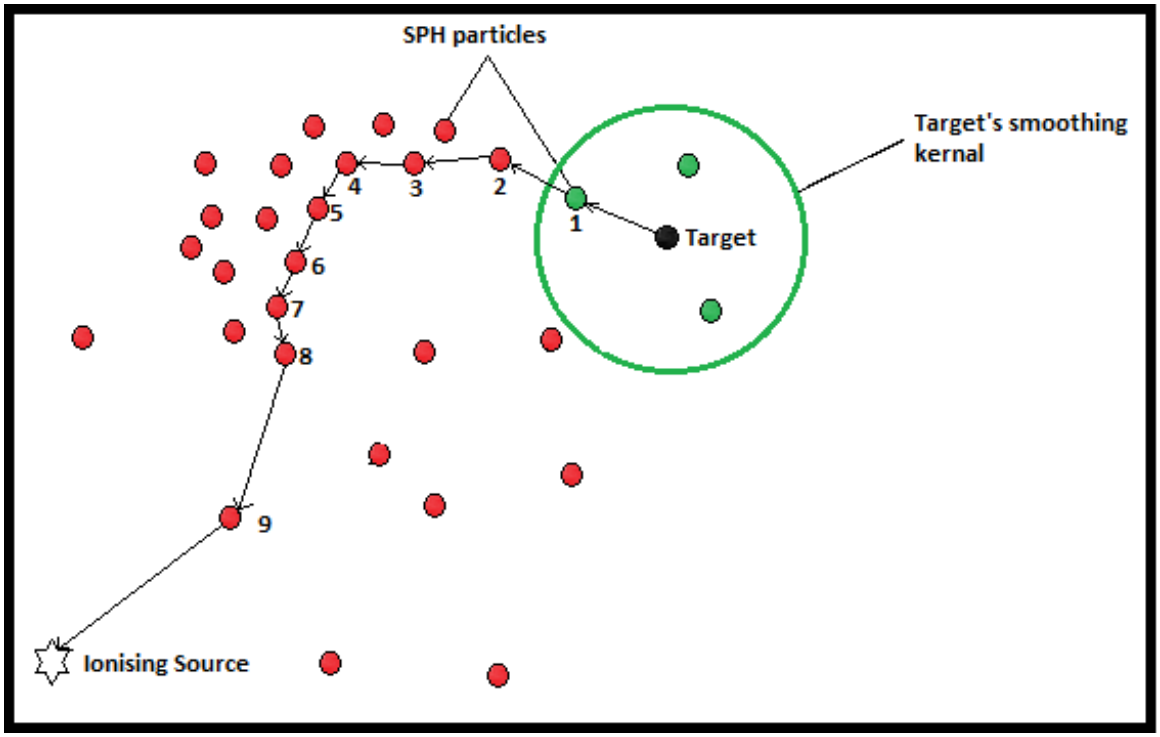

Figure 7.2. As in Fig: 7.1, the building of a ray. However in this case we are building it through a non-uniform gas. As shown, the target particle's smoothing length adds a bias in which the next link chosen is not suitable, resulting in a ray that travels through the dense material rather than crossing into the less dense region.

of SPH particles that describe the ray between the target particle and the source. By doing this we remove the radial dependence of the density, as it should vary smoothly between SPH particles that are neighbours, and hence it is suitable to take an average. Eqn. 7.2 therefore becomes:

$$\sum_{i=1}^{n} \int_{R=R_{\rm i}}^{R=R_{\rm i+1}} \left(\frac{\rho_{\rm i} + \rho_{\rm i+1}}{2} \right)^2 R^2 dR < \frac{\dot{\mathcal{N}}_{\rm LyC} m^2}{4\pi\alpha}. \tag{7.3}$$

This equation can then be simplified further as the integral has an exact solution,

$$\sum_{i=1}^{\rm n} \left(\frac{\rho_{\rm i} + \rho_{\rm i+1}}{2} \right)^2 \left(\frac{R_{\rm i+1}^3 - R_{\rm i}^3}{3} \right) < \frac{\dot{\mathcal{N}}_{\rm LyC} m^2}{4\pi\alpha}, \tag{7.4}$$

where $R_{\rm i} = \|\mathbf{R}_{\rm i} - \mathbf{R}_{\rm source}\|$ and i represents the next particle in the chain, with $i = 1$ being the source, i = 2 being the next particle in the chain and so on until we reach the target particle.

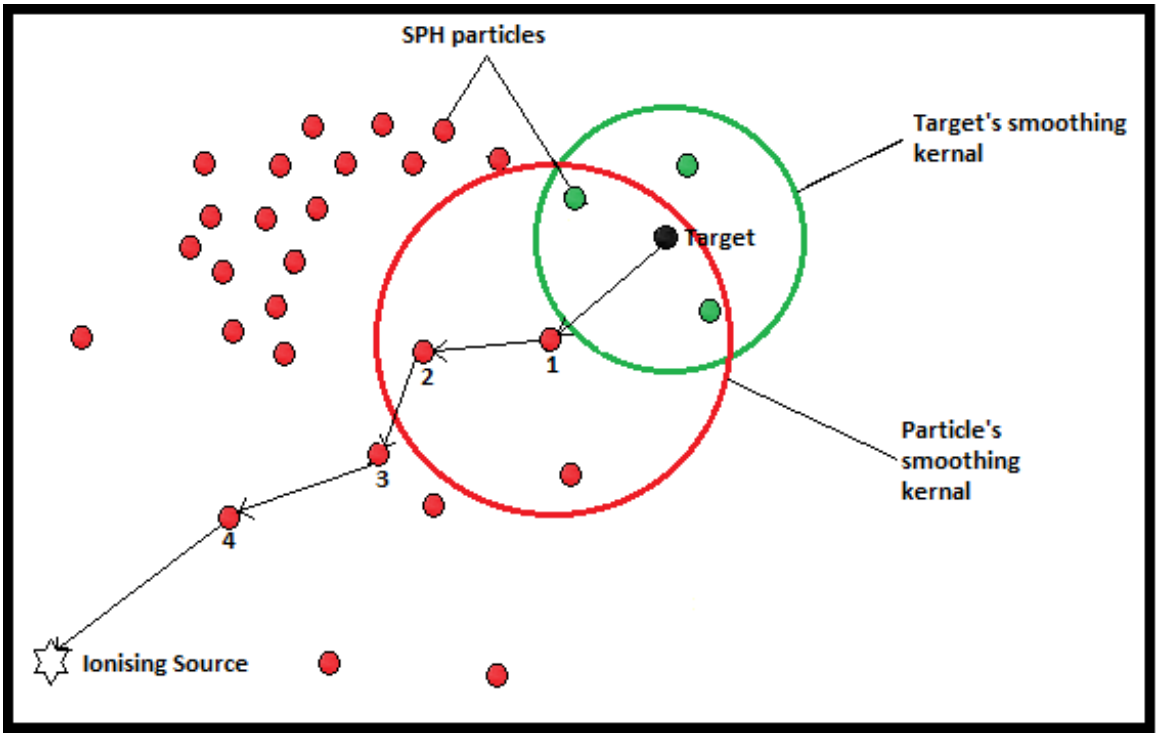

Figure 7.3. The building of the same ray as the one in Fig: 7.2. In this case we apply a fix in which we also consider particles that have the target particle as a neighbour, such as the particle at the center of the red circle. In this case we are able to make a more appropriate link back to the ionising source

7.1.2 Temperature smoothing

It is well known that SPH has difficulty dealing with sharp changes of temperature, such as the one that is encountered between ionised gas at $T \sim 10^4$ K and neutral gas at $T \sim 10$ K. The large temperature and pressure gradients cause a gap to open up between the neutral and ionised gas (see panel A of Fig: 7.4). This gap becomes so large that the ionised and neutral SPH particles do not lie within each others smoothing kernels. As a consequence of this gap no new particles can be ionised and the mass of the HII region cannot increase, resulting in an under-prediction of the pressure terms, so that the HII region does not expand at the correct rate (this is illustrated in Fig: 7.5). This problem is easily corrected by smoothing the temperature gradient across the ionisation front. To do this, the routine takes any neutral particle that lies within 3h of an ionised particle and smooths the temperature using the M4 cubic spline kernel (Monaghan and Lattanzio, 1985) with smoothing length 3h; in this regime a particle's temperature can be smoothed by more than one ionised particle, in such situations we use the largest temperature calculated. By applying this smoothing we are able to prevent the gap from forming, as can be seen in panel

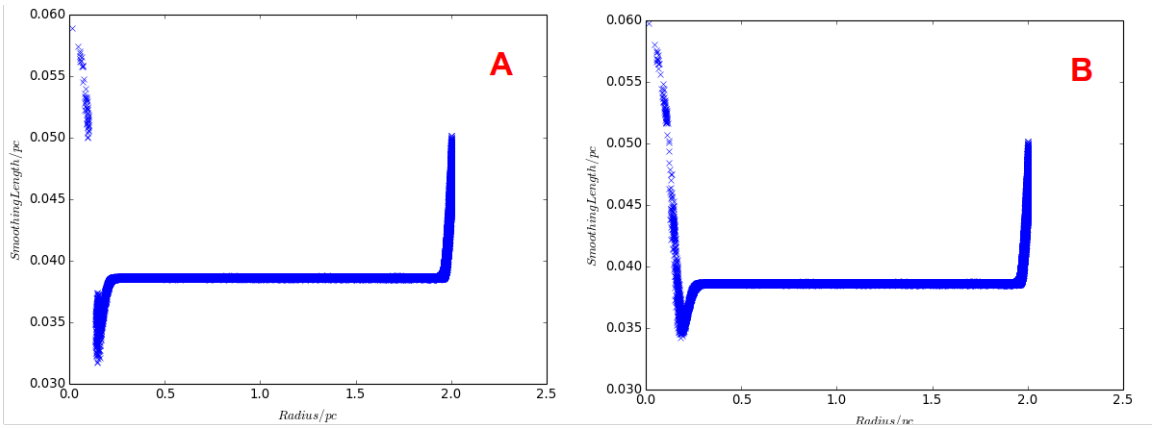

Figure 7.4. The smoothing length of particles as a function of radius at time $t = 0.01\,\mathrm{Myr}$. Panel A on the left is for the simulation where we do not include temperature smoothing, you can clearly see a break where a discontinuity has formed. In comparison, panel B shows a simulation with the temperature smoothing included, and here we see no break.

B of Fig: 7.4. This allows new particles to become ionised and the HII region to expand correctly.

7.1.3 TESTING THE SPITZER SOLUTION

It is very difficult to test a routine that simulates ionising radiation because there are few analytical predictions to which one can compare. The most robust prediction is that by Spitzer (1978), who shows that the radius of an HII region in a uniform non-gravitating cloud is given by,

$$R_{\mathrm{IF}}(t) = R_{\mathrm{St}}\left(1 + \frac{7}{4}\frac{c_{\mathrm{HII}}t}{R_{\mathrm{St}}}\right)^{4/7}. \tag{7.5}$$

Here R_{St} is the Stromgren radius. It is useful to carry out this test on a low $\dot{\mathcal{N}}_{\mathrm{LyC}}$ star to ensure that the HII region expands slowly and remains in the cloud for a longer period of time. We find that our results very closely match the prediction of Spitzer (1978) for almost the entire evolution of the HII region, with only a small deviation at the end, as the HII region approaches the edge of the cloud. We present these results in Fig: 7.6, where the red crossed line illustrates the simulation results and the blue line plots the results as predicted by Eqn. 7.5.

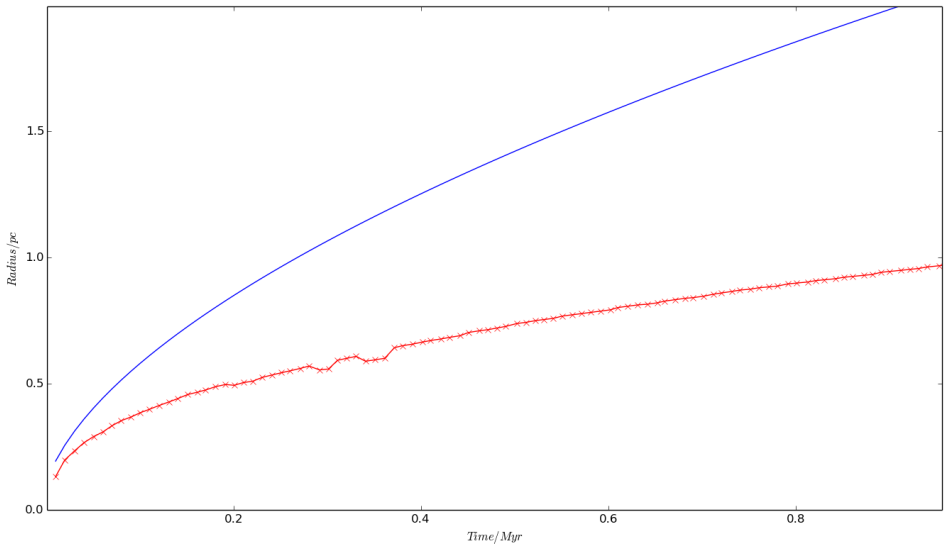

Figure 7.5. The results of a simulation designed to reproduce the Spitzer solution. In this case temperature smoothing has not been turned on. The blue line indicates the location of the ionisation front as predicted by the Spitzer solution (Spitzer, 1978) and the red line indicates the location of the densest part of the shell, which should lie just beyond the ionisation front.

7.2 Expanding the method to multiple sources

Currently this routine is only able to determine the radius of the HII region created by a single ionising star. However, an ionising star is unlikely to form in isolation and so the routine must be modified so that it can determine the structure of an HII region if there are multiple ionising sources. Initially when the HII regions of the sources do not overlap the routine can simply treat each source independently. As the simulation progresses, and the HII regions beginning to overlap, the routine must determine what fraction of the material is ionised by each source and adjust the radius of the HII region accordingly. It does this by defining the photon proportion,

$$P_{\mathrm{i,j}} = \frac{k_{\mathrm{i-1,j}}\,\mathcal{N}_{\mathrm{i,j}}}{\sum_{j'=0}^{S}\{k_{\mathrm{i-1,j'}}\,\mathcal{N}_{\mathrm{i,j'}}\}}, \tag{7.6}$$

which is the proportion of photons arriving at particle i from source j. $\mathcal{N}_{\mathrm{i,j}}$ is the number of photons arriving at the particle i from source j in the current timestep, S is the number of sources, and $k_{\mathrm{i-1,j}}$ describes the ionisation state of particle i − 1 for source j, i.e. it is set to one if it is ionised and zero if not. This allows us to determine the fraction of photons available from each source to ionise the current particle. We

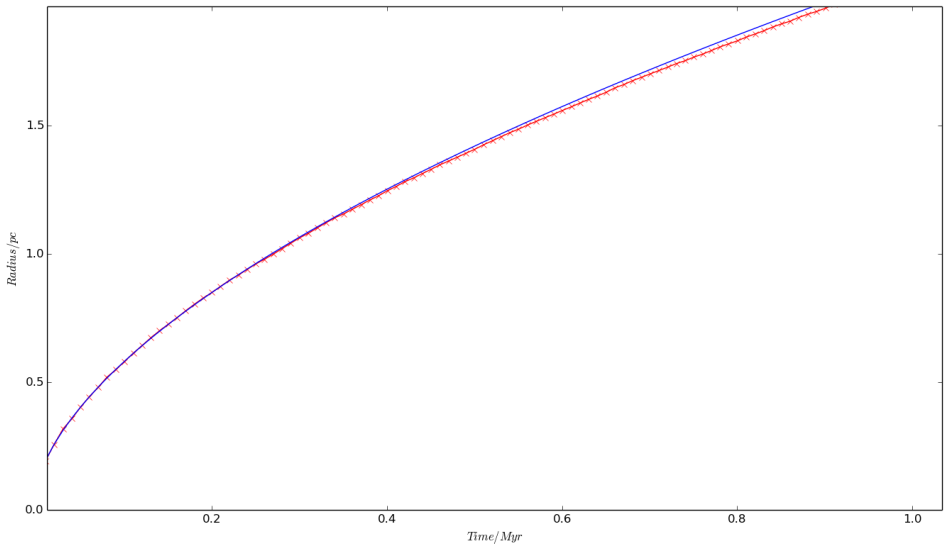

Figure 7.6. The results of a simulation designed to reproduce the Spitzer solution. In this case temperature smoothing has been turned on. The blue line indicates the location of the ionisation front as predicted by the Spitzer solution (Spitzer, 1978), and the red line indicates the location of the densest part of the shell, which should lie just beyond the ionisation front.

can then incorporate this term into Eqn. 7.3,

$$\sum_{i=1}^{n}\sum_{j=1}^{S} P_{\mathrm{i,j}}\left(\frac{\rho_{\mathrm{i}}+\rho_{\mathrm{i+1}}}{2}\right)^{2}\left(\frac{R_{\mathrm{i+1}}^{3}-R_{\mathrm{i}}^{3}}{3}\right) < \frac{\dot{\mathcal{N}}_{\mathrm{LyC}}m^{2}}{4\pi\alpha}\,. \tag{7.7}$$

Though only a small modification to the equation; this change has a large impact on the numerical implementation of this method. The equation is now dependent on the ionisation state of all the particles connecting the target particle to the ionising source, i.e. changing the ionisation state of any particle can result in a large number of changes throughout the system. As a result, we can no longer accept the first solution returned by the code, instead we must iterate until the system converges to a stable solution. We consider the solution stable once the no particles have changed ionisation state for two iterations.s This solution will then represent the correct ionisation structure at the current time step.

Table 7.1. This table shows how the routine scales with the number of sources and the number of particles. The simulations were performed with a routine embedded into the GANDALF SPH code. The times given are CPU times, which are the times taken across all 16 processors. To work out the wall time (actual run time) one must divide the numbers in the table by 16, i.e. with $N_{\rm source} = 1$ and $N_{\rm SPH} = 10^6$ the routine takes 2.4 s to run.

	$N_{\rm source} = 1$	$N_{\rm source} = 2$	$N_{\rm source} = 4$
$N_{\rm SPH} = 10^4$	0.288 s	0.448 s	0.784 s
$N_{\rm SPH} = 10^5$	3.04 s	4.48 s	6.4 s
$N_{\rm SPH} = 10^6$	38.4 s	72 s	142.4 s

7.3 Computational cost

I have carried out a number of simulations to ensure that the routine is not computationally expensive. I examine how the routine run time scales when the number of sources or the number of particles is increased. I also compare the simulation times achieved by my routine to those of other routines that simulate ionising radiation.

Tab. 7.1 shows the time scalings of the routine when either the number of sources, or the number of particles, is increased; these benchmarks are based on simulations carried out with the routine included in the GANDALF SPH code. The routine scales approximately linearly with the number of sources, performing better when the sources are isolated and their HII regions do not overlap. No additional iterations are required in these cases and the routine achieves a scaling of $N_{\rm source}$ or better. More iterations (around ten) are required once the HII regions begin to overlap and the number of sources begins to have a larger impact on the computational time.

The routine achieves an approximately linear scaling with the number of particles. This scaling is achieved because the code is written so that each particle is checked as few times as possible, in most cases only once per iteration, therefore doubling the number of particles simply doubles the number of calculations, and hence the computational time.

We compare this routine to the one added to SEREN by Bisbas et al. (2011), who, for $N_{\rm SPH} = 10^6$ find that the CPU time varies (total amount of time used by all CPUs) between $10\,{\rm s} < {\rm t_{CPU}} < 700\,{\rm s}$ depending on the number of ionised particles within

the simulation. In comparison we achieve an average CPU time of $t_{\rm CPU} \sim 38.4\,{\rm s}$. This does vary depending on the amount of time it takes for the system to converge, and hence how greatly the new solution differs from the previous one. It therefore follows that the very first solution takes the longest to find with the rest falling within a gaussian around the average time. We can see all of these features in Fig: 7.7, which is the probability distribution function of the CPU times taken for the routine over the entire simulation. The bin on the far right at time $t_{CPU} \sim 94\,{\rm s}$ is for the first step. Unlike Bisbas et al. (2011) we see very little variation as the number of ionised particles increases. Multiple sources do increase the average time slightly due to the overlap of HII regions which increases the number of iterations required for the system to converge. My method offers a significant improvement in computational cost compared to other routines, with only a small reduction in accuracy which results from using SPH particles as integration points.

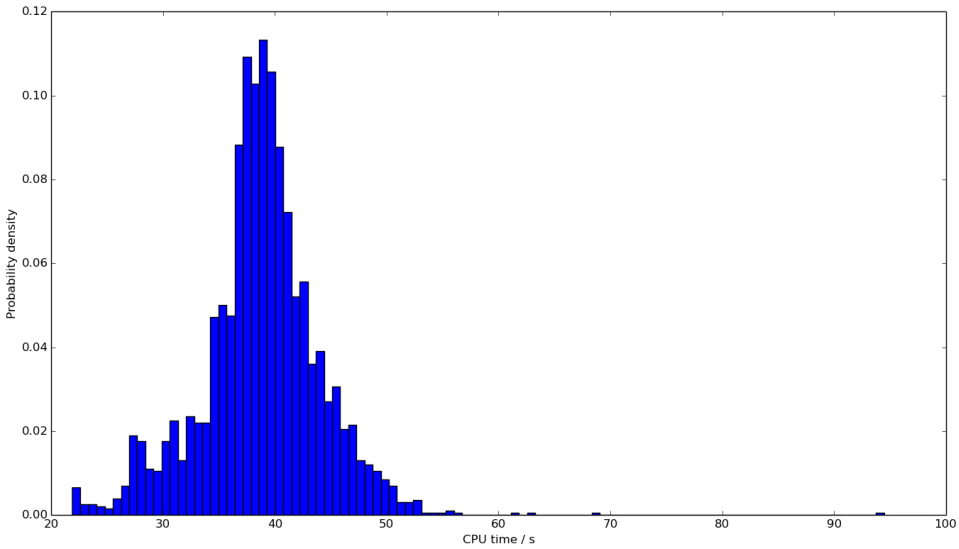

Figure 7.7. The probability distribution function of the CPU time taken to calculate the ionisation state of the gas for one time step over the entire simulation.

Chapter 8
Cloud-cloud collisions : Photoionising feedback

In the chaptes 5 and 6 we have shown that massive star formation can be triggered by cloud-cloud collisions. These stars will produce a large amount of ionising radiation and may trigger or suppress further star formation. In this chapter we repeat the simulations performed in Sec. 6.2 but introduce ionising radiation from stars that have mass $M > 23\,\mathrm{M}_{\odot}$. We then explore what impact this radiation has on the cloud structure and subsequent star formation.

8.1 Simulation set up

In this chapter we carry out four simulations which are based on those carried out in Sec. 6.2. We repeat the simulations for all combinations of $v = 1.2$ and $2.0\,\mathrm{km\,s^{-1}}$ and $\chi = 0$ and 8, where we recall that $\chi = 0$ means a relatively smooth initial clouds and $\chi = 8$ means a more bumpy initial clouds.

We use the routine described in chapter 7 to model the ionising radiation from massive stars. It would be ideal to model the ionising radiation of all the stars in the simulation. However, calculating the location of so many HII regions would be extremely expensive. Moreover, we do not have the resolution to accurately resolve the HII regions of the smaller stars. In these cases it may only take one or two SPH particles to use up all of the ionising photons. In SPH we require around 100 particles to fully resolve any given HII region. Hence we can only model an HII region if it is massive enough to be modeled by more than 100 SPH particles. For these reasons we only model the HII regions of stars that have a mass greater than $23\,\mathrm{M}_{\odot}$ and hence a Lyman continuum output of $\dot{\mathcal{N}}_{\mathrm{LyC}} \geq 10^{48}\,\mathrm{s}^{-1}$

Previously we have terminated simulations once 10% of the total mass has been converted into stars, on the assumption that this is the approximate time that stars would begin to produce enough feedback to disrupt the system. In order to explore the role feedback plays in star formation we allow the simulations to run past this point. The simulations are allowed to run until star formation has ceased, i.e. no more SPH particles have accreted onto stars for the last 10 snapshots (0.1 Myr) .

We explore the shapes of the HII regions that form and determine if they promote or terminate star formation. We determine if the stellar populations found after feedback differ greatly from those we found in chapter 6.

8.2 RESULTS

8.2.1 BIPOLAR HII REGIONS

An HII region is quickly formed once a star becomes massive enough to produce ionising radiation. This HII region can have a range of morphologies, and these are highly dependent on whether the star remains in the layer, or is ejected from the layer. The way these regions appear can also depend heavily on the angle from which the HII region is viewed. In these results we will discuss the cases when the HII region is viewed either along, or perpendicular to the collisions axis.

Star remains in layer

When the HII region is viewed perpendicular to the axis of collision it appears as a bipolar HII region, an example of which is shown in Fig. 8.1 (a) and (b).

Here, the colour in panel (a) represents $log_{10}\{\Sigma/\mathrm{g\,cm^{-2}}\}$ of all the gas in the simulation, where Σ is column-density projected on the (x,y)-plane. The colour in panel (b) represents $log_{10}\{\Sigma/\mathrm{g\,cm^{-2}}\}$ for non-ionised gas, and the colour in panel (b) represents the Emission Measure,

$$EM = \int_{l=\mathrm{inf}}^{l=0} n_{\mathrm{p}}(l) n_{\mathrm{e}}(l) dl. \tag{8.1}$$

The initial clouds used in this simulation contain a large amount of substructure prior to collision, i.e. they have a large density scaling exponent, ξ. We can see evidence of this in the layer, which is only approximately aligned with the (vertical) y-axis. Projecting out perpendicular to the plane of the layer there are two large bubbles.

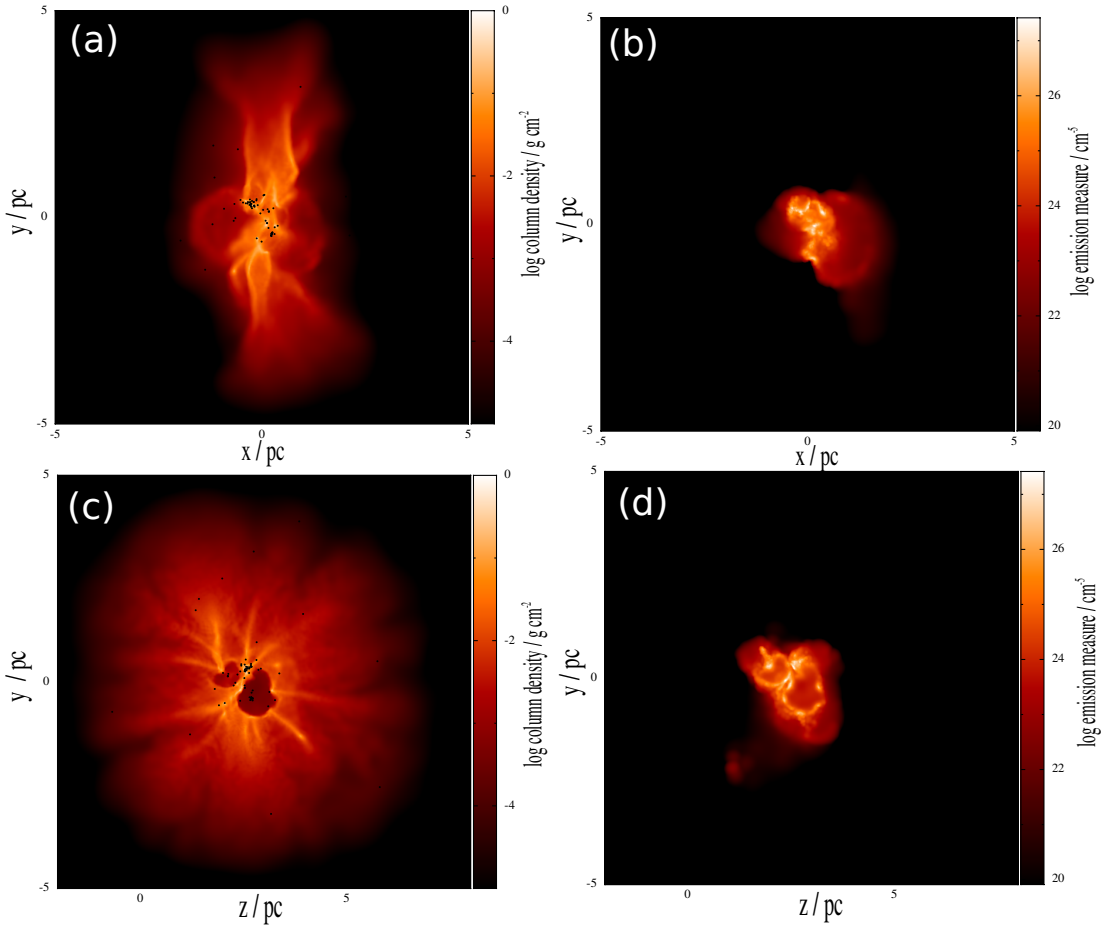

Figure 8.1. Case A. False-colour images of two clouds with strongly clumpy pre-collision internal sub-structure ($\chi = 8$), undergoing a head-on collision at relatively high velocity ($v_{\rm o} = 2.0\,{\rm km\,s^{-1}}$); the time is $t = 2.88\,{\rm Myr}$. The images on the top line (a and b) are views looking across the collision axis, and those on the bottom line (c and d) are views looking along the collision axis. The lefthand panels (a and c) show the logarithm of the column-density of the neutral gas, i.e. $\log_{10}(\Sigma_{\rm I}/{\rm g\,cm^{-2}})$; the black dots are protostars. The righthand panels (b and d) show the logarithm of the emission-measure, i.e. $\log_{10}(EM/{\rm cm^{-5}})$, highlighting the ionised gas.

These are the lobes of a bipolar HII region created by a star within the layer. There is also a clear gap in the layer where the HII region has blown a hole. This hole connects the two lobes and is located around $x = 0\,\mathrm{pc}$, $y = 0.2\,\mathrm{pc}$. If we look at the right hand lobe we can also clearly see the dense outer shell of the HII region. Zooming in, as we have done in Fig. 8.2, allows us to see this more clearly. There is also some indication of small over-densities in this shell. However, these regions do not go on to form stars because the outer shell of the lobes has very low density and is expanding rapidly. There is no clear indication of bright rimmed clouds or elephant trunks, which can form stars via radiation driven implosion. These may not be visible due to our resolution, or it may be that there is no gas dense enough to form them, i.e. gas is evaporated too quickly for such structures to survive.

When viewed along the collision axis one observes a circular HII region, an example of which is shown in panels (c) and (d) of Fig. 8.1. In this image we can see a large HII region has formed within the filamentary system. This part of the HII region is connecting the two lobes discussed in the last paragraph. Once formed the HII region has blown open the filamentary network, creating a hole. There is clear evidence of the filaments that originally created the ionising star and we can see that they now no longer extend to the centre of the layer but stop once they reach the outer edge of the HII region. It is at this location we may see dense regions that have the potential to form additional stars. These dense regions are a result of the HII region sweeping up the layer. The density of the ring in this image is much greater than the shell bounding the lobes of the HII region. This is because the shell is expanding into the layer and therefore sweeps up far more mass. From this angle one would find it hard to identify this as a bipolar HII region. Instead one may determine that this HII region has a cylindrical shape due to the large density of this circular shell compared to the density you would view when looking through the centre of the HII region. There are examples of such observations (Beaumont and Williams, 2010), in which the authors suggest they have observed cylindrical HII regions. We suggest that the features they observe may be due to bipolar HII regions. We did not observe any star formation in the shells of the lobes, but we do see some stars in and around the ring of this part of the HII region. Some of these stars seem to be close to a location where a filament meets the shell, suggesting they could be triggered; we will discuss this later in the chapter.

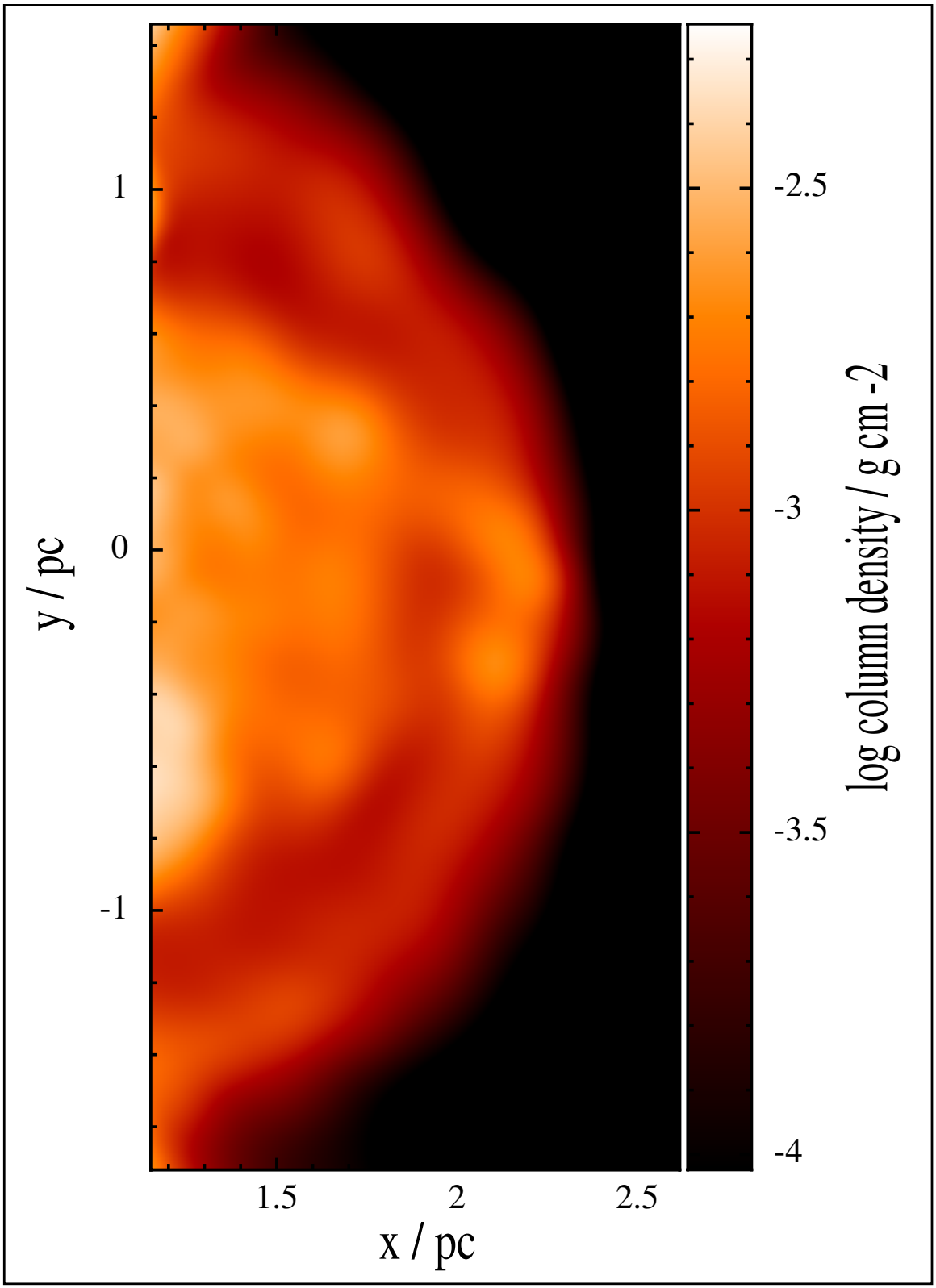

Figure 8.2. False-colour image of the colliding clouds, as seen looking across the collision axis at $t = 2.88\,\mathrm{Myr}$, focusing on one of the lobes of the bipolar HII region. The simulation has parameters: $v_o = 2.0\,\mathrm{km\,s^{-1}}$, b = 0 and has a more bumpy fractal density profile initially, i.e. $\chi = 8$. Colour represents $log_{10}\{\Sigma/\mathrm{g\,cm^{-2}}\}$, where Σ is column-density projected on the (x,y)-plane.

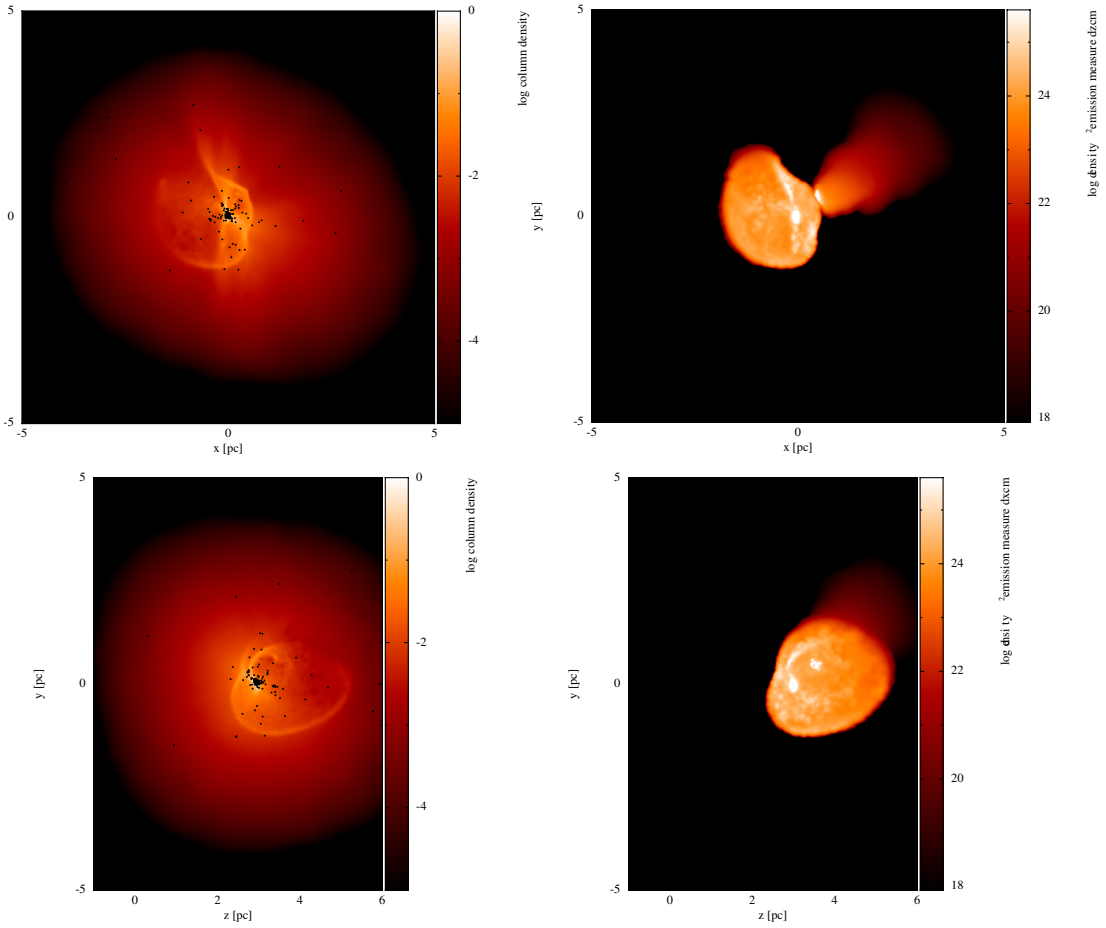

Figure 8.3. As Fig. 8.1, but for Case B, which involves two clouds with strongly clumpy pre-collision internal sub-structure ($\chi = 8$), undergoing a head-on collision at relatively low velocity ($v_{\rm o} = 1.2\,{\rm km\,s^{-1}}$); the time is $t = 3.20\,{\rm Myr}$.

Star ejected from layer

An HII region of an ejected star viewed perpendicular to the collision axis appears as an approximately spherical HII region, an example of which is shown in Fig. 8.3 (a) and (b). Once again the clouds used in this simulation have a large amount of initial substructure. In this case the ionising star has been ejected from the layer and has moved left. If one looks at the emission measure (panel (b)) one can see that the HII region has an approximately spherical structure. The right hand side of the HII region is pushed up against the layer which is very dense. This acts as a barrier and slows the HII regions expansion. There are no stars coincident with the bounding shell of the HII region, suggesting that no star formation has been triggered in this simulation.

When viewed along the collision axis one once again observes an approximately spherical HII region. This is shown in Fig. 8.3 (c) and (d) where we plot the column density of neutral gas (panel (c)) and the emission measure (panel (d)) of the ionised gas (i.e. gas with $T > 1000$K). Looking at panel c we see that the HII region is spherical in shape. However, if we look at the other panel (d) we can see that the shell bounding the HII region is not complete, rather we only see part of it. In general the shell bounding the HII region is low density when compared to the density of the layer and does therefore not show up in the column density plots. However, in locations where the HII is sweeping up material from the layer the density of the bounding shell can become large enough to become visible.

8.2.2 Termination of star formation

We find that feedback has an effect on star formation as well as on the structure of the layer. Our simulations suggest that once feedback begins it very rapidly terminates star formation. We can see evidence of this in the Figs. 8.1 and **??** where we see the HII region disrupting the filamentary structure in which star formation was previously occurring. We can see this termination more clearly if we look at the plot of total stellar mass as a function of time, shown in Fig. 8.4. In this figure we start the plot at 2.2 Myr, but we note that there is star formation prior to this. In chapter 6 we stop the simulations once the total stellar mass is 10% of the total mass, i.e. when $M = 100\,\mathrm{M}_\odot$. In the case of feedback, we see the total stellar mass continues to grow until the first star becomes massive enough to produce feedback. Following this star formation is very quickly terminated. We see this termination in all our simulation, although the time at which it occurs is highly dependent on the point at which the feedback begins. In some simulations, during the feedback phase, we see small increases in the rate at which gas mass is converted to stellar mass; this can be seen in the blue line at around 2.0 Myr. We find that these increases are due to the formation of new stars, and that these stars tend to be forming in the parts of the HII shell which are within the layer. This could suggest that they are triggered by the HII region. However, the number of triggering events is very small. This leads us to the conclusion that, following a cloud-cloud collision, the main effect of feedback from the initial burst of star formation is to terminate subsequent star formation. The resulting star formation efficiency ranges from 20% to 40% depending on the collision velocity.

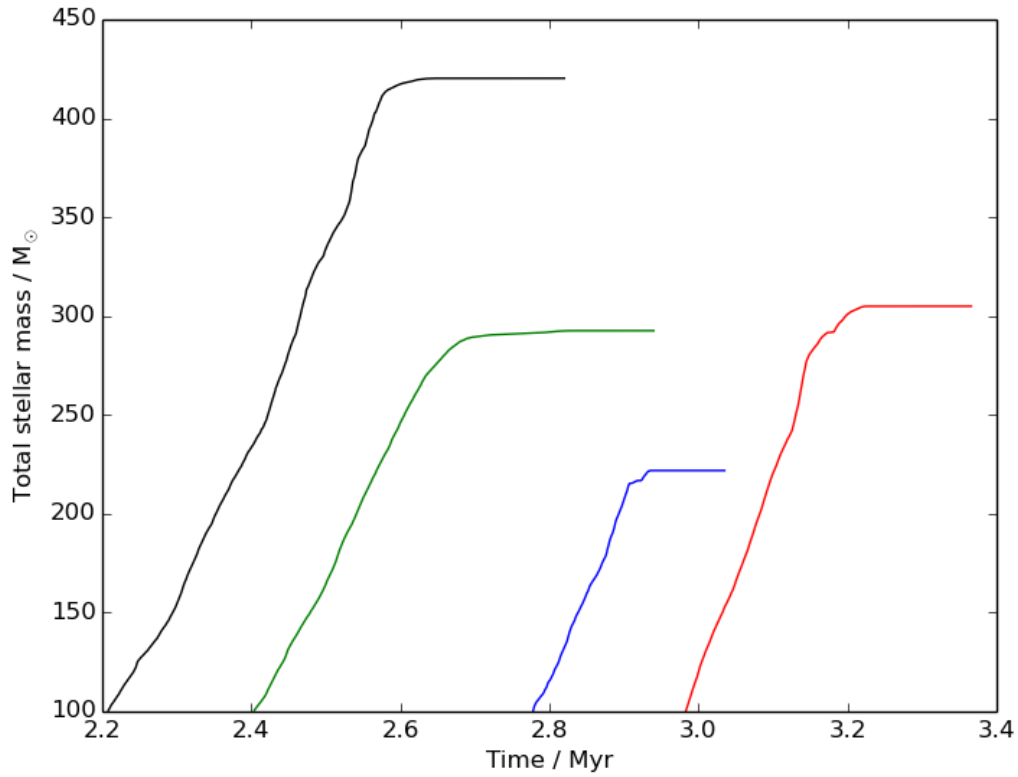

Figure 8.4. The total stellar mass as a function of time: $(v_\circ, \chi) = (1.2\,\mathrm{km\,s^{-1}}, 0)$, blue; $(1.2\,\mathrm{km\,s^{-1}}, 8$; Case B), red; $(2.0\,\mathrm{km\,s^{-1}}, 0)$, green; $(2.0\,\mathrm{km\,s^{-1}}, 8$; Case A), black.

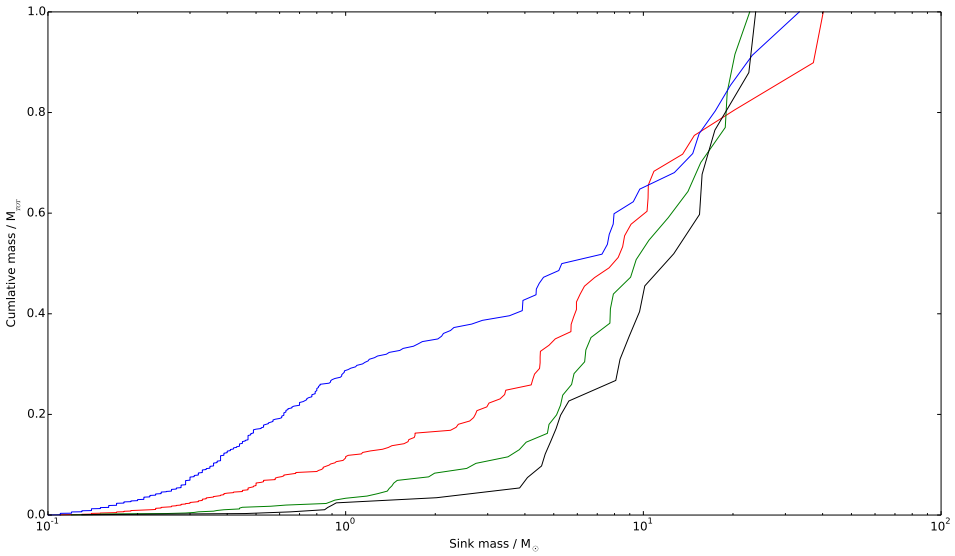

Figure 8.5. The normalised cumulative mass function: $(v_{\circ}, \chi) = (1.2\,\mathrm{km\,s^{-1}}, 0)$, blue; $(1.2\,\mathrm{km\,s^{-1}}, 8;$ Case B), red; $(2.0\,\mathrm{km\,s^{-1}}, 0)$, green; $(2.0\,\mathrm{km\,s^{-1}}, 8;$ Case A), black.

8.2.3 Final stellar populations

In previous chapters we have terminated the simulations once 10% of the mass has been converted to stellar mass. This made it easy to compare the stellar populations of different simulations. However, in this case the time when the simulation is terminated depends on of the time at which the first star becomes massive enough for feedback to begin. This means that the total amount of stellar mass at the end of the simulations can differ by a large amount, particularly between the fast and slow collision velocity simulations. To help visualise and compare the simulations we plot cumulative mass as a function of stellar mass, as we have done in previous chapters. However, in these simulations we plot cumulative mass in units of final mass, allowing us to more directly compare each simulation. We plot this in Fig. 8.5 for each of the four simulations carried out in this chapter. Each of the lines shows the stellar populations at the time star formation ceases. The profiles produced are very similar to those we find in Sec. 6.2. We see that slower velocity collisions produce many more low mass protostars and also have the most massive protostars created in all of the simulations. We also see that the simulations with a very bumpy density structure are less affected by the collision velocity in that they have profiles that are much more similar, although we still see more low mass protostars in simulations where the clouds collide slowly. In all cases we find that feedback has little effect on the final

stellar populations (i.e. the populations are similar to those of Sec. 6.2), rather it has the effect of terminating star formation.

Using stellar populations to determine the properties of a collision is viable because feedback is unable to destroy the imprint the collision leaves on the stellar population. It does however, very quickly disperse the gas, which could make it difficult to link any given stellar population to a collision. Instead the stellar population can be used to determine properties of a collision once it has been identified.

8.2.4 SUMMARY

In this chapter we have repeated some of the simulations in chapter 6 with the addition of photoionising feedback. We find that:

- The ionising star may remain in, or be ejected from, the layer. The HII region created in each case is very different. These HII regions can be difficult to identify because they appear different from different viewing angles.
- Stars that remain in the layer tend to produce bipolar HII regions which appear as two large lobes when viewed across the layer. When the HII region is viewed along the collision axis it appears as a circle, but with little shell material in front of, or behind, the HII region, i.e. a cylindrical shell.
- Stars that leave the layer produce an approximately spherical HII region which is initially unable to break through the layer. When one views this along the collision axis one sees imprints on the layer such as arcs, or in some cases full circles.
- HII regions very quickly terminate star formation. There is some evidence of triggered star formation, but this involves only small numbers of stars and therefore has very little effect on the stellar population.
- Consequently, feedback does not significantly alter the stellar populations we find in chapter 6. Stellar populations might therefore be used as a way of determining the parameters of a collision once it has been identified.

Chapter 9
conclusions

9.1 The effect of an ionising star on a cloud already undergoing freefall collapse

Massive stars have been shown to produce a large amount of ionising radiation which creates large HII regions. In chapter 4 we simulate the HII regions of stars with a range of ionising outputs, in order to determine how the HII regions and star formation are altered in a cloud that is already undergoing freefall collapse.

We first derive a semi-analytic model which we can use to predict the evolution of an HII region in such conditions. Using this we identify three possible evolutions of the HII region; it may expand and then contract, expand and then become approximately stationary before expanding once more, or expand continuously.

Using these predications we carry out three simulations to test each of these regimes. We find that our semi-analytic models are in good agreement with the evolution of the HII regions we observe in our simulations, confirming that each of the three regimes exists. From these results we show that stars with lower ionising outputs may be able to form HII regions but these can be overwhelmed by ram pressure and forced to contract. We also find that there is an ionising output at which a star will create an HII region that will initially expand before coming to a stop as the pressure of the HII region is balanced with the external ram pressure. Stars that have an output just larger than this are able to continue expansion, although the rate of expansion does decrease until the shell breaks out of the layer.

We find significant star formation only occurs in the simulations where the shell

becomes stationary. During this stage the shell is able to form dense regions which go on to form stars. We do see star formation in the cases where the HII region contracts, but not until the entire cloud converges on the centre, and in this case star formation is not a result of the ionising radiation produced by the star. We do see the formation of bright rimed clouds and pillars as the shells of the HII regions break up. However, these structures only produce stars in the case where the shell becomes stationary. When they form in the other simulations they do not form stars and are quickly evaporated by the HII region.

From these results we conclude that if the ambient gas has uniform density and is in freefall then HII regions can only be formed and maintained by the stars with high ionising outputs. These stars are likely to be the most massive stars. Stars that are less massive and therefore produce less ionising radiation may be able to form HII regions but they will not be able to maintain them for long enough to trigger star formation or disrupt the cloud. Even if a star is massive enough to form and maintain an HII region it is unlikely to trigger star formation as this requires very specific conditions that cause the HII region to become stationary for a significant period of time.

9.2 Colliding clouds

We carry out a number of simulations to determine what type of stellar populations cloud cloud collisions produce, and if these populations contain massive stars.

9.2.1 The collision velocity

In chapter 5 I have explored the evolution that results from the collision of two quiescent and approximately uniform-density clouds. These clouds have mass $M_\circ = 500\mathrm{M}_\odot$, radius $R_\circ = 2\,\mathrm{pc}$ and collide with relative speeds between $2.4\,\mathrm{km\,s^{-1}}$ and $4.0\,\mathrm{km\,s^{-1}}$. The results are summarised below:

- In all cases the colliding clouds produce a shock-compresed layer, which fragments into filaments.
- At lower relative velocities, it takes longer before fragmentation becomes nonlinear and delivers protostars.
- At low relative velocities the filaments are predominately radial due to the effects of lateral collapse, which drags and stretches them toward the collision

axis. Protostars condense out of filaments which they then fall along towards the centre, along with residual gas, and a single massive cluster forms there. In the central region competitive accretion leads to the formation of a few very massive protostars, and the ejection of a large number of low mass protostars. The distribution of filaments around the single massive cluster can be described as a hub and spoke system.

- At higher relative velocities , there is less time for lateral collapse of the layer, and so the filaments form a network like a spiders web, with many independent star-forming nodes collecting at the intersections of the filaments. The filaments feeding these nodes are relatively short and therefore deliver only a small amount of material from which stars can form. As a result, nodes are only able to spawn a small number of protostars that typically consist of one of moderate mass and a few of low mass. Dynamical ejections are rare because there are few protostars in each core.

- As the collision velocity is increased, the mean protostellar mass increases, but the range of protostellar masses goes down, so the maximum mass actually decreases and the minimum mass increases; there are many fewer low-mass protostars.

9.2.2 Variations from the simple model

In chapter 6 I have explored how the structures and stellar populations discussed in Chap. 5 are changed when either an closest approach, or a fractal density profile is added prior to collision. The results are summarised below:

- The critical velocity at which the filamentary network changes from a hub and spoke system to a spider's web with nodes is reduced as the closest approach is increased.

- As the velocity is increased beyond the critical velocity, the system tends towards a spider's web with a characteristic stellar mass.

- The introduction of a fractal density profile produces a filamentary structure that is a hybrid between the two types of networks. As a result some nodes are larger and look like hubs. The nodes in spider web systems are no longer uniform, with some having a great deal of mass allowing competitive accretion to take place.

- The underlying fractal density structure allows massive stars to form at all velocities in contrast to the uniform cases where they could only form below the critical velocity.

9.3 COLLIDING CLOUDS AND IONISING RADIATION

In chapters 5 and 6 we show that massive stars are likely to form as a result of cloud-cloud collisions. These stars will produce large amounts of ionising radiation which may disrupt the cloud and terminate star formation. Previously we have stopped the simulations prior to feedback becoming important. In this chapter we allow the simulations to continue and explore what effect the feedback from these stars has on local structure and star formation.

9.3.1 IONISING RADIATION ROUTINE

In chapter 7 we provide an overview of a new ionisation method we have included in GANDALF. We show that it is able to reproduce the Spitzer solution for a single ionising source. We also show that it is able to deal with multiple ionising sources. The routine is computationally efficient, and scales well with both the number of SPH particles and the number of sources.

9.3.2 RESULTS

In chapter 8 we have repeated some of the simulations in chapter 6 with the addition of photoionising feedback. We find that:

- The ionising star may remain in, or be ejected from, the layer. The HII region created in each case is very different. These HII regions can be difficult to identify because they appear different from different viewing angles.

- Stars that remain in the layer tend to produce bipolar HII regions which appear as two large lobes when viewed across the layer. When the HII region is viewed along the collision axis it appears as a circle, which could lead to the suggestion of a cylindrical HII region.

- Stars that leave the layer produce a spherical HII region which is initially unable to break through the layer. When one views this along the collision axis, one sees imprints on the layer such as arcs, or in some cases full circles.

- HII regions very quickly terminate star formation over a very short period of time. The evidence for triggered star formation is minimal, and it has very little effect on the stellar population.
- Feedback does not significantly alter the stellar populations we find in chapter 6. Stellar populations could therefore be used as a way of constraining the parameters of the collision that triggered their formation.

9.4 Future Work

In this thesis we have explored the effect of feedback on both single clouds and the layers formed by cloud-cloud collisions. In chapters 5 and 6 we examine the stellar populations that form as the result of collisions with a range of parameters. In the future we would explore these populations in more detail, looking at properties such as clustering. One then may be able to use these properties as identifiers of stellar populations that have been created by a cloud-cloud collisions.

We would repeat the simulations of chapter 8 at a higher resolution. We would then use these simulations to create synthetic images of the HII regions created by massive stars that are produced in cloud-cloud collisions. This would allow us to make more direct comparison with observations of regions that have bi-polar HII regions.

Bibliography

Aarseth, S. J.: 2003, *Gravitational N-Body Simulations*

Agertz, O., Kravtsov, A. V., Leitner, S. N., and Gnedin, N. Y.: 2013, *ApJ* **770**, 25

Andre, P., Ward-Thompson, D., and Barsony, M.: 1993, *ApJ* **406**, 122

Andre, P., Ward-Thompson, D., and Barsony, M.: 2000, *Protostars and Planets IV* p. 59

Balfour, S. K., Whitworth, A. P., Hubber, D. A., and Jaffa, S. E.: 2015, *MNRAS* **453**, 2471

Bate, M. R., Bonnell, I. A., and Price, N. M.: 1995, *MNRAS* **277**, 362

Beaumont, C. N. and Williams, J. P.: 2010, *ApJ* **709**, 791

Bisbas, T. G., Wünsch, R., Whitworth, A. P., and Hubber, D. A.: 2009, *ApJ* **497**, 649

Bisbas, T. G., Wünsch, R., Whitworth, A. P., Hubber, D. A., and Walch, S.: 2011, *ApJ* **736**, 142

Bodenheimer, P., Tenorio-Tagle, G., and Yorke, H. W.: 1979, *ApJ* **233**, 85

Bonnell, I. A. and Bate, M. R.: 2006, *MNRAS* **370**, 488

Chabrier, G.: 2005, in E. Corbelli, F. Palla, and H. Zinnecker (eds.), *The Initial Mass Function 50 Years Later*, Vol. 327 of *Astrophysics and Space Science Library*, p. 41

Chapman, S., Pongracic, H., Disney, M., Nelson, A., Turner, J., and Whitworth, A.: 1992, *Nature* **359**, 207

Dale, J. E., Bonnell, I. A., Clarke, C. J., and Bate, M. R.: 2005, *MNRAS* **358**, 291

Dale, J. E., Ercolano, B., and Bonnell, I.: 2012, *ArXiv e-prints*

Dale, J. E., Ercolano, B., and Clarke, C. J.: 2007, *MNRAS* **382**, 1759

Dale, J. E., Ngoumou, J., Ercolano, B., and Bonnell, I. A.: 2014, *MNRAS* **442**, 694

Deharveng, L., Zavagno, A., Samal, M. R., Anderson, L. D., LeLeu, G., Brevot, D., Duarte-Cabral, A., Molinari, S., Pestalozzi, M., Foster, J. B., Rathborne, J. M., and Jackson, J. M.: 2015, *A&A* **582**, A1

Dobbs, C. L., Pringle, J. E., and Duarte-Cabral, A.: 2015, *MNRAS* **446**, 3608

Duarte-Cabral, A., Dobbs, C. L., Peretto, N., and Fuller, G. A.: 2011, *A&A* **528**, A50

Elmegreen, B. G.: 2000, *ApJ* **530**, 277

Elmegreen, B. G.: 2002, *ApJ* **564**, 773

Elmegreen, B. G.: 2011, in C. Charbonnel and T. Montmerle (eds.), *EAS Publications Series*, Vol. 51 of *EAS Publications Series*, pp 45–58

Elmegreen, B. G. and Elmegreen, D. M.: 1978, *ApJ* **220**, 1051

Evans, II, N. J., Dunham, M. M., Jørgensen, J. K., Enoch, M. L., Merín, B., van Dishoeck, E. F., Alcalá, J. M., Myers, P. C., Stapelfeldt, K. R., Huard, T. L., Allen, L. E., Harvey, P. M., van Kempen, T., Blake, G. A., Koerner, D. W., Mundy, L. G., Padgett, D. L., and Sargent, A. I.: 2009, *ApJS* **181**, 321

Fall, S. M., Krumholz, M. R., and Matzner, C. D.: 2010, *ApJL* **710**, L142

Franco, J., Tenorio-Tagle, G., and Bodenheimer, P.: 1990, *ApJ* **349**, 126

Freyer, T., Hensler, G., and Yorke, H. W.: 2003, *ApJ* **594**, 888

Freyer, T., Hensler, G., and Yorke, H. W.: 2006, *ApJ* **638**, 262

Furukawa, N., Dawson, J. R., Ohama, A., Kawamura, A., Mizuno, N., Onishi, T., and Fukui, Y.: 2009, *ApJ* **696**, L115

Gingold, R. A. and Monaghan, J. J.: 1977, *MNRAS* **181**, 375

Górski, K. M., Hivon, E., Banday, A. J., Wandelt, B. D., Hansen, F. K., Reinecke, M., and Bartelmann, M.: 2005a, *ApJ* **622**, 759

Górski, K. M., Hivon, E., Banday, A. J., Wandelt, B. D., Hansen, F. K., Reinecke, M., and Bartelmann, M.: 2005b, *ApJ* **622**, 759

Hausman, M. A.: 1981, *ApJ* **245**, 72

Haworth, T. J., Shima, K., Tasker, E. J., Fukui, Y., Torii, K., Dale, J. E., Takahira, K., and Habe, A.: 2015a, *MNRAS* **454**, 1634

Haworth, T. J., Tasker, E. J., Fukui, Y., Torii, K., Dale, J. E., Shima, K., Takahira, K., Habe, A., and Hasegawa, K.: 2015b, *MNRAS* **450**, 10

Hobbs, A. and Nayakshin, S.: 2009, *MNRAS* **394**, 191

Hubber, D. A., Batty, C. P., McLeod, A., and Whitworth, A. P.: 2011, *ApJ* **529**, A27

Hubber, D. A., Walch, S., and Whitworth, A. P.: 2013, *MNRAS* **430**, 3261

Inoue, T. and Fukui, Y.: 2013, *ApJL* **774**, L31

Kahn, F. D.: 1954, *Bull. Astron. Soc. Neth* **12**, 187

Kessel-Deynet, O. and Burkert, A.: 2000, *MNRAS* **315**, 713

Kirk, J. M., Ward-Thompson, D., Palmeirim, P., André, P., Griffin, M. J., Hargrave, P. J., Könyves, V., Bernard, J.-P., Nutter, D. J., Sibthorpe, B., Di Francesco, J., Abergel, A., Arzoumanian, D., Benedettini, M., Bontemps, S., Elia, D., Hennemann, M., Hill, T., Men'shchikov, A., Motte, F., Nguyen-Luong, Q., Peretto, N., Pezzuto, S., Rygl, K. L. J., Sadavoy, S. I., Schisano, E., Schneider, N., Testi, L., and White, G.: 2013, *MNRAS* **432**, 1424

Kroupa, P.: 2001, *MNRAS* **322**, 231

Krumholz, M. R. and Matzner, C. D.: 2009, *ApJ* **703**, 1352

Kwan, J. and Valdes, F.: 1987, *ApJ* **315**, 92

Lada, C. J.: 1999, in C. J. Lada and N. D. Kylafis (eds.), *NATO Advanced Science Institutes (ASI) Series C*, Vol. 540 of *NATO Advanced Science Institutes (ASI) Series C*, p. 143

Larson, R. B.: 1981, *MNRAS* **194**, 809

Lattanzio, J. C., Monaghan, J. J., Pongracic, H., and Schwarz, M. P.: 1985, *MNRAS* **215**, 125

Lefloch, B. and Lazareff, B.: 1995, *A&A* **301**, 522

Lomax, O., Whitworth, A. P., and Hubber, D. A.: 2015, *MNRAS* **449**, 662

Lucy, L. B.: 1977, *AJ* **82**, 1013

Matzner, C. D.: 2002, *ApJ* **566**, 302

McKee, C. F., van Buren, D., and Lazareff, B.: 1984, *ApJL* **278**, L115

McLeod, A. D. and Whitworth, A. P.: 2013, *MNRAS* **431**, 710

Micic, M., Glover, S. C. O., Banerjee, R., and Klessen, R. S.: 2013, *MNRAS* **432**, 626

Monaghan, J. J.: 1997, *Journal of Computational Physics* **136**, 298

Monaghan, J. J.: 2002, *MNRAS* **335**, 843

Monaghan, J. J. and Lattanzio, J. C.: 1985, *A&A* **149**, 135

Morris, J. P. and Monaghan, J. J.: 1997, *Journal of Computational Physics* **136**, 41

Motte, F., Andre, P., and Neri, R.: 1998, *A&A* **336**, 150

Murray, N., Quataert, E., and Thompson, T. A.: 2010, *ApJ* **709**, 191

Nelson, R. P. and Papaloizou, J. C. B.: 1994, *MNRAS* **270**, 1

Norman, C. and Silk, J.: 1980, in B. H. Andrew (ed.), *Interstellar Molecules*, Vol. 87 of *IAU Symposium*, pp 137–148

Ohama, A., Dawson, J. R., Furukawa, N., Kawamura, A., Moribe, N., Yamamoto, H., Okuda, T., Mizuno, N., Onishi, T., Maezawa, H., Minamidani, T., Mizuno, A., and Fukui, Y.: 2010, *ApJ* **709**, 975

Oort, J. H. and Spitzer, Jr., L.: 1955, *ApJ* **121**, 6

Ostriker, J. P. and Cowie, L. L.: 1981, *ApJ* **243**, L127

Palmeirim, P., Andre, P., Kirk, J., and Nutter, D.: 2012, *ArXiv e-prints*

Peretto, N., Fuller, G. A., André, P., Arzoumanian, D., Rivilla, V. M., Bardeau, S., Duarte Puertas, S., Guzman Fernandez, J. P., Lenfestey, C., Li, G.-X., Olguin, F. A., Röck, B. R., de Villiers, H., and Williams, J.: 2014, *A & A* **561**, A83

Preibisch, T. and Zinnecker, H.: 2007, in B. G. Elmegreen and J. Palous (eds.), *IAU Symposium*, Vol. 237 of *IAU Symposium*, pp 270–277

Price, D. J. and Monaghan, J. J.: 2004, *MNRAS* **348**, 139

Price, D. J. and Monaghan, J. J.: 2007, *MNRAS* **374**, 1347

Roberts, W. W.: 1969, *ApJ* **158**, 123

Roberts, Jr., W. W. and Stewart, G. R.: 1987, *Formation of giant molecular clouds in global spiral structures: The role of orbital dynamics and cloud-cloud collisions*, Technical report

Rogers, H. and Pittard, J. M.: 2013, *MNRAS* **431**, 1337

Rosswog, S., Davies, M. B., Thielemann, F.-K., and Piran, T.: 2000, *A&A* **360**, 171

Salpeter, E. E.: 1955, *ApJ* **121**, 161

Scoville, N. Z. and Hersh, K.: 1979, *ApJ* **229**, 578

Simpson, R. J., Nutter, D., and Ward-Thompson, D.: 2008, *MNRAS* **391**, 205

Spitzer, L.: 1978, *Physical processes in the interstellar medium*

Springel, V., Yoshida, N., and White, S. D. M.: 2001, *NA* **6**, 79

Stamatellos, D., Whitworth, A. P., Bisbas, T., and Goodwin, S.: 2007, *A&A* **475**, 37

Strømgren, B.: 1939, *ApJ* **89**, 526

Sugitani, K., Tamura, M., and Ogura, K.: 1999, in T. Nakamoto (ed.), *Star Formation 1999*, pp 358–364

Takahira, K., Tasker, E. J., and Habe, A.: 2014, *ApJ* **792**, 63

Tenorio-Tagle, G.: 1979, *A&A* **71**, 59

Tomisaka, K.: 1984, *PASJ* **36**, 457

Torii, K., Enokiya, R., Sano, H., Yoshiike, S., Hanaoka, N., Ohama, A., Furukawa, N., Dawson, J. R., Moribe, N., Oishi, K., Nakashima, Y., Okuda, T., Yamamoto, H., Kawamura, A., Mizuno, N., Maezawa, H., Onishi, T., Mizuno, A., and Fukui, Y.: 2011, *ApJ* **738**, 46

Vishniac, E. T.: 1983, *ApJ* **274**, 152

Walborn, N. R., Maíz-Apellániz, J., and Barbá, R. H.: 2002, *AJ* **124**, 1601

Walch, S. K., Whitworth, A. P., Bisbas, T., Wünsch, R., and Hubber, D.: 2012, *MNRAS* **427**, 625

Whitworth, A.: 1979, *MNRAS* **186**, 59

Whitworth, A. P., Bhattal, A. S., Chapman, S. J., Disney, M. J., and Turner, J. A.: 1994, *MNRAS* **268**, 291

Whitworth, A. P. and Francis, N.: 2002, *MNRAS* **329**, 641

Wilking, B. A. and Lada, C. J.: 1983, *ApJ* **274**, 698

Woodward, P. R.: 1976, *ApJ* **207**, 484